HYPERSPECTRAL THERMAL INFRARED ANALYSIS OF THE SALTON SEA GEOTHERMAL FIELD

by

Kevin Andrew Reath

B.S. Geology, University of Pittsburgh, 2006

Submitted to the Graduate Faculty of

Arts and Science in partial fulfillment

of the requirements for the degree of

Master of Science

University of Pittsburgh

2011

UNIVERSITY OF PITTSBURGH

ARTS AND SCIENCES

This thesis was presented

by

Kevin Andrew Reath

It was defended on

July 27, 2011

and approved by

William Harbert, Professor, University of Pittsburgh

Ian Skilling, Assistant Professor, University of Pittsburgh

Thesis Director: Michael Ramsey, Associate Professor, University of Pittsburgh

Copyright © by Kevin Andrew Reath

2011

HYPERSPECTRAL THERMAL INFRARED ANALYSIS OF THE SALTON SEA GEOTHERMAL FIELD

Kevin Andrew Reath, M.S.

University of Pittsburgh, 2011

The Salton Sea Geothermal Field is an active 20 km^2 region in southern California, which lies along the Calipatria Fault; an offshoot of the San Andreas Fault. Several geothermal fields (including the Davis-Schrimpf and Sandbar fields) and ten power plants generating 340 MW lie within this region. To better understand the mineral and thermal distribution of the surface, hyperspectral thermal infrared (TIR) data were acquired by The Aerospace Corporation using the Spatially Enhanced Broadchannel Array Spectrograph System (SEBASS) airborne sensor on March 26, 2009 and April 6, 2010. SEBASS collects 128 wavelength channels at 1 meter spatial resolution. Such high resolution data are rarely available for this type of scientific analysis and enabled the identification of mineral assemblages associated with geothermally-active areas. This study was supported by field based thermal readings and surface samples. Thermal readings obtained remotely and in the field are also used to better understand the dynamics of the piping and heat flux this system.

High resolution remote sensing of this area enables the identification of minerals associated with geothermally active areas and the subsequent use as indicator minerals to discover other, previously unknown, active areas. These minerals include anhydrite and one unknown mineral. Scanning electron microscopy (SEM) and x-ray diffraction (XRD) were

performed on one of the samples in order to positively identify this mineral and further constrain the TIR analysis.

Data obtained by the SEBASS sensor were later regressed to the 32 channel spectral resolution of the future Mineral and Gas Identifier (MAGI) sensor. At this lower spectral resolution these important geothermal indicator minerals are still effectively identified. Therefore, proving the satellite imager counter-part of this sensor, MAGI-L, would be a much desired follow-on instrument to the 5 TIR channel resolution Advanced Spaceborne Thermal Emission Reflection Radiometer (ASTER) sensor, by producing accurate identification of surface mineralogy previously not detected by an orbiting sensor.

Work performed during this research has the potential to be used at other geothermal sites to better characterize transient mineralogy, understand the influence of surface and ground water in these systems, and ultimately to identify new geothermal targets for future exploration.

TABLE OF CONTENTS

LIST OF TABLES

LIST OF FIGURES

LIST OF IMAGES

LIST OF GRAPHS

PREFACE

First, I would like to thank Michael Ramsey, for advising and supporting me for years in both my graduate and undergraduate degrees and for giving the opportunity to challenge and better myself by working on this project.

I'd also like to thank:

The NASA instrument Incubator Program (IIP) for the *"Development of the Mineral and Gas Identifier (MAGI) Instrument"* and The Aerospace Corporation, who funded my research and without whom none of this would be possible.

My committee members: Ian Skilling and Bill Harbert, who put their skill and time into helping me with my research.

My parents, Harvey and Evelyn, who supported me through good times and bad and are the main reason I'm not working in a warehouse

Christopher Hughes who helped as a field assistant, office mate, paper editor, sounding board, and in every other conceivable way he or I could come up with.

My sister, Shannon who gave me a place to live when I needed it and at least pretends like she is interested in what I'm talking about when I mention my research.

My sisters dog, Carina, who kept my company while I was writing despite being angry that I was spending too much time staring at the computer screen, not playing with her.

Rachel Lee, for helping me during my mind blanks with the spectrometer, and always being a good IVIS lab partner.

Alison Graettinger, for taking me to Iceland, helping me with volcanology, and always listening when I have questions.

Bobby Karimi for always being in the mood to have fun, being good at making silly hats, and hosting more parties than he can afford.

All my lab mates in the IVIS program and office mates, who have pointed me in the right direction and helped me keep my sanity.

David Tratt and Jeffrey Hall my contacts at The Aerospace Corporation, who always answer any SEBASS questions and help me get the latest data files.

I'd also like to thank my legion of proof readier on this thesis, without you the pages of this thesis would run red with ink: Hilary Morgan, Alison Graettinger, Christopher Hughes, and Bobby Karimi.

1.0 INTRODUCTION

New geothermal areas can be located by identifying areas with a higher temperature than background temperatures and finding the key minerals surrounding geothermal locations. Higher spectral and spatial resolution sensors allow mineral spectra previously undetected with earlier generation sensors to be observed. Therefore, a more accurate assessment of mineralogy can be quickly recorded for geothermal features and the surrounding area allowing for new geothermal locations to be found remotely with a minimum of time spent in the field exploring potential regions.

A geothermal field is an area of the earth characterized by a relatively high heat flow due to present or recent orogenic or magmatic activity or from the radioactive decay of crustal isotopes (Allaby and Allaby, 2001). This high heat flow, as well as the unique minerals surrounding the fields, are produced as a result of increased temperatures that can be detected remotely. Sinter and tufa carbonate deposits as well as hydrothermally altered clays and sulfates have all been found to be associated with geothermal systems (Calvin et al., 2005).

Geological remote sensing was first utilized for mineral exploration in the 1970s by Abrams et al. (1977) in the Cuprite mining district using a NASA airborne multispectral sensor. This analysis identified hydrothermal alteration minerals; however these minerals could only be identified by altered rocks with an absence of iron oxide and by the presence of clay minerals. Using multispectral airborne and spaceborne thermal data to detect and map silica content

Vincent et al (1984) studied the Cuprite district again several years later. Numerous studies have been performed utilizing multispectral remote sensing in order to detect broad hydrothermal mineralization; however, most sensors lack the needed spectral resolution to identify specific mineral features (Sabins, 1999). Both the Spatially Enhanced Broadchannel Array Spectrograph System (SEBASS) and the Mineral And Gas Identifier (MAGI) sensors posses the necessary spectral resolution to allow the identification of these specific mineral features, specifically those associated with geothermal systems.

1.1 SALTON SEA GEOLOGIC HISTORY

1.1.1 Regional Geology

The body of water known as the Salton Sea is a recent phenomenon that came into existence as a result of the 1905 Colorado River flood filling the Salton Trough (**Figure 1-1**). Prior to 1905 the area was relatively dry, although the presence of evaporates in the geologic record and the mining of evaporates, which occurred in the late 1800's suggest it to be an area that commonly fills with water and then evaporates. The present day lake is a large, closed system, below-sea-level lake and is currently maintained by irrigation run-off from the surrounding agricultural area and occasional storm water run-off from the surrounding mountains (Helgeson, 1968).

The Salton Sea geothermal field is located on the southeastern edge of the Salton Sea, which is found in the low point of the Salton Trough (**Figure 1-1**), an extensional depression associated with the active continental rift between the North American and Pacific Plates (Elders and Sass, 1987). This rift occurs along the San Andreas Fault. The depression is surrounded by

granitic mountains and metasediments. The trough has been partially filled with detritus from the Colorado River delta; the propagation of this delta isolated the Salton trough from the Gulf of California to the south and created a closed basin.

The Salton Sea Trough is one of the few regions where a continent is actively rifting and is therefore characterized by vigorous tectonic deformation, geodetic deformation, high heat flow, frequent seismicity, and volcanism (Sass, 1988). The many geothermal fields found within this region attest to this increased level of high heat flow and volcanic activity.

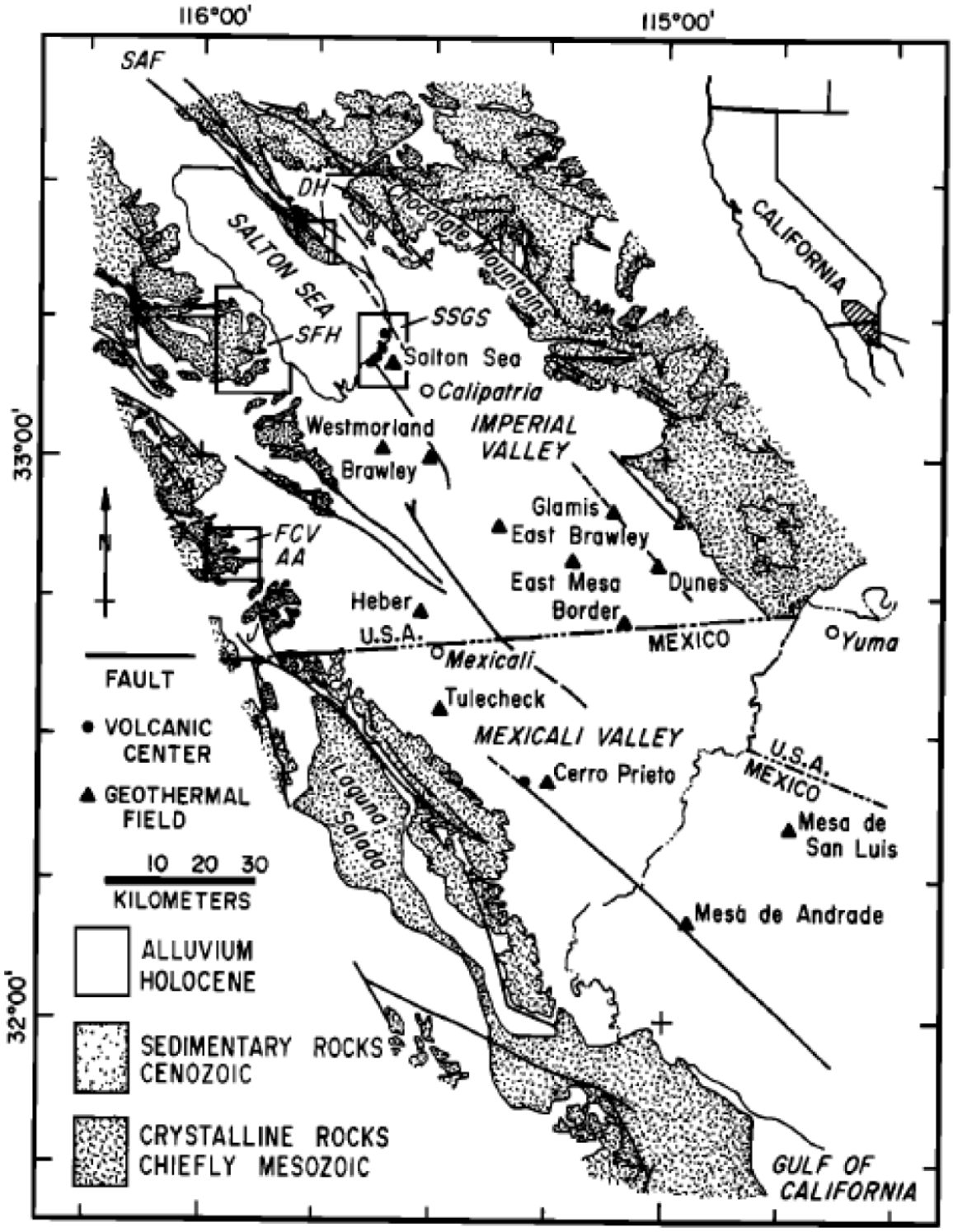

Figure 1-1: Map of Salton Sea Trough (Herzig et al., 1988). This map provides an overview of locations and surface geology in the Salton Sea Trough area. AA, Alverson Andesite; Dh, Durmid Hills; FCV Fish Creek-Vallecito; J, Jacumba; SAF, San Andreas Fault; SFH San Felipe Hills; SSGS, Salton Sea Geothermal system. Location of SSDP bore is approximated by the black triangle within SSGS area.

The trough area consists of a relatively flat basement floor, which is covered by lacustrine and deltaic Tertiary sands and shales that have been overlain by Quaternary alluvium (Helgeson, 1968). The Salton Sea Drilling Project (SSDP) borehole within the area found the general stratigraphy to be characterized by shales with interbedded siltstones, sandstones, and pebbly mud of varying thickness (Herzig et al., 1988). Sedimentary rocks found within the borehole were commonly partly altered to greenschist and amphibolite facies. Shale sections within the borehole were found to be lacustrine and up to 100 m thick, the inter-bedded units associated with fluvial-deltaic sediment were found with thicknesses ranging from 10 m to a few cm (Herzig et al., 1988) (**Figure 1-2**). Due to the stratigraphic occurrence of these mineral assemblages, this formation is classified as part of the Borrego-Brawley formation (Helgeson, 1968); a Pliocene/Pleistocene formation made up of predominantly shales and siltstones and found in the Split Mountains that surround the Salton Sea Trough. Below 900 m, rocks in the bore have undergone greenschist facies metamorphism; however original depositional textures are well preserved within the rocks. Volcanic tuffs and basaltic sills were also encountered in the borehole at 1704m and 2880 to 2896m and are common within the stratigraphy of the Salton Sea Basin.

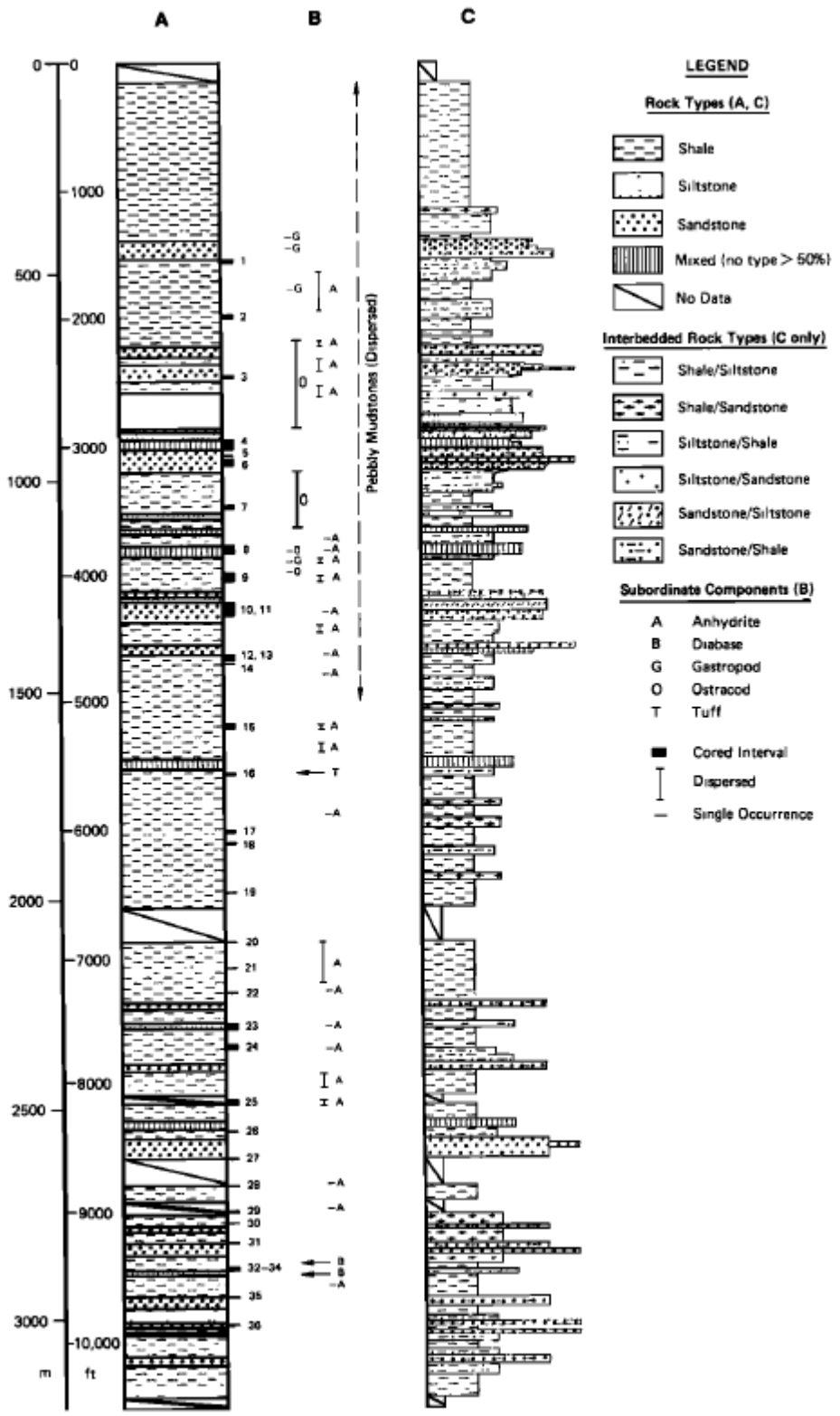

Figure 1-2 : Detailed Lithstratigraphic column of the SSDP borehole (Herzig et al., 1988). Column A: Dominant rock types; Column B: Cored intervals and subordinate components, Column C: Weathering Profile**.**

The SSDP bore was found to be commonly offset by centimeter scale normal faults within the soft sediment loading structures. These were determined to be a result of seismic disturbances in the area. Secondary minerals were found intruding these faults such as calcite, pyrite, sphalerite, galena, chalcopyrite, and anhydrite (McKibben et al., 1988) as a result of geothermal brine infilling.

Anhydrite is present in the borehole as nodules above the depth of 1220m and as masses of bladed crystals below 1220m. Compared to an outcrop of the Borrego Formation found in the Durmid Hills the nodular anhydrite was found to be similar to textures found for gypsum. This suggests that anhydrite found in the SSDP borehole is replacing gypsum (Herzig et al., 1988).

The paleodepositional environments of the Salton Sea Trough were found to be similar to the modern environment examining the sediments found in the SSDP borehole. Any kind of marine depositions can be ruled out due to the Colorado River delta acting as a barrier for marine transgressions since the Pliocene and Pleistocene. (Van de Kamp, 1973). Lacustrine sequences dominate the stratigraphy found in the borehole, along with the deltas of distributary river channels that cross-cut them. The pebbly mudstones found in the sequence were determined to be a result of storm induced debris flows from the surrounding alluvial fans. Evaporites are also common in the shales; recording subaerial periods that any lake in the area would have dried (Herzig et al., 1988). In the SSDP borehole hydrothermal and/or syndepositional alteration has caused these gypsum sabhka-like nodules to become dehydrated and replaced with anhydrite. The interbedding of lacustrine muds, coastal sand deposits, and evaporate-bearing muds indicate fluctuations in paleo-lake levels and periodic flooding of the region. Thick intervals of sandstone may also suggest prolonged deposition from the delta of a distributary river (Herzig et al., 1988).

Dating has been attempted upon the tuff encountered during the SSDP, however due to the altered nature of the tuff, this procedure has been problematic. Hydrothermal alteration has caused the tuff to become recrystallized and therefore correlation based on petrography and texture becomes quite difficult. However, by correlating this tuff with its volcanic source it can be used as a time-stratigraphic marker. In near-by Durmid Hill (25 km NE), outcrops of the Bishop Tuff, a chemically and petrographically distinct flow tuff, were encountered and believed to be related to the tuff found in the borehole. In the altered borehole tuff facies, chlorite porphyroblasts are believed to have replaced biotite phenocrysts found consistently within the Bishop Tuff. Furthermore, the proportions of Mn, Sm and other rare earth elements (REE) found within the altered tuff are very similar to that of the Bishop Tuff, and differ strongly from that of other pyroclastic rocks found in the area (Herzig and Elders, 1988). Therefore, the altered tuff encountered at 1704 m depth within the SSDP borehole was concluded to be the Bishop Tuff that is 0.7 Ma old. This places the rate of sedimentation and subsidence of the area to be approximately 2.4 mm/yr for the past 0.7 Ma (Herzig and Elders, 1988). By extrapolating the sedimentation and subsidence rate of 2.4 mm/yr it can be inferred that the depth (3220 m) of the borehole is 600m shy of the Pliocene-Pleistocene boundary (~1.35 Ma).

1.1.2 Salton Sea Geothermal System

The Salton Sea geothermal area includes an offshoot of the San Andreas Fault known as the Calipatria fault and is found along the southeast margin of the Salton Sea (Yonker et al, 1982) (**Figure 1-3**). The geothermal field itself has an area of approximately 20 km^2 of gryphons and mud pots.

Figure 1-3 : Aerial view of the Salton Sea, the approximate geothermal field area has been highlighted with a yellow box (Google Earth 2010)

As early as 1540, accounts can be found of what is assumed to be the Salton Sea geothermal field. Melchor Dias explored the Gulf of California coast, upon attempting to penetrate the overland Colorado River Delta he was stopped by “fields of boiling mud” (Sass, 1988). These were the very first unconfirmed accounts of geothermal activity in this area. Early Salton Sea descriptions mention notable thermal springs and geyser activity (Blake, 1855). In 1927 three commercial wells were drilled for steam, but were insufficient for any type of power generation (Rook and Williams, 1942). In the 1930’s shallow wells were drilled in order to mine the large amounts of CO_2 found degassing from local fumaroles for a dry ice plant. In 1957 a deep well was drilled, which was the first to encounter hot geothermal brines, thus sparking

geologic interest in the area (Helgeson, 1968). Upon analyzing these brines, the Salton Sea geothermal system was found to be unique in composition. The brines consisted heavily of sodium, potassium, calcium, and chloride, and also contained large amounts of iron, manganese, silica, strontium, boron, lithium, barium, lead, zinc, and copper.

In 1984 a multi-agency program made up of the Department of Energy (DOE), the National Science Foundation (NSF), and the U.S. Geological Survey (USGS) was formed in order to partially fund and petition additional funding from Congress for the SSDP. The SSDP was an innovative science-led drilling program that was located very close to the geothermal field that is described in this paper. The precise location of drilling has not been released. As a result of this program, scientific research was performed in this area that includes many tests on subsurface geology and geothermal brine compositions, results are used in this paper.

The Salton Sea Geothermal field currently has ten geothermal plants that produce a combined capacity of 340MW (net) or enough energy to power over 100,000 homes. The majority of the research described in this thesis takes place within two locations found in the geothermal field. The first of these locations is the Davis-Schrimpf Geothermal field (**Figure 1-4**); a large, unvegetated field of mud pots and mud volcano-like gryphons located southeast of Mullet Island. This location has been a historical area of extensive geologic and geothermal research. The second location is a geothermal field that has only recently become subaerial due to lower water levels of the Salton Sea, and will henceforth be known as the Sandbar Geothermal Field. For years, activity at this geothermal field has been identified as submarine fumaroles, but now specific vents, geologic features, and mineralogy surrounding them can be studied.

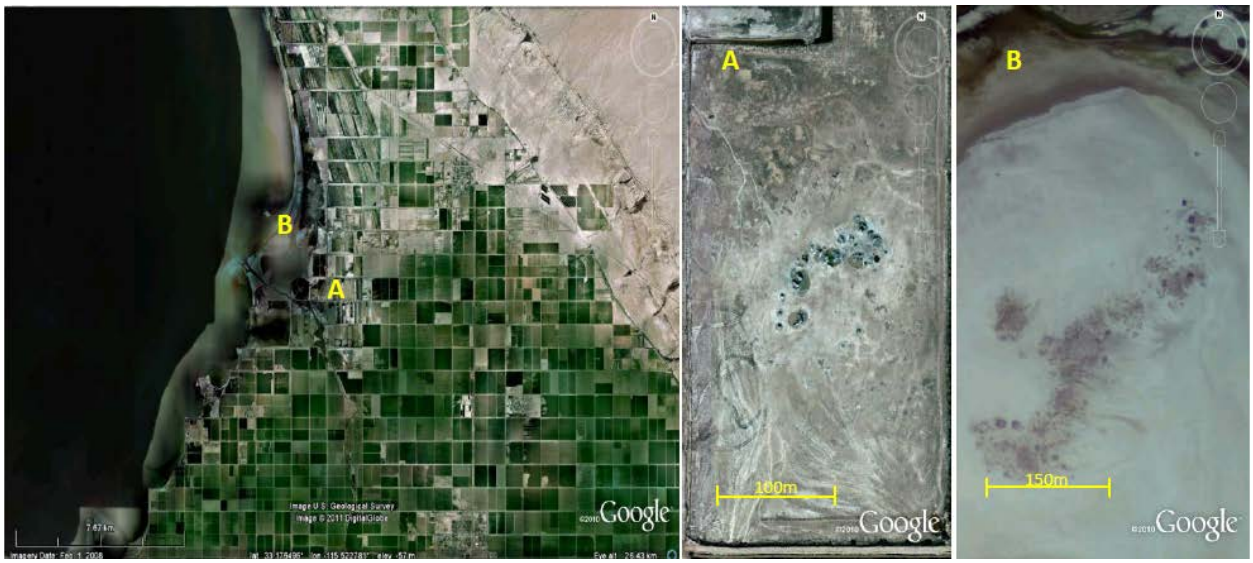

Figure 1-4: A February 28, 2008 aerial view of the Salton Sea Geothermal Field, showing the location of (A) the Davis-Schrimpf Geothermal field, as well as a zoomed in aerial view of the field, and (B) the Sandbar Geothermal Field, along with its zoomed in aerial view. (Google Earth 2010)

The Salton Sea Geothermal Field is a result of shallow magmatic intrusions that occur as a result of the pull-apart extensional setting Salton Sea Trough (Elders et al., 1972). These magmatic intrusions cause contact metamorphism and fluid flow within the lacustrine and fluvial sediments, which in turn causes a considerable amount a CO_2 degassing and temperatures of over 350°C at 1440m depth. Geothermal seeps, such as the Davis-Schrimpf Geothermal Field, in a sedimentary basin are commonly a result of vertical migration pathways that occur from faults, mud volcanoes, dewatering pipes, pockmarks, and hydrothermal vent complexes (Svensen et. al., 2009). The morphological features of the Davis-Schrimpf field are very similar to seep fields found on dormant mud volcanoes; however, they are not related to mud volcanism (Planke et al., 2003). Mud volcanism is associated with large-scale mud breccias eruptions and a low temperature seep stage. No large-scale mud eruptions have been recorded in association with this field and the temperatures of gryphons exceed the typically lower temperatures in a mud volcano

seep stage (Jukubov et al., 1971). The Davis-Schrimpf field has more the 50 individual seeps within a relatively compact 120 m^2 area. This field is dominated by gyrphons and mud pots, which contain a substantial amount of water as well as many fumarole vents (**Figure 1-5**). All of these seep locations expel gas (dominated by CO_2 and contains other volcanic gases), mud, and water in differing amounts. Gryphons tend to expel more mud, causing them to continuously build up flanks and produce a cone-like structure; the mudpots are mostly composed of water. All sources release CO_2 nearly continuously, which occurs as a continuous bubbling in the mudpots and gryphons and as an audible hissing in the fumaroles.

Image 1-1: Davis-Schrimpf Geothermal field, July 2, 2010. In the foreground is an example of a typical mudpot, in the back ground is a gryphon. Notice the collapsed tripod (.65m), which is denoted with a yellow arrow, resting against the gryphon for scale. Fumaroles can be found along the flanks of the gryphon.

Isotopic evidence suggests (Svensen et al., 2007) that CO_2 produced from devolatilization reactions with sedimentary carbonate may be the main driver for the seep activity found in these fields. It has been reported by Svensen et al., 2009 and was later confirmed in the field that the temperatures of the gryphons (40-65°C) are significantly higher than the mudpots (15-25°C). Thus, the differences in makeup of these two features are affecting how well heat from the magma intrusion radiates to the surface. The fact that the water-rich pools are cooler then the gryphons suggests that water is not the main heat carrier. This leaves two other possible sources: hot gas and/or mobilized mud from lower depths (Svensen et al., 2009). In the case of gas being the heat carrier, hot gas from a deep reservoir would migrate through overlying sediments and heat near-surface mud in gryphons. Interacting with shallow water reservoirs, such as those found in the mud pots, the gas is cooled due to the lower temperatures and high specific heat capacity of the water. In the case of mud being the heat carrier, hot mud from below 120 m depth could be mobilized by the high flux of gas, causing fluidization and transport to the surface (Svensen et al., 2009). This would explain the build-up of gryphons from deep mud being transported to the surface. Caldera structures are also expected in the system from downward sagging as deep material is mobilized. This system would allow for a pipe-like structure to connect the gas and mud source with the expulsive gryphon vent. With gryphon build-up and caldera subsidence remaining in a constant state, convection in the pipe structure would lead to remobilization of mud that was erupted at an earlier stage (**Figure 1-5**). Fumaroles and mud pots found in this area, where little or no mud has been mobilized, would be expected to have a different dynamic than the gryphon system.

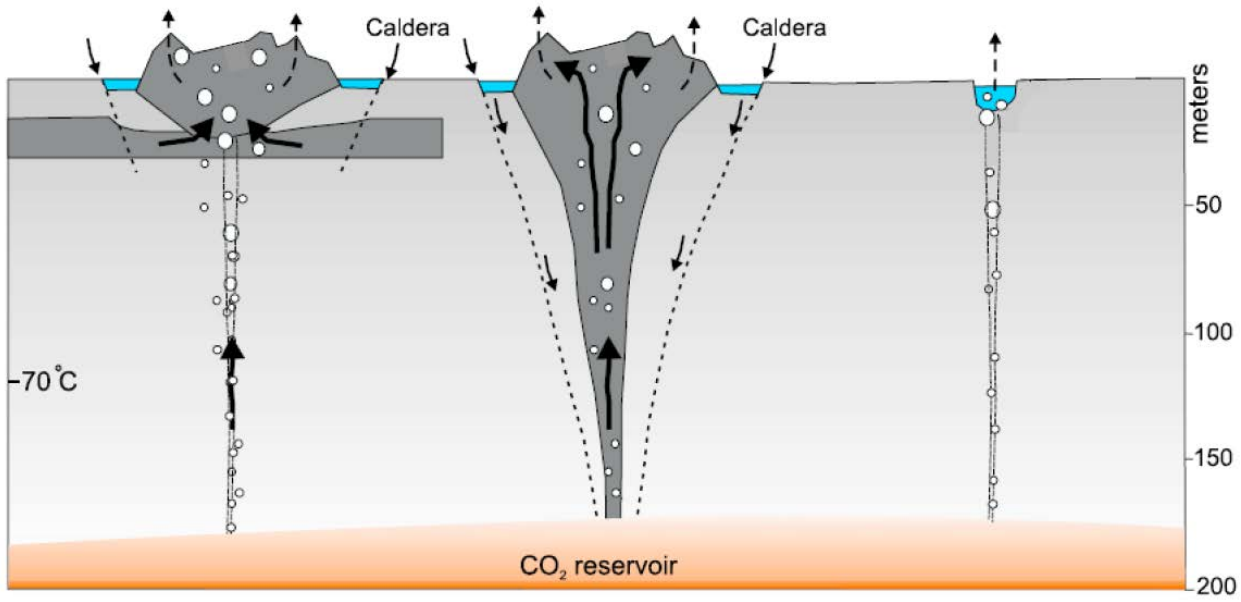

Figure 1-5: (Modified from Svensen et al., 2009) Cross section of geothermal piping system. (Left) Gryphon cross-section demonstrating the geothermal system using gas as the heat carrier, mud does not become mobilized and heated until shallower depths. (Middle) Gryphon cross-section of a system that utilizes deep mud as the heat carrier. (Right) Mud-pot cross-section demonstrating the system, which is believed to create them, notice gas interaction with water at shallow depths that cools the gas resulting in lower temperature mud-pots.

1.1.3 Surface Mineralogy

Although the Salton Sea Trough is composed of mostly shale at shallow depths in the stratigraphic column, the surface is a different composition. Much of the trough has become filled with quartz-rich sand from the break-down of sandstone facies from the surrounding mountains. In some areas evaporate minerals are present as a result of the areas past and present evaporitic nature. The predicted sulfate evaporite sequence for the Salton Sea, based on research performed in Spencer, 2000, includes the minerals gypsum, glauberite, blödite, polyhalite, anhydrite, and epsomite. Studying areas surrounding active and formally active geothermal

areas, mineralogy becomes more complex due to geothermal brines containing approximately 25% Total Dissolved Solids (TDS) (Thompson and Fourier, 1988) reaching the surface. Much work still needs to be done locating and understanding the complexities of this surface mineralogy. The research and technologies presented in this paper will help to reveal a better understanding in this area.

1.2 ADVANCED SPACEBORNE THERMAL EMISSION AND REFLECTION RADIOMETER (ASTER)

ASTER is one of five advanced sensors that were included on the NASA Terra satellite that was launched in December 1999. Shortly after its launch, Terra began collecting and transmitting data that are still being collected today and has created a decade-long archive of remote sensing data. The ASTER instrument is composed of three separate wavelength sub-systems that all utilize separate telescopes (Yamaguchi et al., 1998): the Visible Near InfraRed (VNIR), Short Wave InfraRed (SWIR), and Thermal InfraRed (TIR) subsystems. There are four VNIR channels between 0.52 and 0.86 μm that have a pixel size of 15 m^2. Digital elevation models (DEMs) are made from the third and fourth VNIR channel, using a fourth telescope that points backwards from the satellite and collects the fourth channel at the same wavelength as the third. Six short-wave infrared (SWIR) channels between 1.6 and 2.43 μm have a pixel size of 30 m^2 (unfortunately SWIR ceased to operate in April 2009 due to a failed cryo-cooler), and five TIR channels between 8.13 and 11.65 μm that have a pixel size of 90 m^2 (Fujisada et al., 1998). Only the TIR channels of the ASTER sensor will be used for the analysis during the research

performed in this thesis. The TIR instrument is a 10 by 5 array of HgCdTe elements, which are used in a whiskbroom configuration (Yamaguchi et al., 1998).

The ASTER sensor has a 16 day temporal resolution at the equator that can be decreased for urgent matters due to the ±8.5° off-nadir cross track pointing capabilities of the TIR telescope (Kääb et al., 2003). ASTER collects data with a swath width of 60 km that allows for relatively large, regional data collection (**Figure 1-6**). However, due to the 90 m pixel size in the TIR, individual features are difficult to observe, an example of this can be observed by zooming in on Davis-Schrimpf field (**Figure 1-7)**.

Due to ASTER having five channels in the TIR and a 16 day temporal resolution that can be reduced if needed, it is considered one of the most comprehensive TIR sensors currently available in orbit. It is because of these aspects that ASTER is used as a frame of reference for the Mineral And Gas Identifier (MAGI) sensor, which is currently in development.

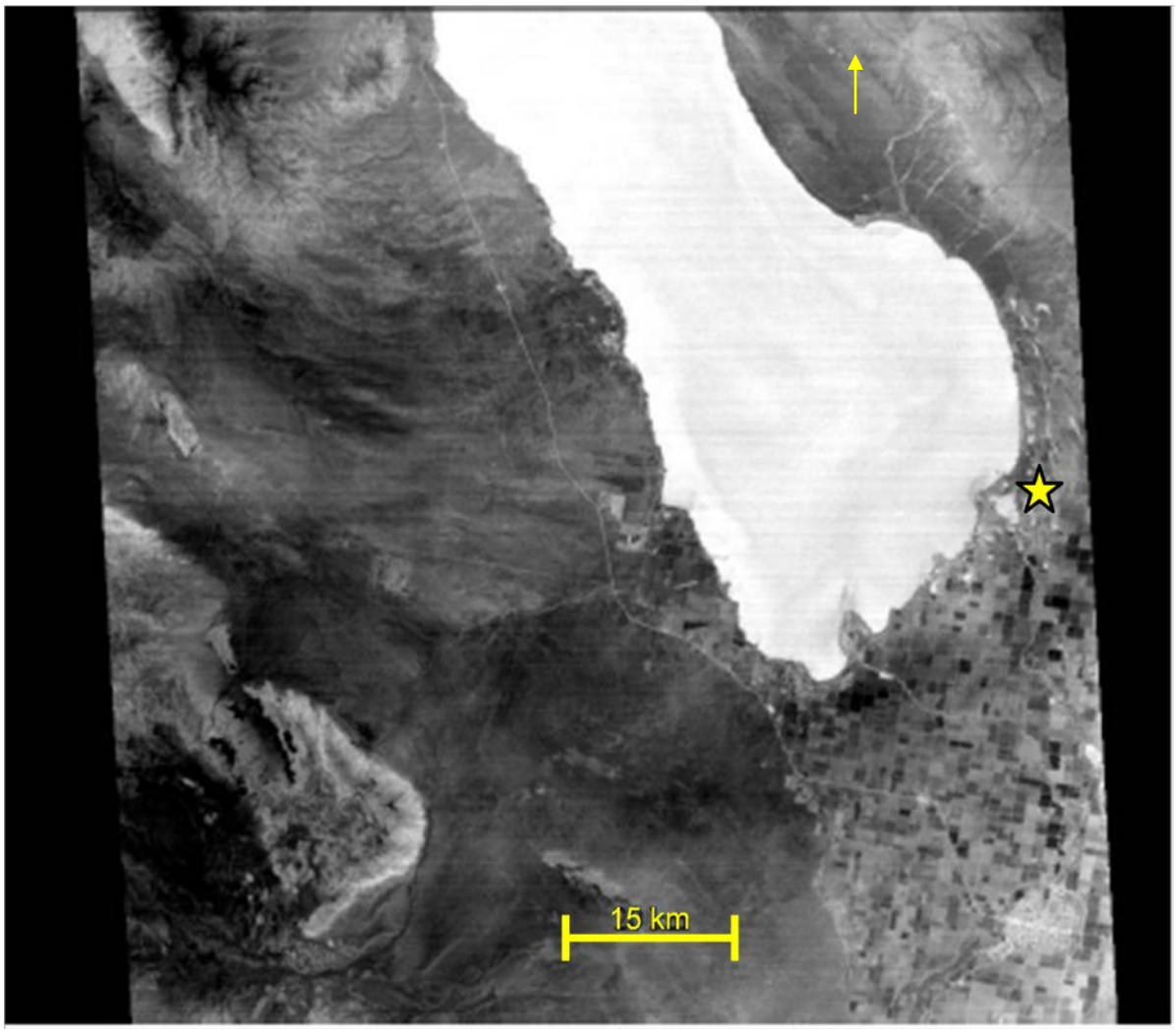

Figure 1-6: ASTER channel 11 (8.634 µm), of the Salton Sea, CA aquired on Septemper 7, 2009, This image shows the full swath width of the ASTER dataset. The star on this image indicates the loction of the Davis-Schrimpf geotherml field.

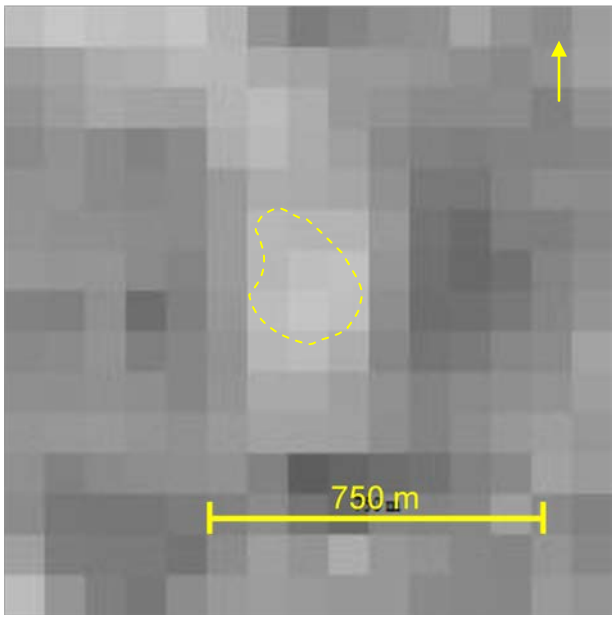

Figure 1-7: Zoom of the Davis-Schrimpf geothermal field obtained from Figure 1-7. The field itself is the lighter area in the middle of the image that has been outline with a yellow dashed line. Notice, the specific features can be easily observed.

1.3 SPATIALLY ENHANCED BROADCHANNEL ARRAY SPECTROGRAPH SYSTEM (SEBASS)

SEBASS is a hyperspectral airborne TIR sensor with 128 channels within the region of 2.5 to 5.2 µm and 7.5 to 13.5 µm that is designed and operated by The Aerospace Corporation (Hackwell et al, 1996). The SEBASS sensor is a passive TIR sensor commonly flown on-board a

Twin Otter aircraft. Measurements are taken with two liquid helium cooled 128 by 128 detector-element arrays that cover the 2.5 to 5.2 µm region and the 7.5 to 13.5 µm region (Vaughan et al., 2003). For the purpose of this work, and to reduce complications in calculating reflectance and emissivity, only the 7.5 to 13.5 µm region was utilized. The instantaneous field of view (IFOV) of SEBASS is 1.1 mrad per pixel with a total field of view (FOV) of approximately 7.3° (Vaughan et al., 2003). The aircraft typically flies at an altitude of 915 m that creates an average pixel size of approximately 1 m^2. The swath width of the SEBASS dataset is 128 pixels in the cross-track direction or 128 m from a typical altitude. Compared to the ASTER data, SEBASS allows for the ground features found in the Davis-Schrimpf to be clearly resolved. However, the total area covered by this instrument is limited in comparison to many other remote sensors (**Figure 1-8**).

The SEBASS sensor was flown over the Salton Sea geothermal field and surrounding areas on March 26, 2009 and April 6, 2010. These datasets represent a level of high spectral and spatial resolution not commonly encountered that can be used to analyze the geothermal areas in the Salton Sea in an attempt to remotely identify these key minerals. Comparisons will be made with the soon to be produced Mineral and Gas Identifier (MAGI) sensor once these minerals have been identified.

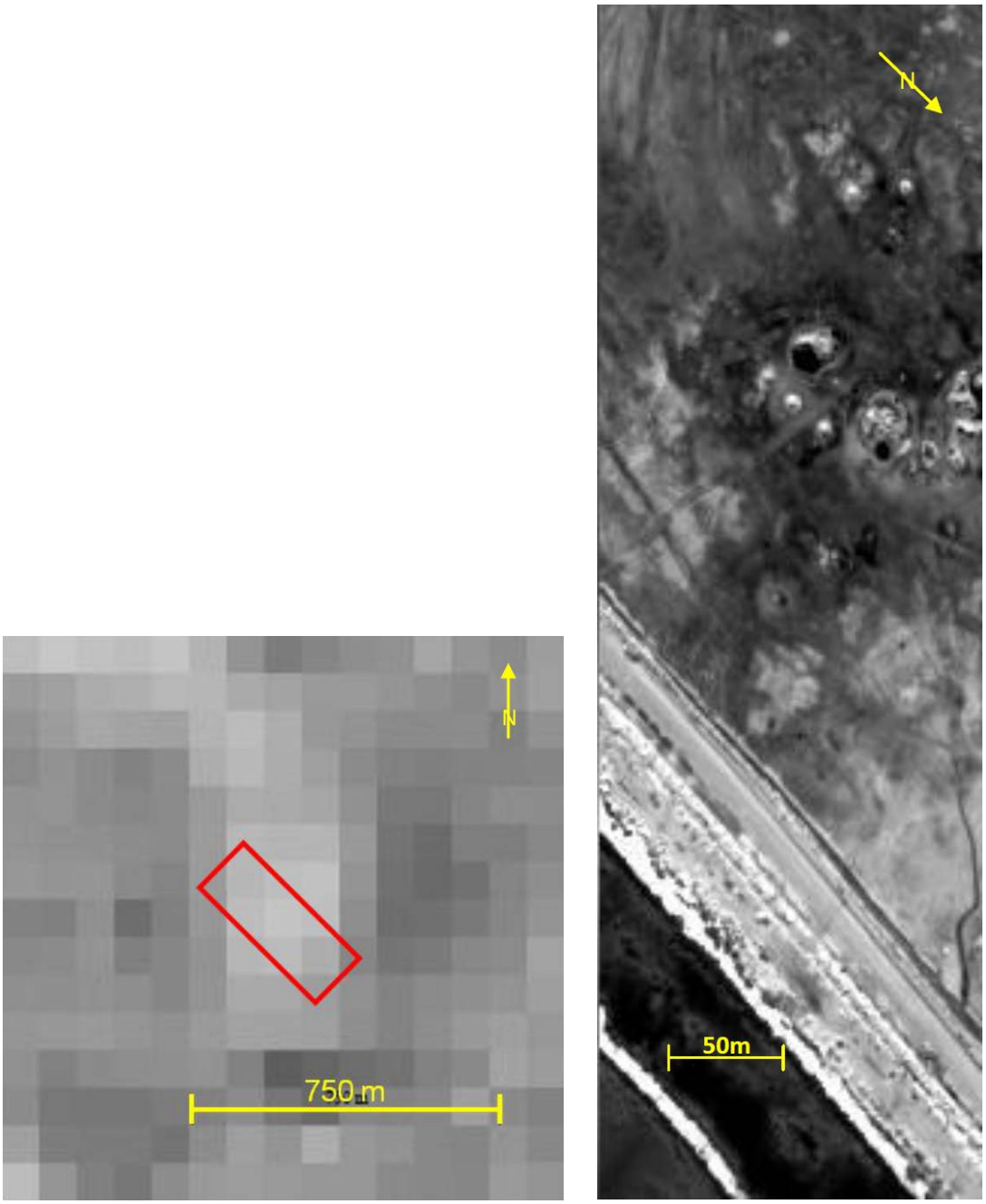

Figure 1-8: ASTER zoom of the Davis-Schrimpf geothermal field of channel 11 (8.634 µm) radiance, obtained September 7, 2009 (left), with a red box indicating the area covered by the SEBASS image of channel 18 (8.6183µm) radiance, obtained March 26, 2009 (right).

1.4 MINERAL AND GAS IDENTIFIER (MAGI)

The MAGI airborne sensor is a 32 channel, airborne TIR sensor being developed by The Aerospace Corporation to address the next generation Hyperspectral Infrared Imager (HyspIRI)-type sensors being developed (Hall et al., 2008). The sensor will have capabilities ranging from rock and soil identification to volcano characteristics and monitoring. This instrument uses 32 channels that range from 7.8 to 12.5 μm, and exceed the capabilities of existing multi-spectral TIR imagers currently available to the scientific community, thus enabling additional missions. The higher spectral resolution of the 32 channels compared to the 5 channel ASTER-type sensors will expand the discrimination of rock types, and expand gas-detection capabilities allowing for more accurate land-surface temperature retrieval. The MAGI instrument will also have a pixel size similar to that of SEBASS; a smaller pixel size enables weaker thermal changes to be tracked and allows the monitoring of smaller gas-emission sources. Initially the MAGI sensor will be flown on a Twin Otter platform with a whiskbroom scanner; however there are plans to use MAGI as a test platform for a proposed satellite based sensor that will be known as "MAGI-L" or the Low Earth Orbit (LEO) version of MAGI (Hall et al, 2008).

Creating an instrument with such a high degree of spectral resolution will allow for more information to be obtained than its earlier predecessors and still enable the collection of a majority of the data that is found in more complex and costly hyperspectral sensors. The efficiency of using only 32 channels was tested using the SEBASS sensor, which has 128 channels in the TIR, to collect and compare initial data. The 128 channel SEBASS data was first processed to remove atmospheric absorption and emission features using the InScene Atmospheric Compensation algorithm (ISAC) and then regressed to the 32 channel centers of the MAGI senor and the 5 channels of the ASTER sensor.

The common mineralogy analog site of Cuprite, NV was used to demonstrate capabilities in indentifying minerals by Hall et al, 2008. A constrained least-square-regression was used to identify surface minerals found within the Cuprite SEBASS dataset. A 32 channel image at the MAGI channel centers, 16 channels, and 5 channel ASTER regressions was preformed upon these data (**Figure 1-9**). The 32 channel image was visually identical to the original data, the 16 channel regression lead to some confusion in positively identifying silicate end-members and the ASTER regression resulted in a loss of fidelity (Hall et al, 2008).

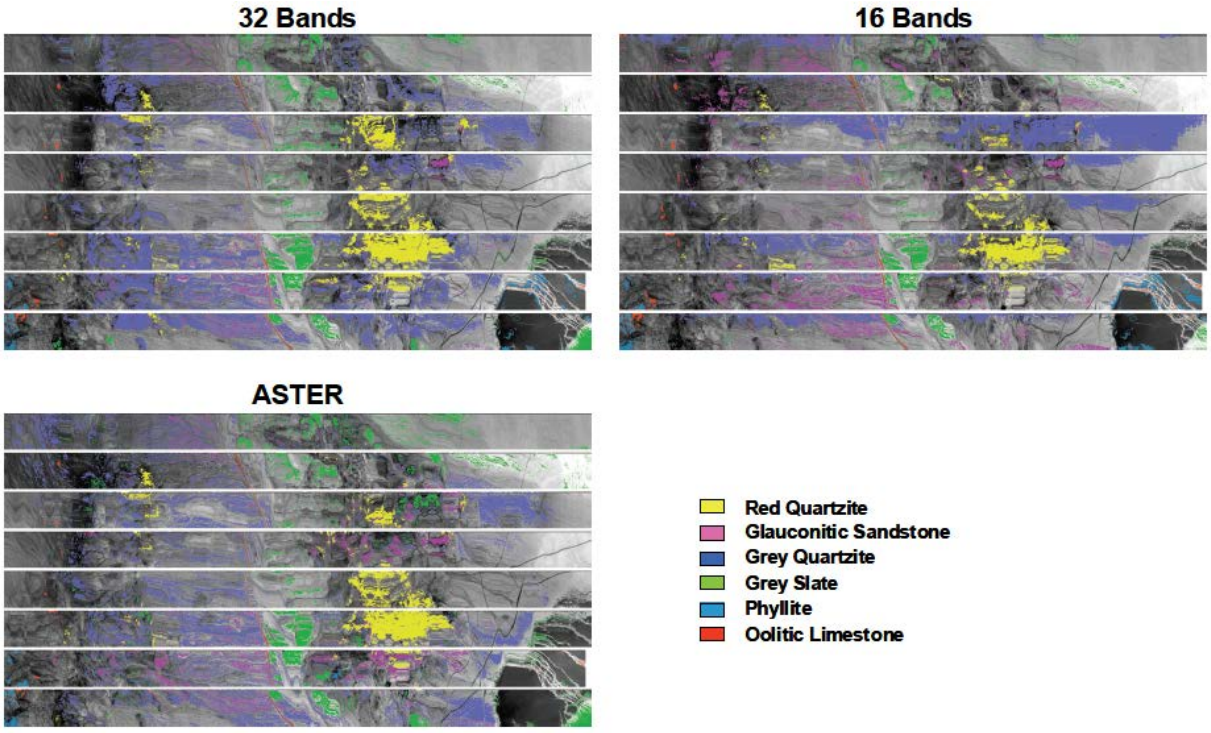

Figure 1-9: Computed mineralogy of Cuprite using SEBASS TIR data collect October, 2002 (Hall et al, 2008). The data has been regressed to 32, 16, and 5 channels. Each horizontal strip represents a separate flight line.

Hall et al, 2008 performed a similar study involving gas detection. In this study SEBASS data was collected by The Aerospace Corporation over a coal-fired power plant and analyzed for CO_2. The images were once again viewed as 128, 32, 16, and 5 channel data. The ability to separate CO_2 plumes from underlying surface clutter deteriorates as the number of spectral channels decrease (**Figure 1-10**). In the case of this specific study the detection of CO_2 was still possible with 32 channels but nearly impossible at 16 channels and impossible at 5 channels.

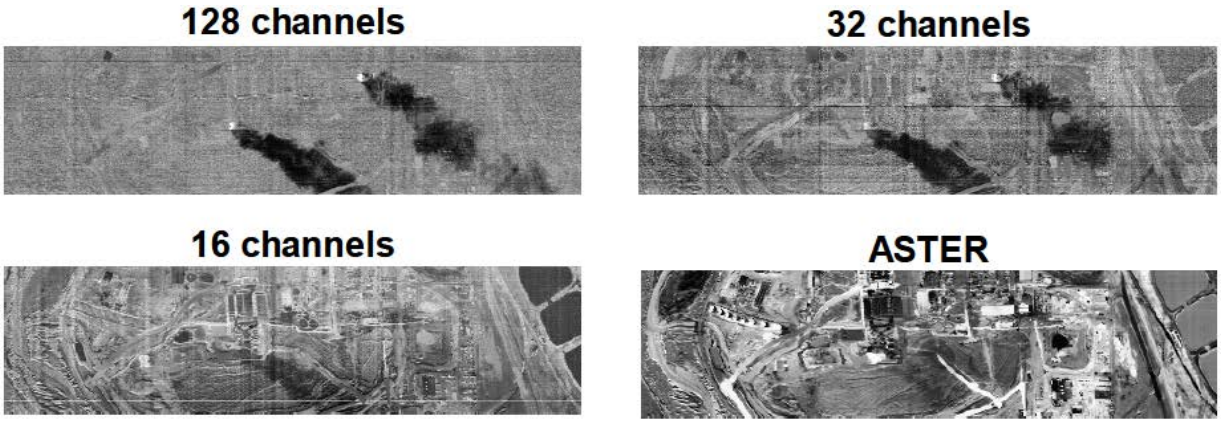

Figure 1-10: CO_2 plumes detected above a coal burning power plant (Hall et al., 2008). The original 128 channel SEBASS image is located in the upper left corner, is has then been degraded in each subsequent image to the 32 channels of MAGI, 16 channels, and the 5 channels of ASTER.

In a related second study by Hall et al, 2008, the ability of MAGI to detect other gases measured by Noise Equivalent Contrast (NEC). The contrast represented is the gas column density times the temperature contrast between the gas and the previous (gas free) background behind the gas. A summary plot has been created of the NEC ratios for 28 chemicals (**Figure 1-11**). The performance penalty was found to be markedly worse for any spectral resolution found to be below 32 channels.

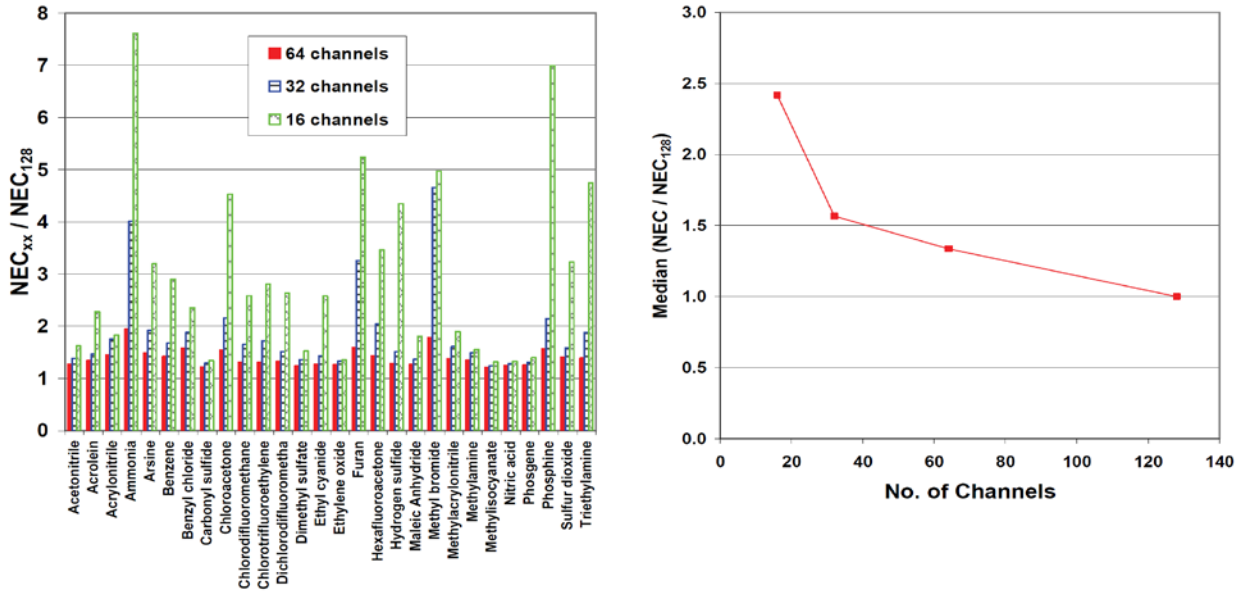

Figure 1-11: Left: Values of NEC for 64, 32 and 16 channels ratios to values for 128 channels (Hall et al., 2008). Larger ratios suggest a lower sensitivity to the specific chemical. In most cases sensitivity loss from 128 channels to 32 is less than a factor of 2. Right: NEC median ratio vs. Number of channels (Hall et al, 2008). Notice the significant penalty whereas the data is reduced to 16 channels.

As mentioned earlier, the MAGI airborne sensor is currently under development. Due to the varying heights where the plane could fly, pixel size is not set; however, from the typical flight altitude of 915 m, the pixel size will be approximately 1 m^2. This pixel size is significantly smaller than that of the previous multi-spectral TIR sensor datasets commonly available for scientific use. This allows for a more detailed dataset where specific features such as mudpots and the mineralogy surrounding them can be studied.

The Salton Sea will likely be one of the initial MAGI targets. This is due to its close distance to the Hawthorne Municipal Airport (265 km) where the Twin Otter plane that the MAGI sensor is connected to will take off and land. Furthermore, the geothermal activity in the Salton Sea geothermal field makes the area a region of greater interest.

Therefore this work will demonstrates how well the spectral resolution of the MAGI sensor will perform in a non-analog environment. By first studying SEBASS and identifying important mineralogical features found at its higher spectral resolution, these same features can be analyzed at the MAGI resolution. Mineral percentages on the surface at both resolutions will also be analyzed and compared. Proving these features can be found at both resolutions and demonstrating similar surface mineral percentages will signify that the MAGI sensor, with 96 less channels than the SEBASS sensor, can be just as effective for a portion of the price.

2.0 METHODS

2.1 ASTER DATA PROCESSING

Cloud-free ASTER nighttime TIR radiance data were used for this research. Calculations using band math in the Environment for Visualizing Images (ENVI) program are needed in order to derive radiance values for further processing. The band math function allows channels or files to be input as variables in user defined functions. To perform these band math calculations upon the ASTER dataset, band scale factors specific to each TIR channel needed to be found within the global attributes for the file. These factors were then multiplied by the Digital Number (DN) for the corresponding channel to derive radiance values. The ASTER data product used for this research was the level 2 09T product, meaning the data was comprised of atmospherically corrected (atmospheric adsorption and emission features are removed) radiance values for the 5 TIR channels.

The atmospherically corrected radiance values can then be reduced into temperature and emissivity values. This is possible because the radiance (L) emitted at a given wavelength (λ) is a function of both temperature (T) and emissivity (ε). Analyzing the radiance data from a sensor,

by correcting instrument effects, black-body radiance (*B*), temperature, and emissivity can be related through the Planck equation:

$$L_{(\lambda,T)} = \varepsilon_{\lambda} B_{(\lambda,T)} = \varepsilon_{\lambda} \left\{ \frac{C_1 \lambda^{-5}}{[\exp\,(C_2/\lambda T) - 1]} \right\}$$

where C_1 is equal to 3.74 x 10^{-16} Wm^2 and C_2 is equal to 0.0144 mK. In solving this equation, problems arise upon dealing with the unknown variables of temperature and emissivity. These variables result in the occurrence of a set of underdetermined equations. Temperature is assumed to have a constant value across the area of a pixel, whereas emissivity is wavelength dependent. The problem of finding values for these undefined variables is solved by the emissivity normalization method or by using the ASTER L2 emissivity product, which has already been converted to emissivity.

In the emissivity normalization method, the emissivity for each wavelength is given a blackbody value, the highest resulting temperature for each pixel is then assigned as the constant temperature value for all wavelengths. For this research the emissivity blackbody value was set to 0.986, the emissivity value for water (Saunders, 1967). After defining the temperature variable, the emissivity variable is the only undefined variable in each equation. By reducing the equation to one unidentified variable, emissivity values can be easily computed for each wavelength channel (Realmuto 1990, Gillespie, 1985).

A temperature map can be created for the area within the 60 km swath width covered by the ASTER sensor. This was done by calculating the temperature for each pixel in the ASTER dataset through the emissivity normalization process (**Figure 2-1**). Thermal variations in specific regions within the Salton Sea can be derived by examining the variation per pixel. Regional thermal variations were analyzed by collecting all cloud-free nighttime scenes over the Salton Sea Geothermal Field. Ten separate cloud-free, nighttime ASTER scenes were found between November, 2003, and February, 2010. Although ASTER was launched in December 1999, data matching these criteria could not be found prior to November 1, 2003. Temperatures were calculated for the Davis-Schrimpf geothermal field area, a typical average ground surface area, and a typical average water surface area. The geothermal field temperature was calculated from a single 90 m pixel, the ground and water surface temperatures were calculated using the average temperature of a 10 x 10 pixel square in order to reduce pixel to pixel noise. The 10 x 10 region used to identify ground temperature was located southwest of the Salton Sea. This region had little to no vegetation or agriculture and was free of any temperature anomalies in all ASTER scenes. The water region was taken from the middle of the Salton Sea; as with the ground region, no temperature anomalies were observed. The temperatures found in each of these regions were then used to analyze the temperature variations of the geothermal field over the seven year window of datasets collected (**Graph 2-1**).

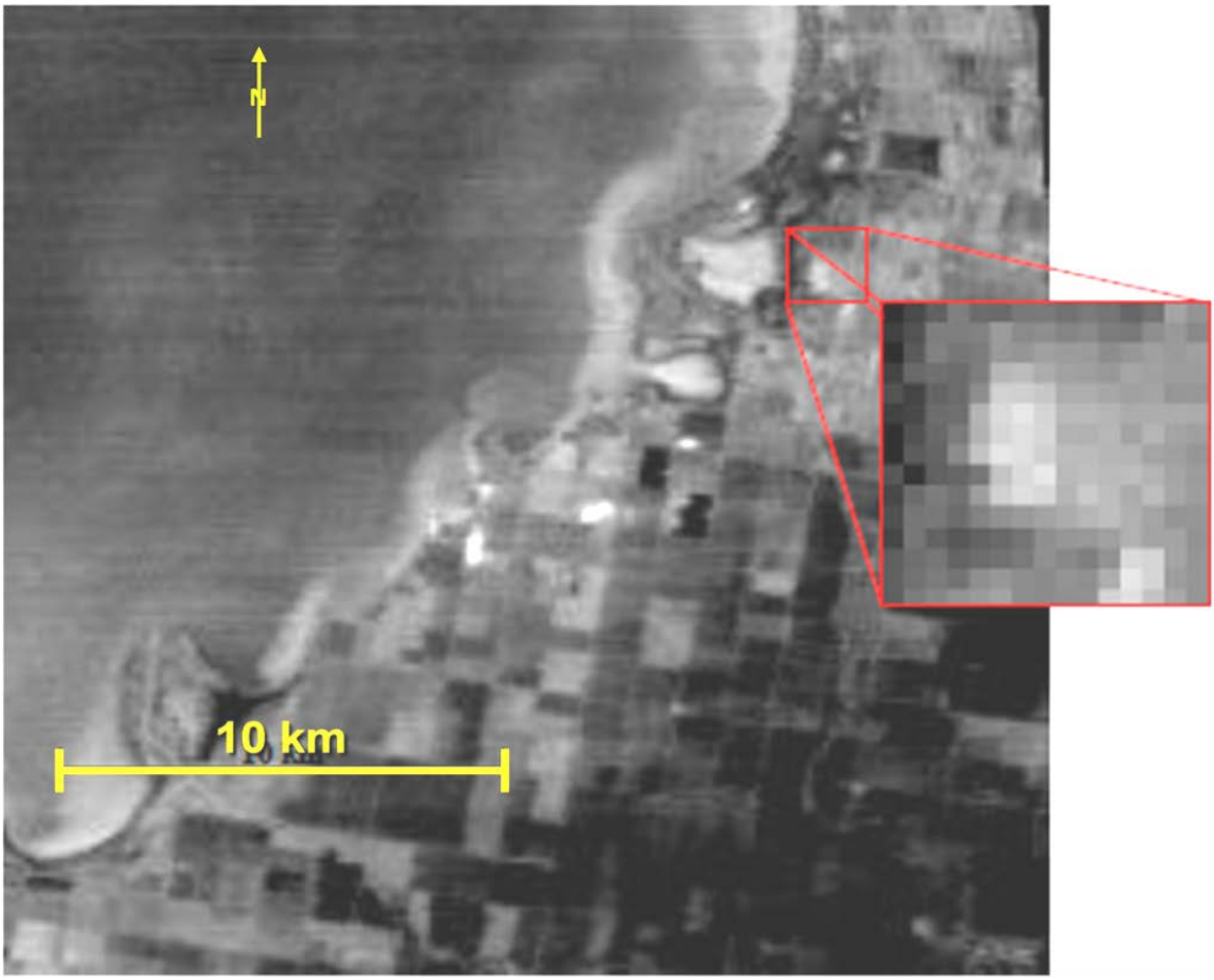

Figure 2-1: ASTER temperature map from May 21, 2010 with a dynamic temperature range of 22.6 to 29.8°C. Lighter tones denote warmer areas. The location in the red box is the Davis-Schrimpf geothermal field; it is visibly warmer (lighter) than the surrounding area.

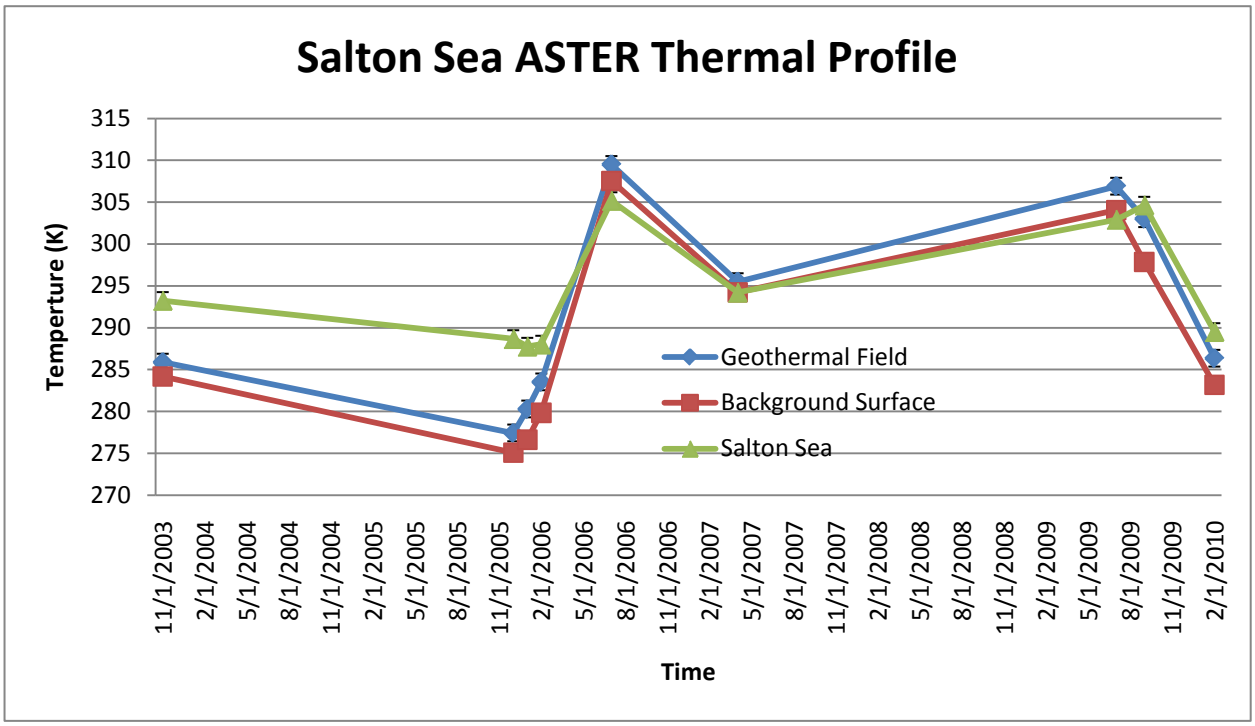

Graph 2-1: ASTER night data graphed over seven years of available data. Average temperatures for the same 10 by 10 pixel area of the Salton Sea and a background surface in the Salton Sea area are recorded for each dataset as well as the temperature of the single pixel covering the Davis-Schrimpf geothermal area. The background surface temperature and the geothermal area temperatures seem to be highly correlated, whereas the water temperatures show a similar, but not direct correlation. Error bars indicate the average error for ASTER TIR data (±1-2°C).

2.2 SEBASS DATA PROCESSING

2.2.1 Band Math

ENVI band math was the first step utilized in order to have the radiance data in the correct units needed to perform image processing on SEBASS data. Radiance data for SEBASS is received in $\mu W/cm^2*sr*\mu m$, this results in the DN value being one hundred times larger for the same radiance than it was in the units ($W/m^2*sr*\mu m$) used by ENVI in the emissivity normalization function. Therefore the entire dataset is divided by one hundred resulting in comparable radiance values with correct units. The ENVI standard atmospheric correction algorithm, which is a modified version of the ISAC model used by The Aerospace Corporation, was then applied to these data.

Once the conversion of units and atmospheric correction had been performed, the emissivity normalization function was applied. This produced pixel brightness temperature values as well as emissivity pixel values in each of the 128 separate channels.

2.2.2 Image Deconvolution

An image deconvolution function was then performed upon this emissivity data in order to establish mineral concentration percentages in each pixel. The principle behind the image deconvolution technique is that the energy emitted or reflected from a surface containing multiple minerals can be deciphered by the amount of energy that has radiated from each mineral (Ramsey and Christensen, 1998; Adams et al., 1989). The emitted energy from different minerals

is calculated in proportion to its aerial percentages. Due to TIR emissivity being linearly related to the minerals present on the surface, percentages of surface minerals at specific locations can be derived from this aerial percentage of emitted energy. By utilizing spectra of pure minerals to act as end-members, the mixed spectra can be deconvolved using a least squares linear fit function, allowing percentages of each end-member to be identified, as well as producing a measure of the model quality. With this method, surface mineral assemblages can be inferred from TIR emissivity values (Ramsey and Christensen, 1998; Adams et al., 1989).

In order to effectively use image deconvolution, the proper mineral end-members must be used in the deconvolution process. First, a reasonable sampling of the spectra within the dataset must be created. This was done to the March 26, 2009 SEBASS data of the Davis-Schrimpf geothermal field by performing a decorrelation stretch (Gillespie, 1992) at channels 10 (8.1956µm), 25 (9.0549µm), and 69 (11.4142µm) (**Figure 2-2**). This stretch allows for slight variations in these 3 channels to be exaggerated and therefore visibly identifies areas of varying surface composition. By noting the wavelength locations of spectral peaks and absorption features and searching for spectra with corresponding features, the spectra in the dataset are compared to pure mineral spectra found in the Arizona State University Thermal Emission Spectrometer (TES) spectral library (Christensen et al., 2000). After extensive comparisons and testing, a mineral suite of: quartz, gypsum (selenite), kaolinite (powder), halloysite (powder), hectorite (powder), microcline, anhydrite, and chalk were used as end-members. This mineral suite was used every time linear unmixing was performed on any Salton Sea dataset using SEBASS or MAGI resolution for the duration of this research.

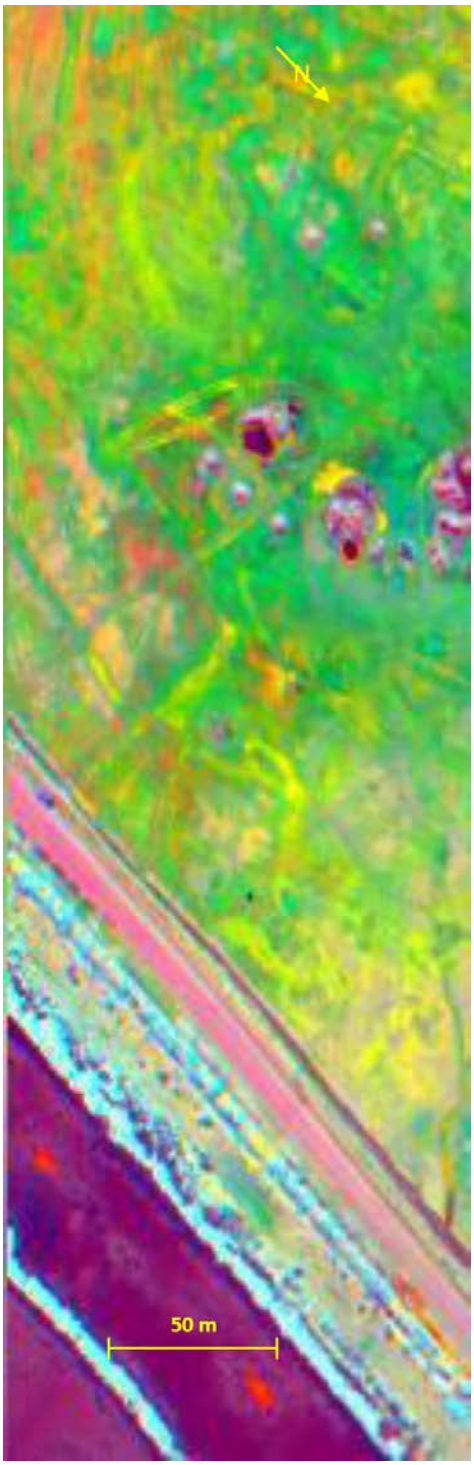

Figure 2-2: SEBASS scene of the Davis-Schrimpf Geothermal field, March 26, 2009. This image is a decorrelation stretch of the channels R: 69, B: 25, G: 10. Notice the many differing colors that are used as indicators of areas of spectral variability.

Before the mineral suite end-members were run in the image deconvolution process, they were resampled using the ENVI spectral library resampling tool. This process allows the spectral points of the pure mineral spectra in the library to match the spectral resolution of the sensor data where the deconvolution function is being performed. Once this had been completed, image deconvolution can take place. The image deconvolution processes produces images corresponding to blackbody, mineral percentage, and Root Mean Squared (RMS) values. The blackbody end-member image represents the percentage that is classified as a blackbody for each pixel. Only the portion of a pixel not classified as a blackbody is considered where calculating the true mineral percentages. A series of images are produced that correspond to each mineral end-member, these images represent the percentage values of the amount of that specific mineral found in each pixel. The amount of images produced for this series is directly related to the amount of mineral end-members utilized in the linear deconvolution processes. Finally, an image is produced representing RMS values of each pixel; this is used as an interpretation of the model quality of the aforementioned mineral maps.

2.2.3 Image Warping

In order to properly compare the March 26, 2009 dataset of the Davis-Schrimpf field to the April 6, 2010 dataset georeferencing is required. This is due to artifacts in the 2010 dataset created by flight errors, which causes the data to be elongated and shortened in places that are not true to reality. The idea behind georeferencing of an image/dataset is to reference the image to specific geographic coordinates and/or correct an image to match a given base image geometry (Li and Husar, 1999). In this case the 2009 image was used as a base image, due to no flight error

artifacts being present, and the 2010 image was corrected to match its geometry. This process entails setting a series of points on the 2010 warp image that match locations on the 2009 base image. The accuracy of georeferencing increases as more tie points are chosen. In this case 62 points were used to georeference the two images (**Figure 2-3**). Unfortunately the RMS error for these points ranges from 0.5693 to the relatively large value of 16.1168. Due to these points being meticulously matched according to features found in both images, this high RMS value is believed to be a result of non-linear image deformations in the 2010 image that occurred as a result of the plane moving as these data were collected. Once these points had been collected the 2010 image was warped to match its 2009 counterpart. The end results are areas in both the 2009 and 2010 scenes that are georeferenced to each other. Therefore, these scenes can be linked so that a pixel selected in one image will also be selected in the other image at the same latitude and longitude. Once this image linking has taken place, image deconvolution had been performed to establish mineral percentages in each dataset to establish mineral percentages. A 20 by 20 pixel square region of interest was created in the same area in both the 2009 and 2010 scenes, mineral percentage values within each region were analyzed, and a table was created in Microsoft Office Excel to better compare these values.

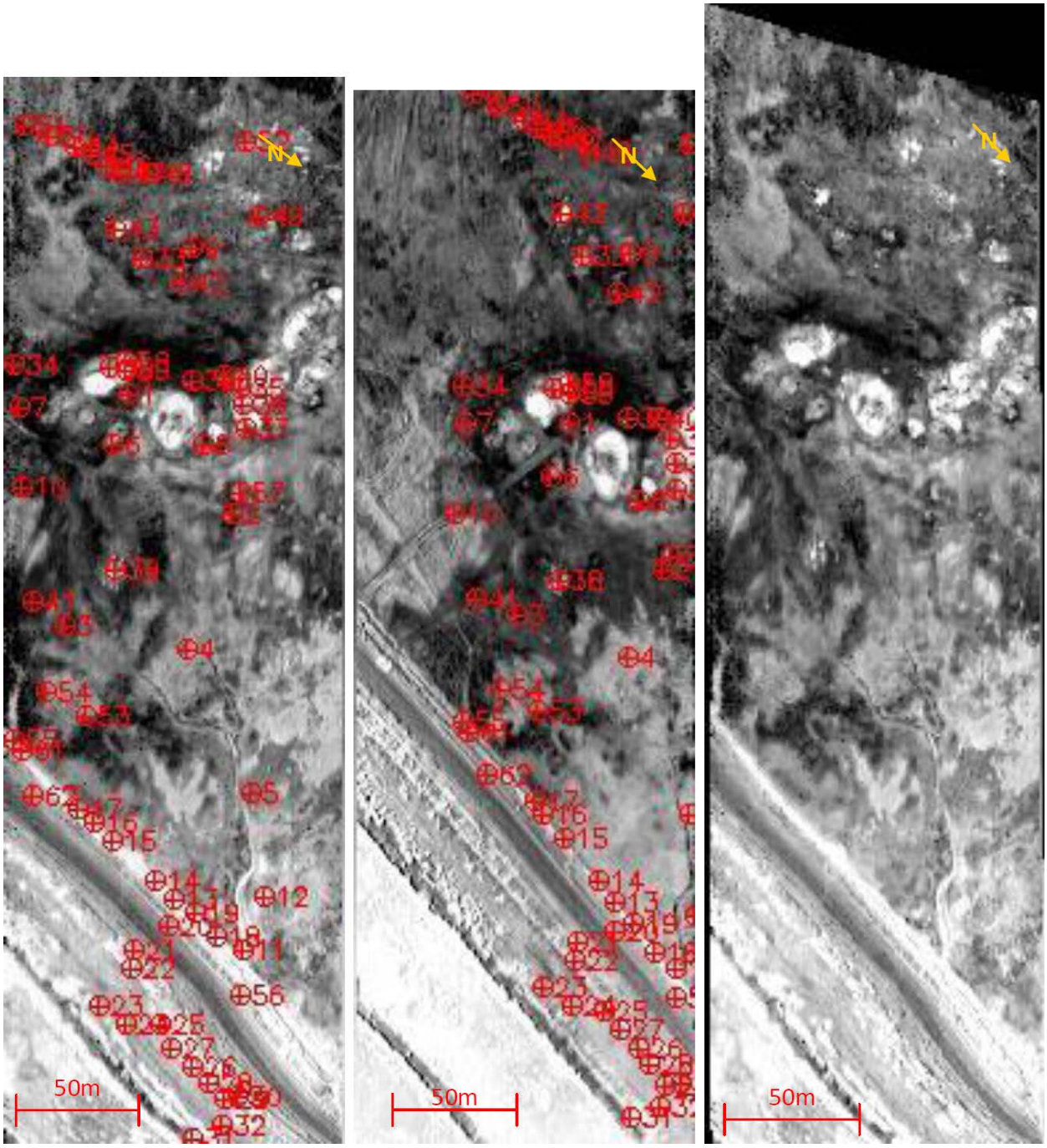

Figure 2-3: SEBASS dataset of the Davis-Schrimpf geothermal field in channel 10 (8.1956µm), these images were obtained March 26, 2009 (center) and April 6, 2010 (Right and Left). The image on the left is the 2010 image that has been deformed due to flight error; the 62 georeferencing points are shown. The image in the center is the 2009 base image with georeferencing points. The image of the right is the 2010 image once it has been warped.

2.2.4 Spectral Matching

The next method utilized on the SEBASS data was to degrade it to the spectral resolution of the MAGI sensor and the ASTER sensor in the TIR. This was performed by creating a new file using the SEBASS data, but only selecting the channels that are closest to the MAGI/ASTER channels centers to be a part of the file. The new file with a lower spectral resolution was subjected to the same processes as the original SEBASS data to derive emissivity data. Mineral maps, created using the linear deconvolution process with the same end-members were produced for the MAGI emulated data. Due to the ASTER data only having five channels in the TIR, only four end-members can be used in the linear deconvolution process at a time. Although this creates difficulties directly comparing maps, by going through the deconvolution process three times, each with different end-members, a viable comparison was made. The 2009 and 2010 scenes of the Davis-Schrimpf field were analyzed with this method. In each dataset three regions of interest are created based on surface features and regions of mineralogy found with image deconvolution in the SEBASS data. The first region encompasses the area that was identified as having relatively higher percentages of kaolinite, in the 2009 image the region is 6183 pixels and in the 2010 image the region was split into two separate areas above and below the main vents and encompasses 10,088 pixels. The second region consists of the main vent area in the center of the scene; this region is 2206 pixels in the 2009 data and 3384 pixels in the 2010 data. Finally the third region is an area found to be high in anhydrite and quartz and can be thought of as the typical background mineralogy in these Salton Sea geothermal fields, it is 8647 pixels in the 2009 data and 7614 pixels in the 2010 data. These spectrally differing mineral maps were then compared visually through RBG versions combining separate end-members, as well as analytically by recording end-member percentages of each region.

2.3 FIELD METHODS

The Davis-Schrimpf Geothermal field was visited on two separate occasions, March 13, 2010, and June 30 to July 2, 2010. On each of these occasions several methods were employed in order to better understand the area, and to perform proper verification and validation of the data acquired by the SEBASS sensor during its over-flights of the area.

Upon arrival the geothermal field was photographed and observed. During the March 13th visit, which was following 1.3" of rain on March 8th (National Weather Service, 2011), the mudpots formed large pools around the gryphons (**Image 2-!**). Where as in July, this water had receded within these mudpots and could be found several feet beneath the surface plane (see **Figure 1-4**). In order to better catalog and analyze the area, four distinct regions of increased geothermal activity were chosen and labeled as regions 1-4 (**Figure 2-4**), in these areas a significant degree and geothermal activity was observed. Various samples of mud from active gryphon slopes, liquefied mud within the gryphons, and mud surrounding the mudpots were taken from each region. Surface samples were also collected in areas outside of the 4 active regions to act as background surface samples.

Thermal readings were recorded of active gryphon vents, mudpots, fumaroles, gryphon slopes, and the background surface in the area after retrieving these samples. Thermal readings were done by using both a thermocouple instrument and the Forward Looking InfraRed (FLIR) thermal camera. The FLIR camera used for this analysis was the FLIR ThermaCAM™ S40, which has a 24 by 18 degree instantaneous field of view (IFOV) and a spatial resolution of 1.3

mrad. The thermal camera has the ability to detect thermal features with the precision of 0.1°C between the 7.5 to 13 µm region. In order to prevent saturation from temperatures too high or low, there are multiple gain settings that adjust the temperature range being collected. The thermocouple was used as a probe to provide instant subsurface temperature measurements; the FLIR camera provided thermal images and videos of features, which provided accurate surface temperature measurements of everything in the field of view. Thermal images were taken of gryphon vents and mud pots, whereas thermal videos were taken to capture the thermal flux of actively degassing gryphon vents. Five separate points were examined in a thirty second long thermal video of a degassing gryphon vent in region 3, thermal flux was recorded at each. These videos and images were further analyzed back at the laboratory.

Image 2-1 : March 13, 2010 ground photo of the Davis-Schrimpf geothermal field. In the foreground is the geothermally active region 2. A mound building gryphon is surrounded by water-dominated mudpots.

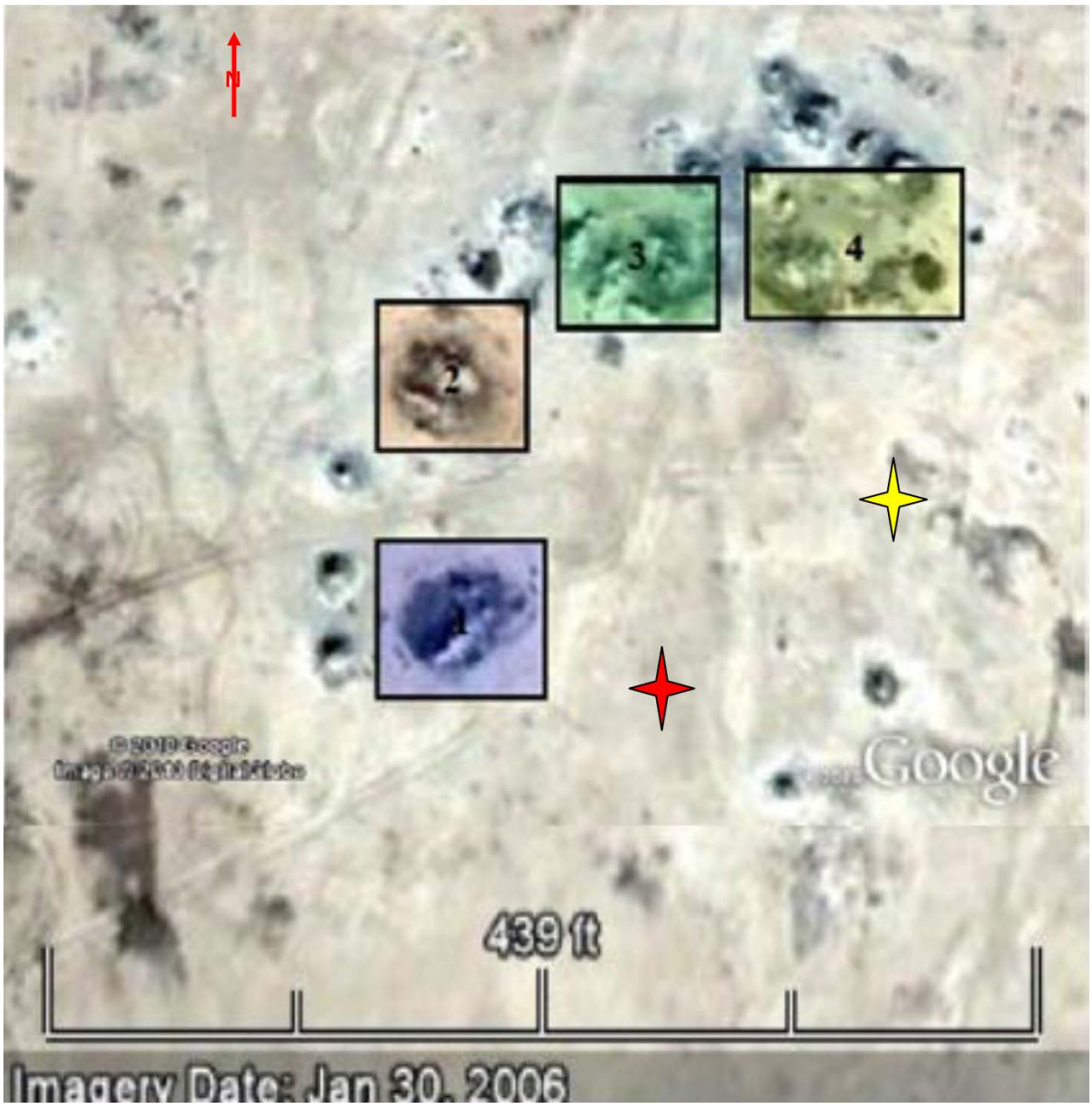

Figure 2-4: (©Google Earth 2010) This figure shows the four regions of increased geothermal activity as classified by the field study. The red marker shows the location of a surface sample taken March 13, 2010 and the yellow marker is the location of a surface sample taken July 2, 2010

2.4 LABORATORY METHODS

2.4.1 Spectrometer Methods

Several laboratory methods were used to better understand the composition of the samples collected from the Davis-Schrimpf Geothermal area. Thermal emission spectra of four of the samples collected in March and July were recorded using a Fourier-Transform Infrared (FTIR) spectrometer (King et al., 2004). The TIR spectra of the samples were collected in the Image Visualization and Infrared Spectroscopy (IVIS) laboratory at the University of Pittsburgh using a Nicolet Nexus 670 FTIR spectrometer with a potassium bromide (KBr) beam splitter in combination with a Mercury-cadmium-telluride (MCT)-B detector (allowing data from 5-25 μm) (Carter, 2008). In order for the spectrometer to receive an adequate signal from the sample, there must be a large difference in temperature between the two. Thus, the sample was pre-heated in an oven at 75°C for 24 hours and the spectrometer detector was cooled via liquid nitrogen. Samples were placed on a heating stage and emission spectra were collected. This allows the samples to maintain their temperature throughout the collection period and reduces any temperature mixing that may occur from readings being recorded at differing temperatures. Furthermore, the spectra were collected in the controlled environment of a glove box, which was purged of water vapor and carbon dioxide. To derive the instrument response function, a two temperature approach was used by scanning a blackbody at 70°C and 100°C (Ruff et al, 1997). This function was then used to produce a calibrated emissivity spectrum. This instrument response function was re-calculated any time the instrument temperature changes by 1°C. After following these steps the process yields a combined error of no more than 2% (Ruff et al., 1997).

Standard spectrum collection includes an initial black body calibration spectrum, followed by 256 scans of an individual sample to produce an average final spectrum.

The radiance data of each spectrum was then saved using OMNIC processing software and imported into the VM program, created by Arizona State University. Using the VM software, the two blackbody radiance files were used to create the response function, which then allowed a calibrated emissivity spectrum to be created for each sample. This data was then saved as an ASCII format file, which was then imported into Microsoft Excel for spectral analysis.

2.4.2 Scanning Electron Microscopy (SEM) Methods

A full elemental SEM analysis was also performed on five grains of the March background sample at the Material Micro-Characterization Laboratory (MMCL), which is part of the University of Pittsburgh Swanson School of Engineering. The SEM method was performed on Philips XL-30 field emission scanning electron microscope, which has detectors for imaging in secondary electron (SE) and backscatter detector (BSE) modes. The SE mode gives the highest resolution image and penetrates into the sample tens of nanometers where the BSE mode is used for element recognition, this is generated from a greater volume of electrons and penetrates around 1 micrometer deep. SEM allows specific elements found in grains of the sample to be identified by interpreting the energy signals produced by energy-sample interactions where the incident electrons from the electron microscope are decelerated in the sample (Edgerton, 2005).

2.4.3 X-Ray Diffraction (XRD) Methods

Once SEM analysis had identified elements found within the sample, XRD was used to identify specific minerals within the sample. In the XRD process a Philips X'pert Diffractometer dedicated to powder samples was used in the MMCL laboratory. The sample was broken apart into powder sized particles and then placed on a black silicon base that was cut specifically to prevent any interference with readings during analysis. Diffraction patterns were recorded by step scanning from 10 to 80°2θ, with a step size of 0.02° and counting for 5 seconds per step. As the experiment ran, the number of diffracted counts per second occurring at each step was recorded. Minerals were identified based on the location and size of peaks of counts per second (at the specific °2θ) and compared with a large library of natural and synthetic minerals. The comparison of minerals in the XRD library were constrained to only those that contained elements found in the SEM analysis.

3.0 RESULTS

3.1 DATA PROCESSING RESULTS

A thermal chronology of various thermal regions in the Salton Sea was created by collecting the temperatures of the geothermal field, background surface and Salton Sea water regions for the seven available years of scenes in the possible 11.5 year window of ASTER nighttime data (**Graph 2-1**). By examining the trends of the water, surface and geothermal temperatures there was found to be a strong correlation between the background surface and geothermal temperatures, but not with water temperatures. The geothermal field was continuously 1 to 6°C warmer then the background surface temperatures, which are heated primarily by solar heating (**Graph 3-1**). Due to the temperature error range of this process of 1-2°C (Vaughn et al., 2010) this continuously 1-6°C hotter area of 90 m^2 over seven years of data is enough to demonstrate that geothermal heating of the area has occurred for the past seven years. It also validates that the spikes of geothermal heating found in **Figure 3-1**, which has a temperature difference of just over 4°C in some places, are true. The ASTER analysis uses the temperature data extracted from the emissivity normalization process, the SEBASS analysis relies on emissivity data from the same process.

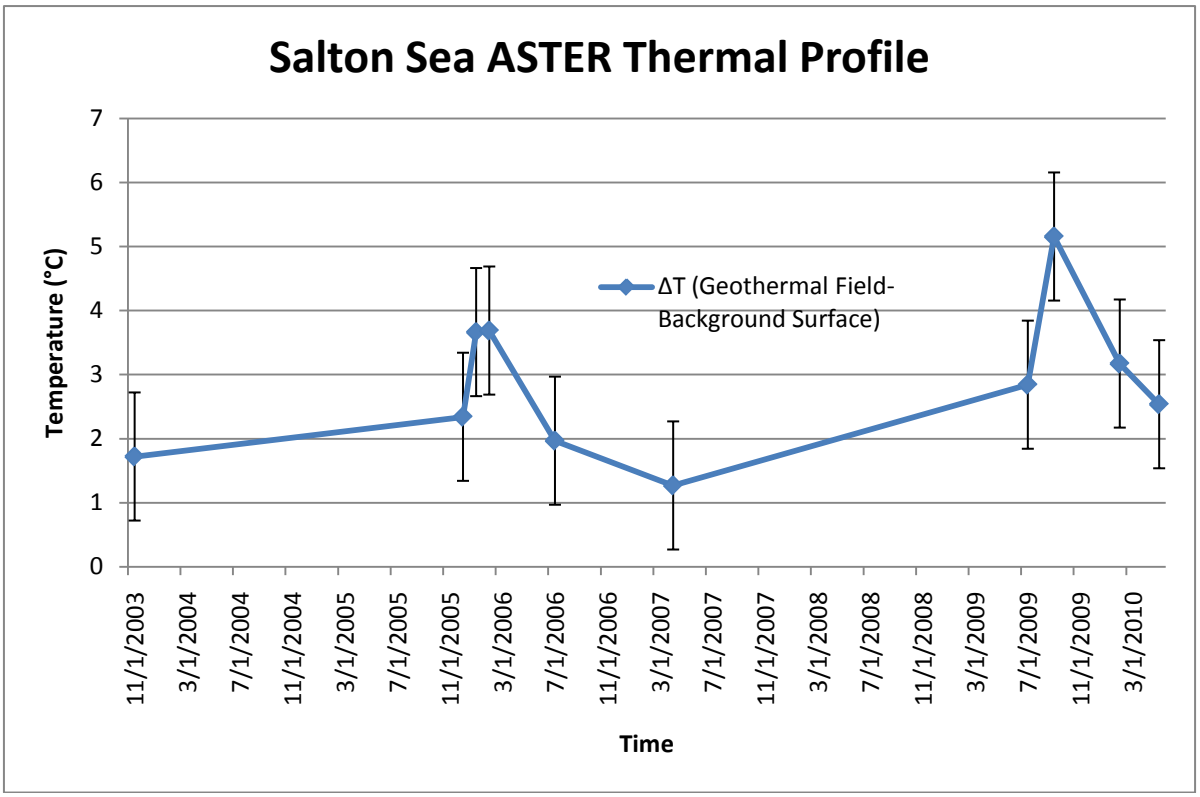

Graph 3-1 : ASTER data derived from temperature data graphed over seven years of data available. This graph clearly demonstrates the difference between the background surface temperature and the geothermal field temperature. Over the seven years there are times where the temperature difference increases, due to fluxes in geothermal activity. Error bars indicate the average error for ASTER TIR data (±1°C).

Pure mineral spectra (**Graph 3-2**) were chosen as end-members in the linear deconvolution process based on spectral compatibility with ground spectra found within the March 26, 2009 dataset (**Graph 3-3**). Maps correlating to each mineral end-member as well as the blackbody end-member and the RMS (error) scene were created (**Figures 3-1 and 3-2**) by running an image deconvolution function upon the 2009 and 2010 datasets. The lighter regions in the RMS map, which relate to areas of higher error, were compared to each end-member map to determine if some classifications were made with a higher degree of error. Detailed analysis of these mineral maps allowed some interesting results to be observed. First, anhydrite was found in large percentages surrounding geothermally active areas. This also holds true for the Sandbar geothermal area located northwest of the Davis-Schrimpf field (**Figure 3-3**). Gypsum can typically be found on the surface as a result of the evaporitic environment of the Salton Sea Trough in non-geothermally active, vegetation free zones (Herzig et al., 1988). This suggest that in geothermally active areas, gypsum ($CaSO_4 \bullet 2H_2O$) is being replaced by anhydrite ($CaSO_4$). This occurs because the original gypsum deposits became dehydrated as a result of hydrothermal alteration or surface heating from a time where the gypsum was exposed to the surface.

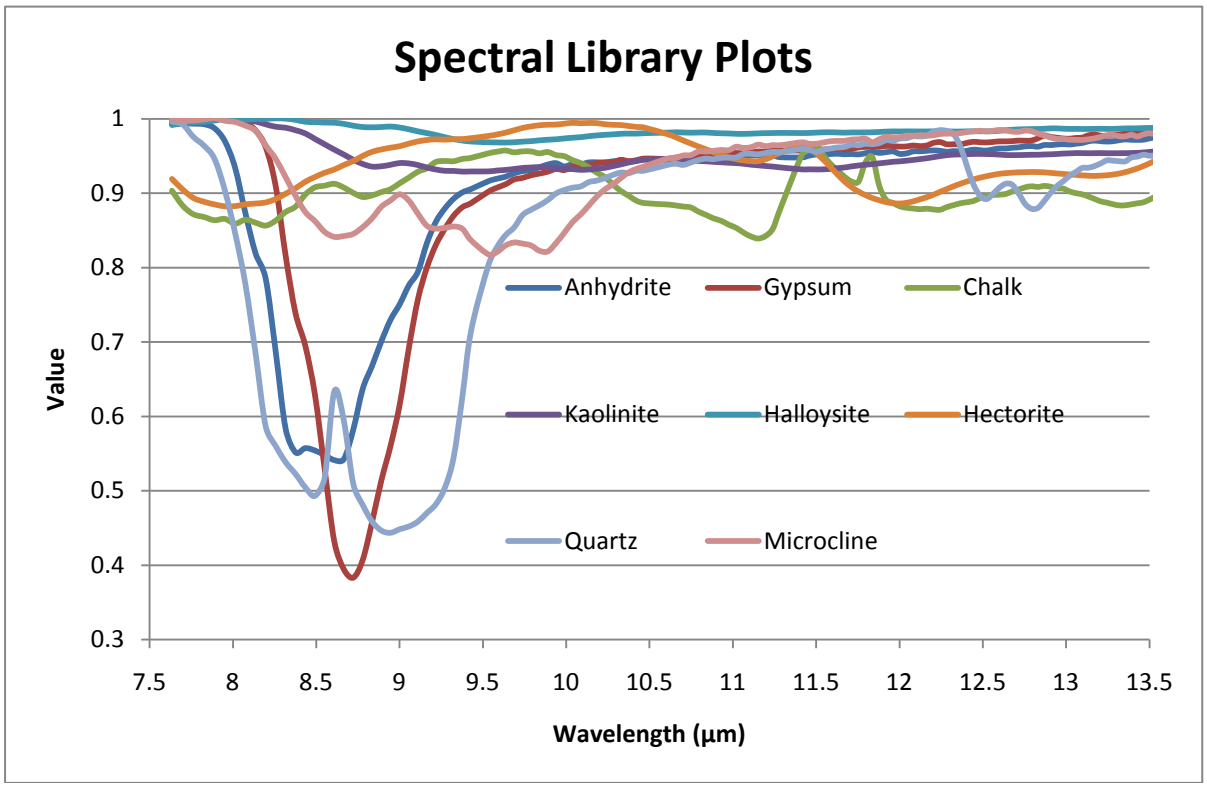

Graph 3-2 : Spectral plot of the end-member spectra.

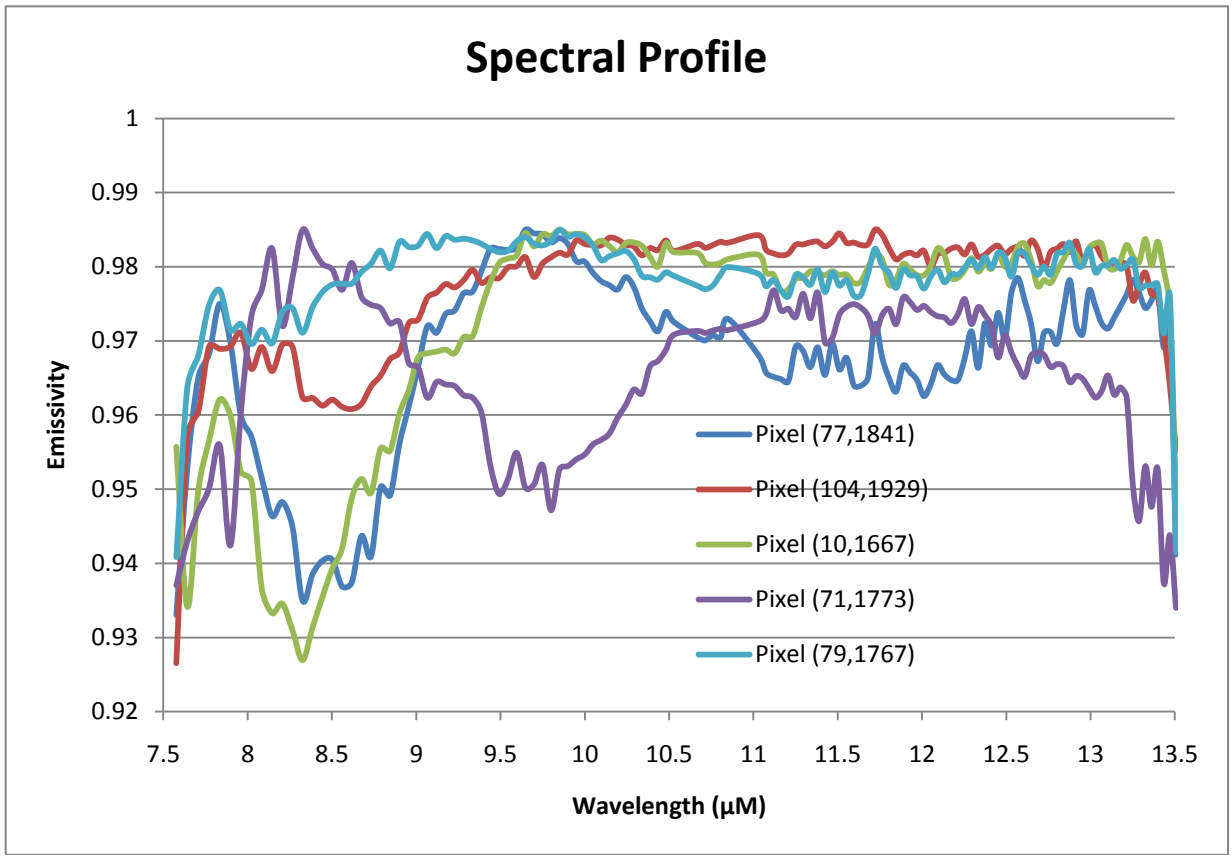

Graph 3-3 : A sampling of SEBASS derived spectra found in areas of differing color in the geothermal field upon performing a decorrelation stretch on the March 26, 2009 dataset.

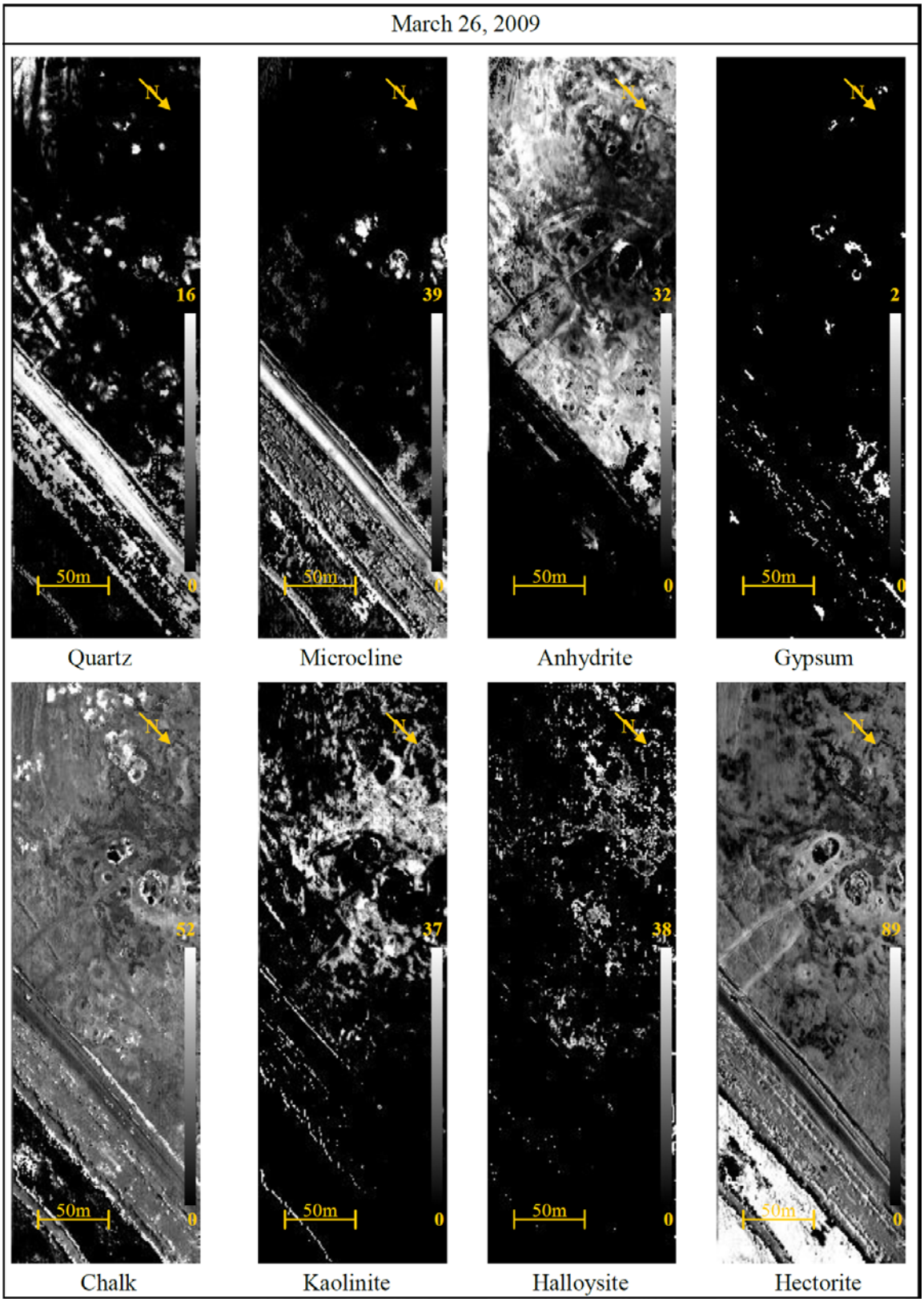

Figure 3-1: Continued on next page

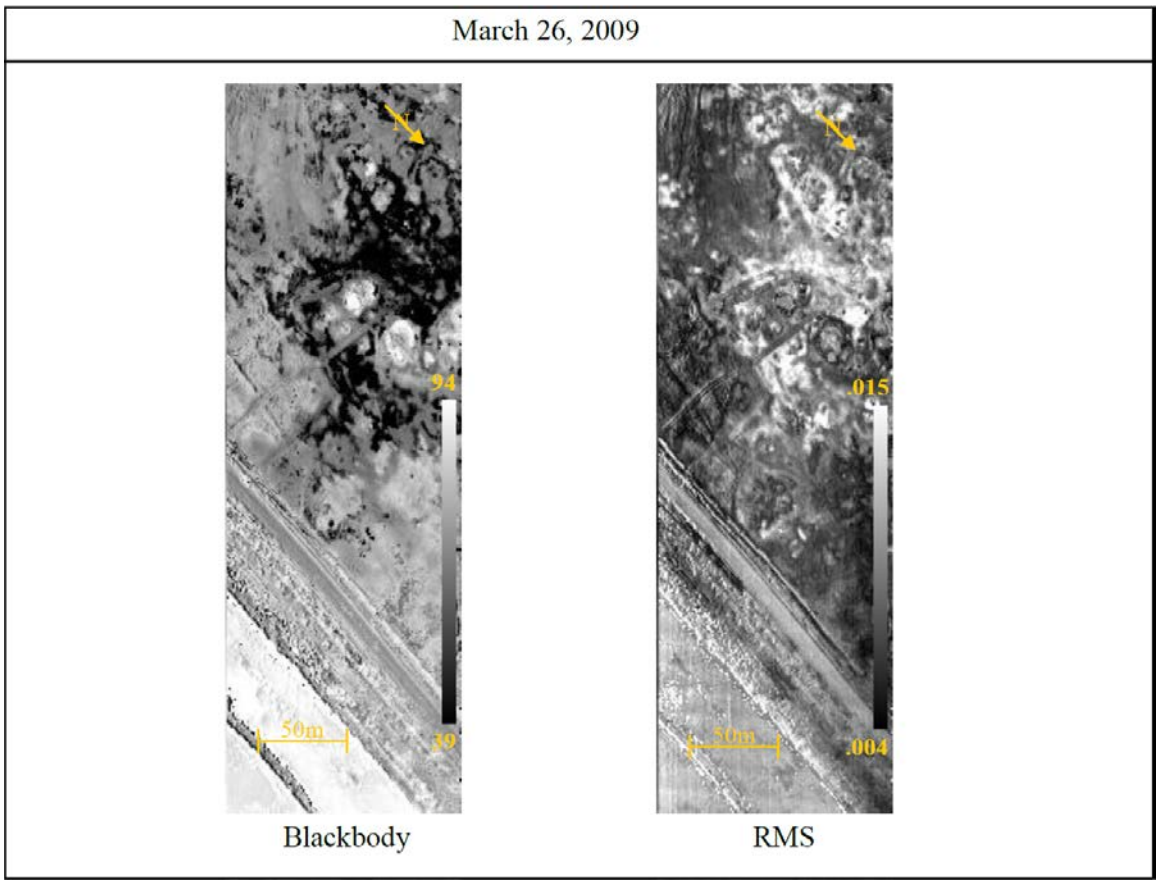

Figure 3-1: Mineral maps of the Davis Schrimpf geothermal field derived from the SEBASS dataset collected March 26, 2009. On the right on each map is a color gradient ramp that shows the dynamic ranges of mineral percentages found on each map. The light areas in the kaolinite and RMS maps correlate, meaning that the surface mineral being characterized as kaolinite is most likely a different mineral. Anhydrite can also be found in large amounts surrounding the geothermal field, where as gypsum, its hydrated counter-part, and is only found in very low percentages surrounding mud pots**.**

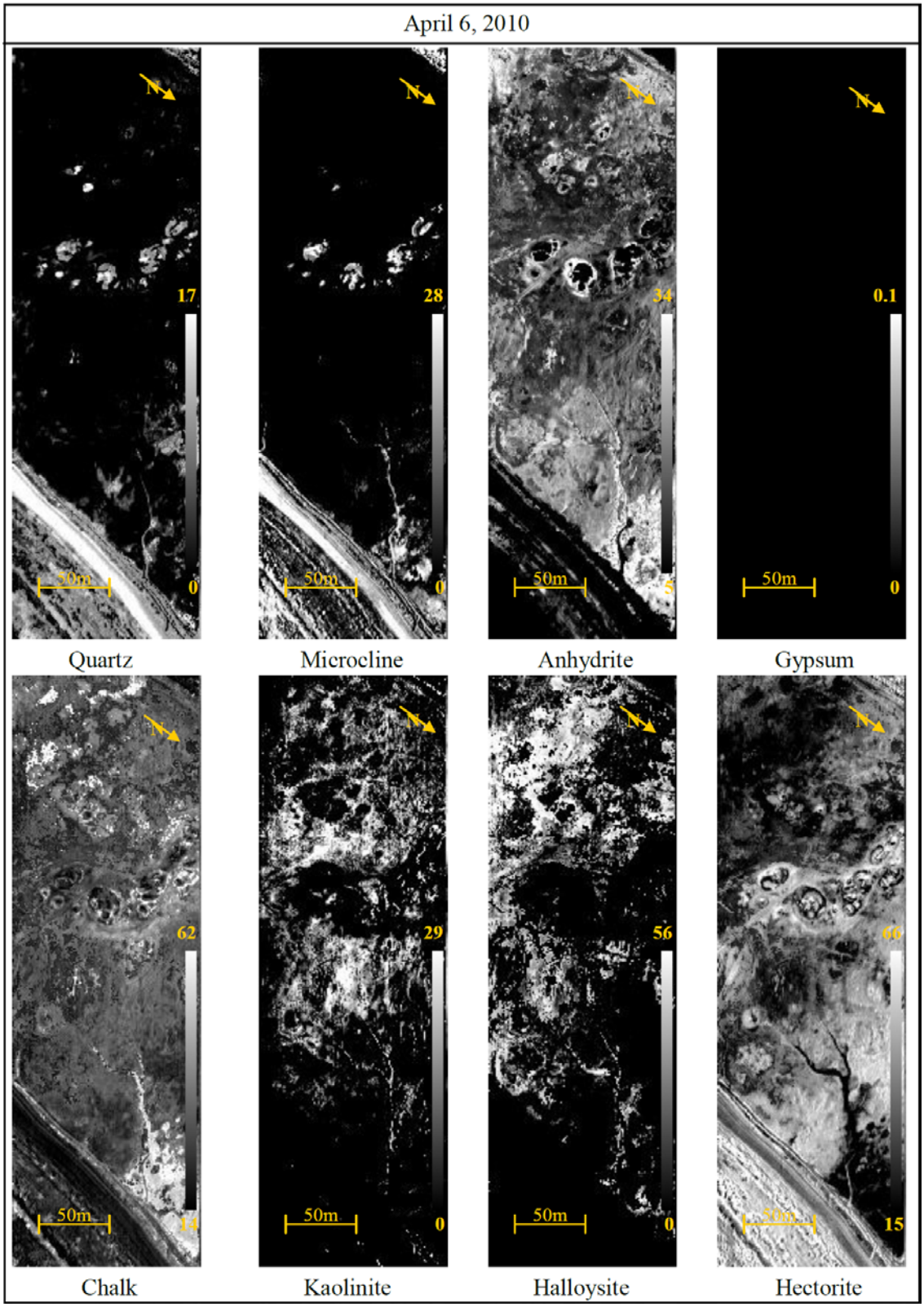

Figure 3-2: Continued on next page

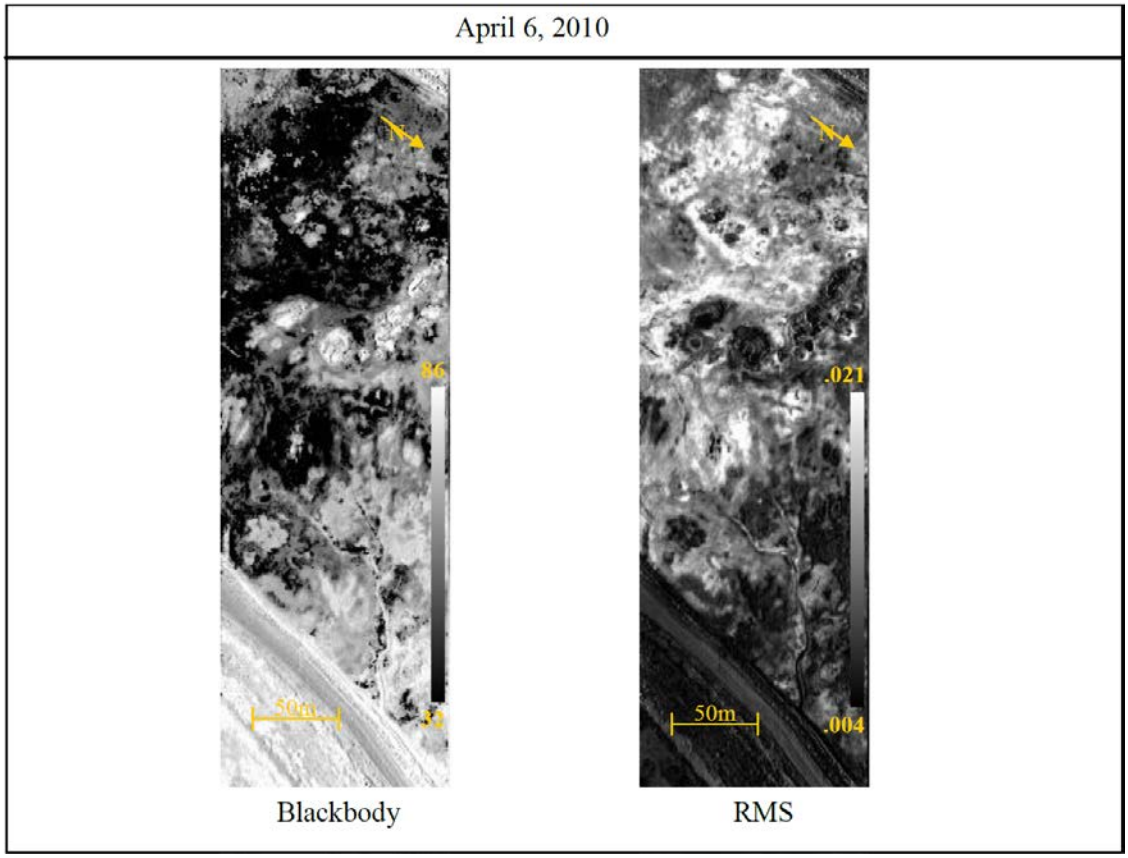

Figure 3-2: Mineral maps of the Davis Schrimpf geothermal field derived from the SEBASS dataset collected April 6, 2010. On the right on each map is a color gradient ramp that shows the dynamic ranges of mineral percentages found on each map. Once again areas of higher value in the RMS map correlate to area with higher percentage of the mineral kaolinite. Anhydrite can once again be found in abundance and gypsum is not detectable at all.

Second, an unidentified mineral was found surrounding active vents. Due to this mineral having a short TIR wavelength absorption feature around 8.2 μm in its emission spectrum (**Graph 3-4**) it does not match any emission spectrum currently in the spectral library. This causes the unidentified mineral area to show up very clearly in RMS images as a lighter area, signifying a higher amount of error (**Figures 3-1 and 3-2)**. In the cases of the 2009 and 2010 datasets of the Davis-Schrimpf field it was apparent upon comparing the RMS map to the other mineral maps, that the area that had been identified as kaolinite correlated strongly to areas of high error (**Figures 3-1 and 3-2)**. The kaolinite end-member was misclassified and truly represents the surface area rich in the unknown mineral. The same event occurs upon analyzing the 2010 mineral maps of the Sandbar geothermal field, an unidentified mineral surrounds active vents and has a peculiar spectrum with the same 8.2 μm absorption feature. The only difference was that the unidentified mineral had been classified dominantly as the halloysite end-member in these mineral maps (**Figure 3-4)**. Much like anhydrite, which was located only in geothermal fields, this unknown mineral can also only be found surrounding geothermally active areas in the Salton Sea.

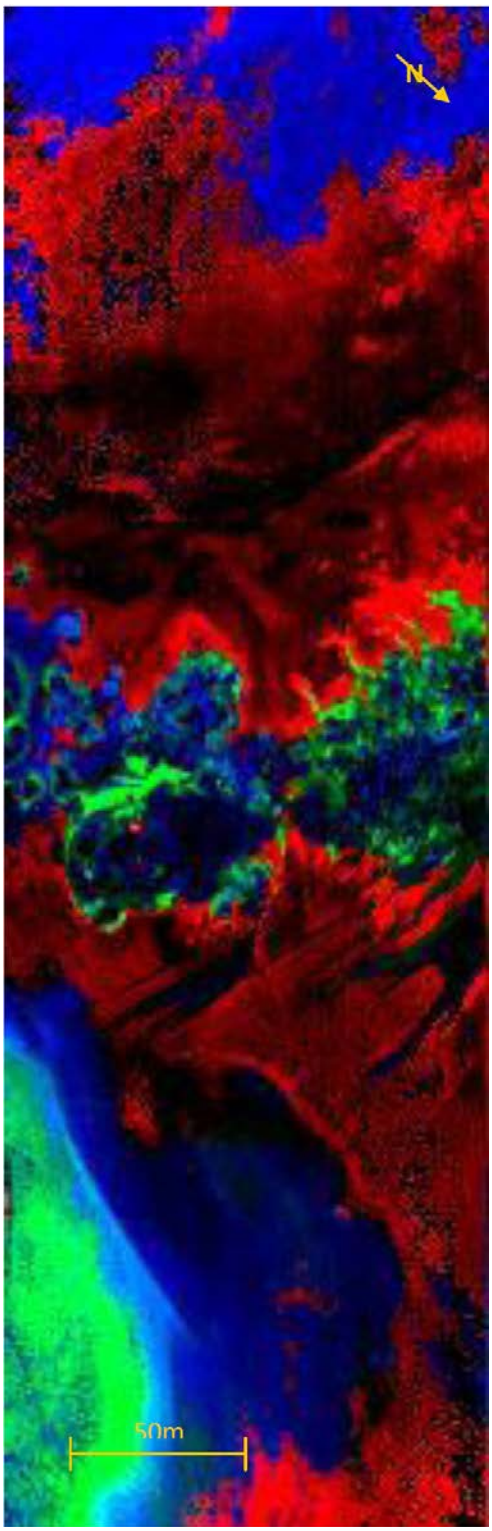

Figure 3-3: SEBASS scene of the Sandbar Geothermal field, April 6, 2010. R: anhydrite, G: gypsum, B: quartz. Notice the large amounts on anhydrite found surrounding this geothermal field in this region as well as in the Davis-Schrimpf field anhydrite maps in Figures 3-4 and 3-5.

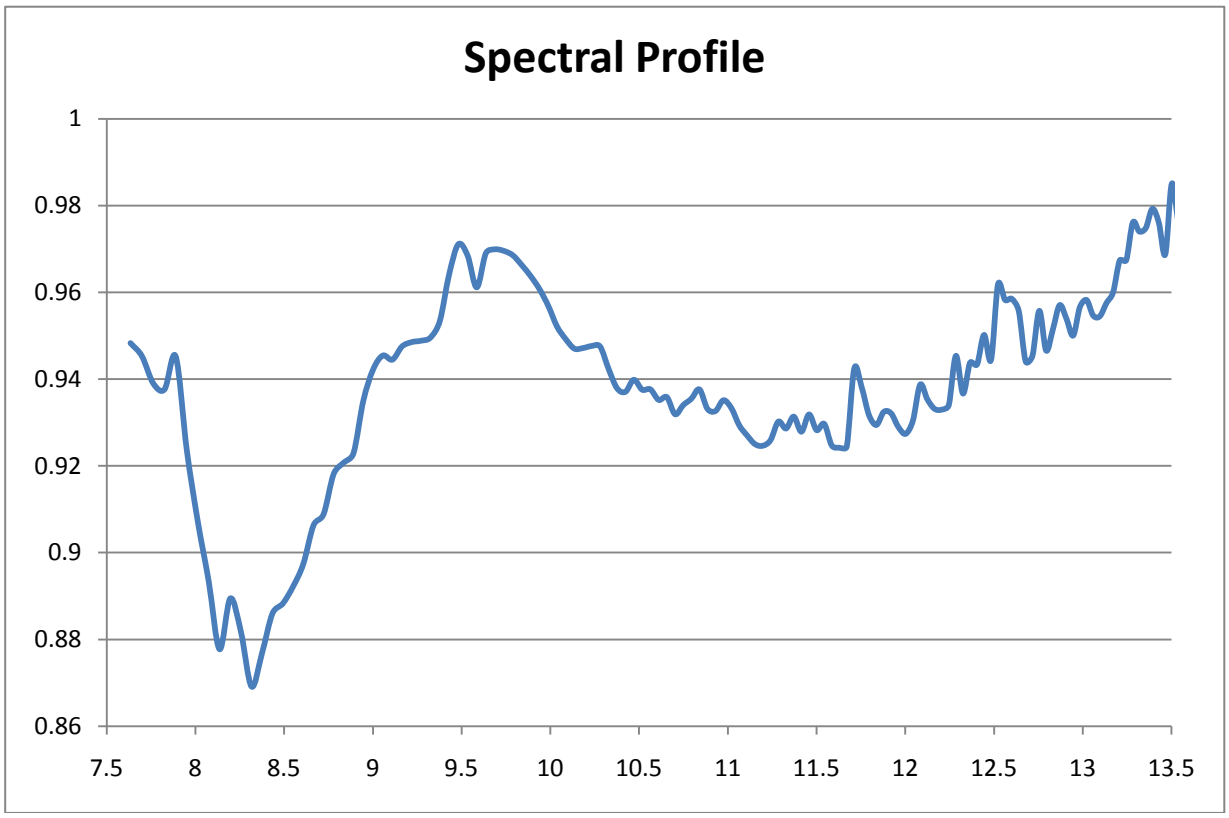

Graph 3-4 : Typical unknown mineral spectrum, taken from a pixel in an unidentified mineral rich area of the Davis-Schrimpf field dataset collected April 6, 2010. Note the short TIR wavelength absorption feature occurring at approximately 8.2µm.

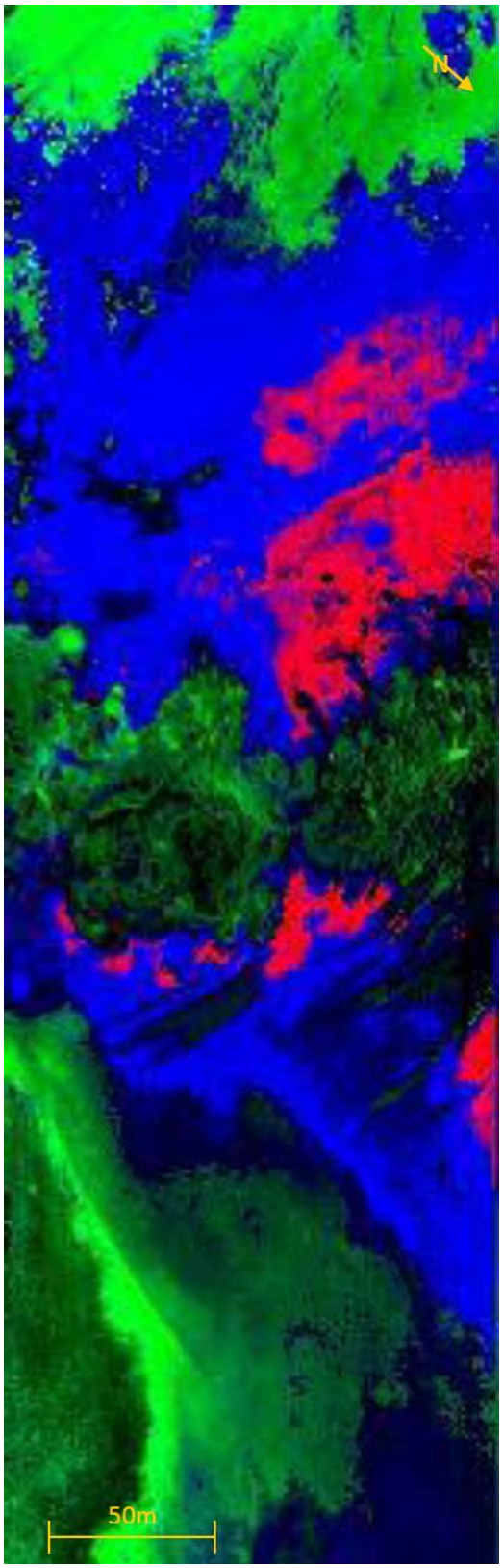

Figure 3-4: SEBASS scene of the Sandbar Geothermal field, April 6, 2010 R: halloysite, G: quartz, B: chalk

A discrepancy in the amount of area covered by each mineral end-member was noted upon comparing the 2009 and 2010 maps. By comparing the ROI in the 2009 scene to the same area in the warped 2010 scene (**Figure 3-5**) not only was the change observable, but there was also a change in mineral percentages on the surface (**Table 3-1**). The most substantial of these discrepancies was that of the area covered by the unidentified mineral or "kaolinite". In the area shared by both the 2009 and 2010 datasets the kaolinite area had grown from 9613 m^2 with a value above zero in 2009, to 17345 m^2 in the warped 2010 dataset. Within a year, this area had increased by slightly more than 80%. This 80% increase in kaolinite was found by examining mineral composition difference over the chosen region of interest as well. This demonstrates that the deposits from 2009 have not merely been spread out over the surface through weathering effects; rather, new deposits had formed on the surface before the 2010 overpass.

Emulated MAGI and ASTER TIR data derived from SEBASS data gives an accurate representation of how the spectral resolution of these two sensors would affect the interpretation of the pre-determined mineral end-members. At a TIR spectral resolution of less than 32 channels, the spectral resolution becomes too low to accurately identify specific minerals.

A certain degree of data loss was observed with each step upon comparing the SEBASS, emulated MAGI (eMAGI), and emulated ASTER (eASTER) data. Only SEBASS and eMAGI data can be directly compared because the eASTER data do not having enough TIR channels to support the analysis using the full mineral suite. However, four minerals at a time can still be compared in eASTER. This allows for a basic understanding of how well these mineral can be indentified with the TIR spectral resolution of ASTER (**Figures 3-6 through 9 and Tables 3-2 through 7**). Using the linear deconvolution process results in a ±2.5% error for lab or high spectral resolution data, because of this any value below 5% cannot be accounted for with certainty.

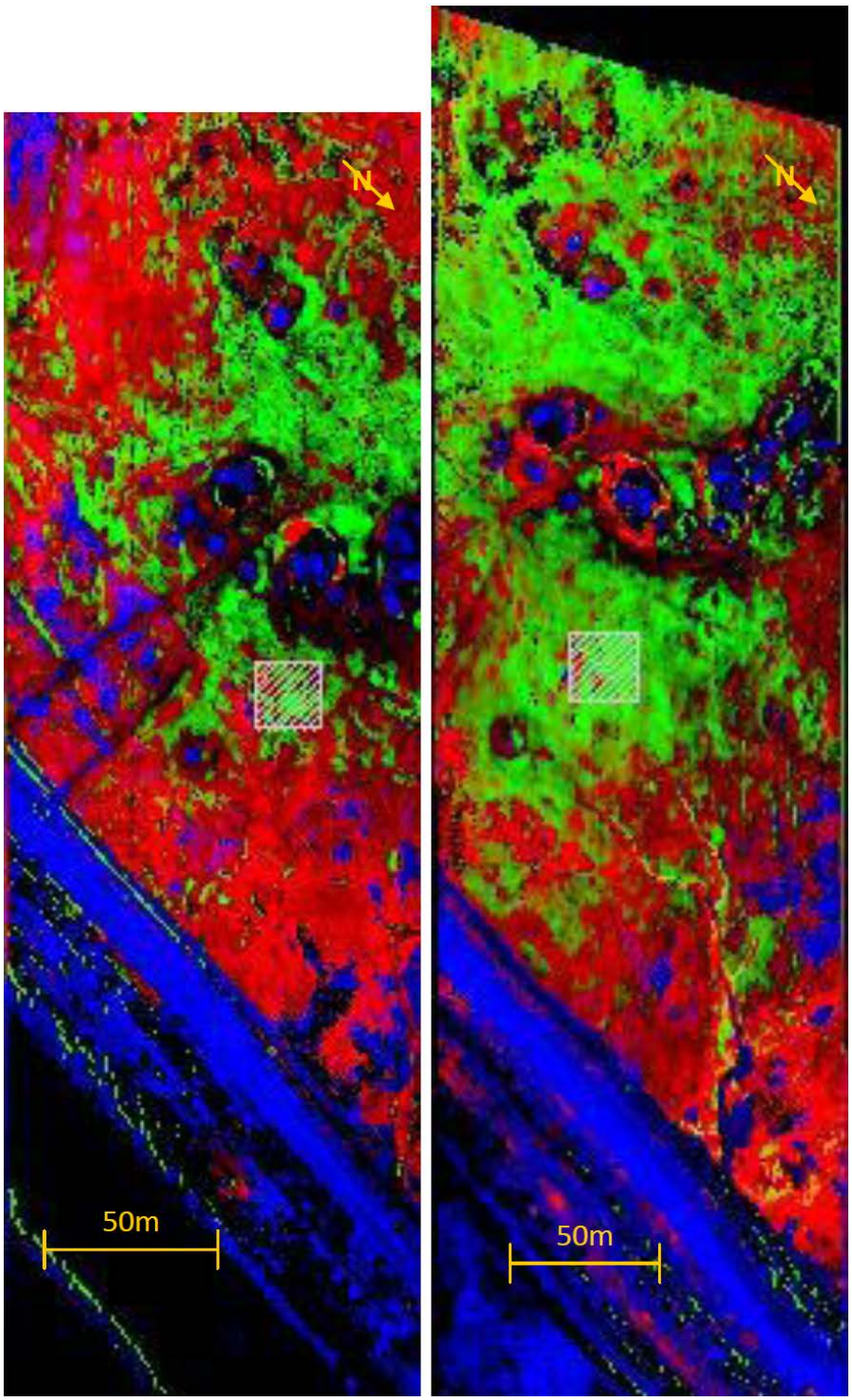

Figure 3-5: SEBASS scene of the Davis-Schrimpf Geothermal field, March 26, 2009 (left) and April 6, 2010 (right) R: anhydrite, G: kaolinite B: quartz. The white box found on these figures signifies the region of interest area where the mineral percentages in the correlating Table 3-1 were calculated.

Table 3-1: Mineral percentages calculated from the same area in the March 26, 2009 and April 6, 2010 data. Notice anhydrite maintains a near constant mineral percentage between the two datasets, whereas kaolinite increases rapidly.

Mineral Percentages within same Region of Interest		
Mineral	March 29, 2009	April 6, 2010
Quartz	0	0
Microcline	0	0
Anhydrite	12	9
Gypsum	0	0
Chalk	23	30
Kaolinite	18	32
Halloysite	3.	1
Hectorite	43	27

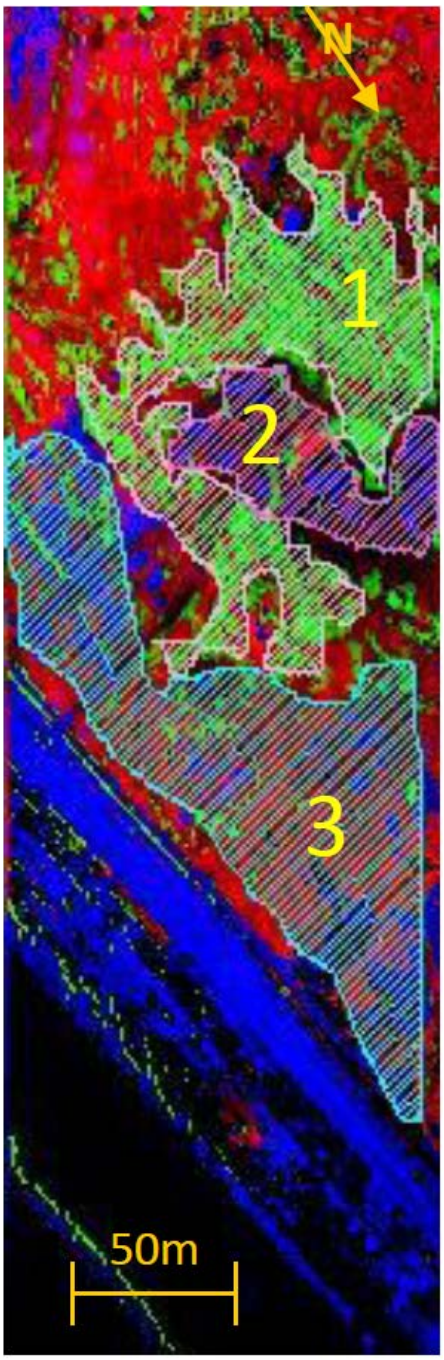

Figure 3-6: March26, 2009 SEBASS image of the Davis-Schrimpf field, R: anhydrite, G: kaolinite, B: quartz. Regions of interest are shown, which were analyzed for the average mineral percentages in the spectral resolution of all three sensors. The regions have been labeled with the same numbers they are referred to in the subsequent tables.

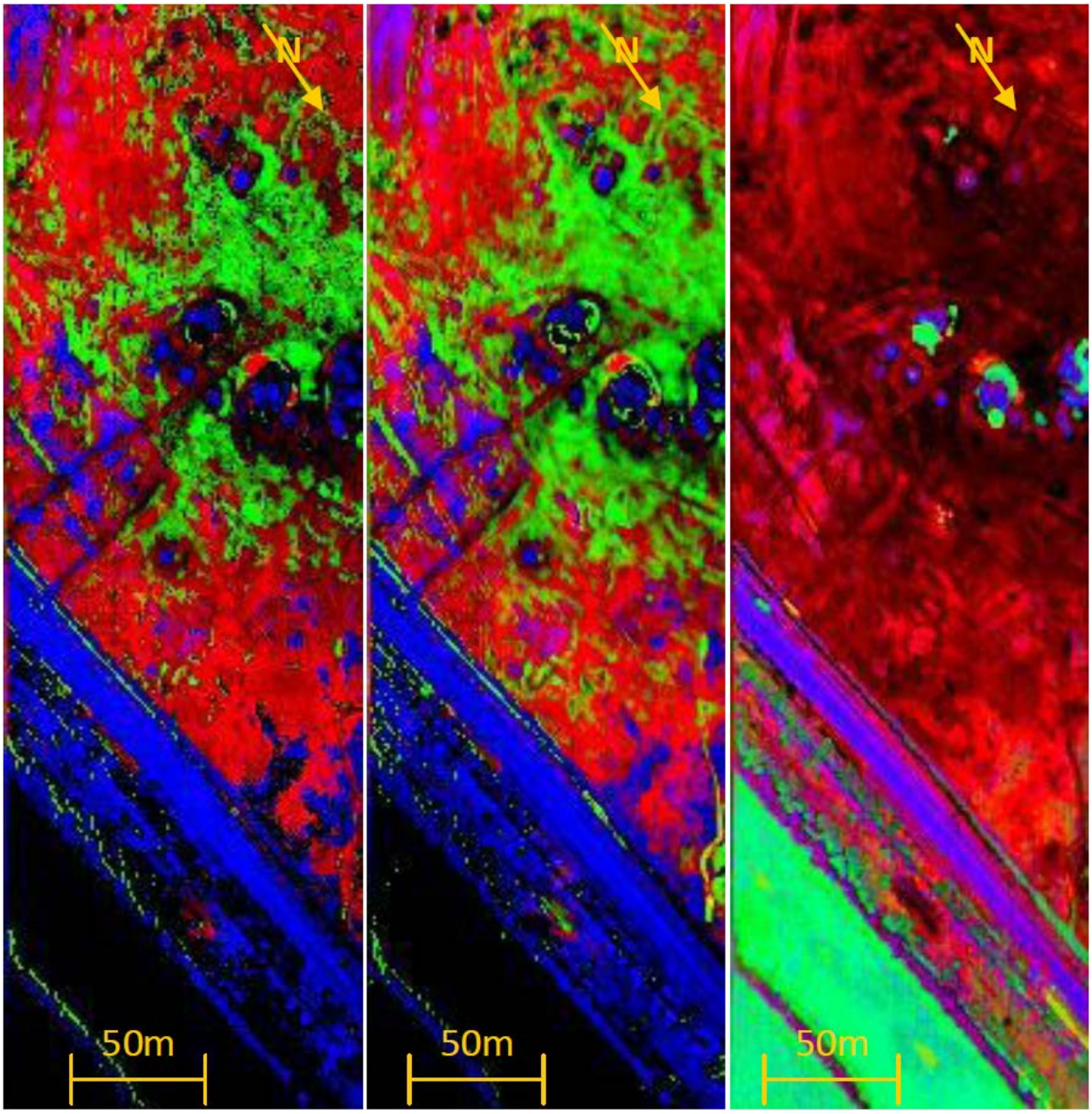

Figure 3-7: March 26, 2009 SEBASS image of the Davis-Schrimpf field, R: anhydrite, G: kaolinite, B: quartz. These maps are from the same area, at the same time, and map the same minerals in RGB. The only differing factor is the spectral resolution. These maps have the resolution of SEBASS (left), MAGI (center), and ASTER (right). Notice that where the left and middle maps look very similar, the right map looks entirely different**.**

Table 3-2: Numerical analysis of average mineral percentages of each region that were not identified as a blackbody end-member in region 2 of the March 26, 2009 map. Average RMS values are given as an indicator of error.

Region 1 2009 Mineral Percentage Comparisons					
Minerals	SEBASS	MAGI	ASTER(CKHH)	ASTER (QMAG)	ASTER (KCAQ)
Quartz	0	2	na	0	0
Microcline	0	3	na	2	na
Anhydrite	10	15	na	98	11
Gypsum	0	0	na	0	na
Chalk	23	31	49	na	87
Kaolinite	21	5	0	na	0
Halloysite	7	0	2	na	na
Hectorite	39	43	49	na	na
Blackbody	36	67	26	86	50
RMS	1.14×10^{-2}	5.26×10^{-2}	5.45×10^{-2}	1.84×10^{-2}	6.39×10^{-2}

Table 3-3: Numerical analysis of average mineral percentages of each region that were not identified as a blackbody end-member in region 2 of the March 26, 2009 map. Average RMS values are given as an indicator of error.

Region 2 2009 Mineral Percentage Comparisons					
Minerals	SEBASS	MAGI	ASTER(CKHH)	ASTER (QMAG)	ASTER (KCAQ)
Quartz	3	2	na	5	4
Microcline	9	10	na	20	na
Anhydrite	6	4	na	74	13
Gypsum	1	0	na	0	na
Chalk	27	27	40	na	71
Kaolinite	3	6	11	na	12
Halloysite	1	2	4	na	na
Hectorite	51	48	45	na	na
Blackbody	60	61	45	89	67
RMS	9.13×10^{-4}	6.58×10^{-3}	5.6×10^{-3}	9.87×10^{-3}	2.79×10^{-3}

Table 3-4: Numerical analysis of average mineral percentages of each region that were not identified as a blackbody end-member in region 3 of the March 26, 2009 map. Average RMS values are given as an indicator of error.

Region 3 2009 Mineral Percentage Comparisons					
Minerals	SEBASS	MAGI	ASTER(CKHH)	ASTER (QMAG)	ASTER (KCAQ)
Quartz	2	2	na	0	1
Microcline	2	3	na	4	na
Anhydrite	20	15	na	96	24
Gypsum	0	0	na	0	na
Chalk	27	31	69	na	74
Kaolinite	2	5	1	na	1
Halloysite	1	0	0	na	na
Hectorite	44	43	29	na	na
Blackbody	73	67	53	89	67
RMS	7.65×10^{-3}	6.58×10^{-3}	1.01×10^{-2}	8.86×10^{-3}	3.44×10^{-3}

.

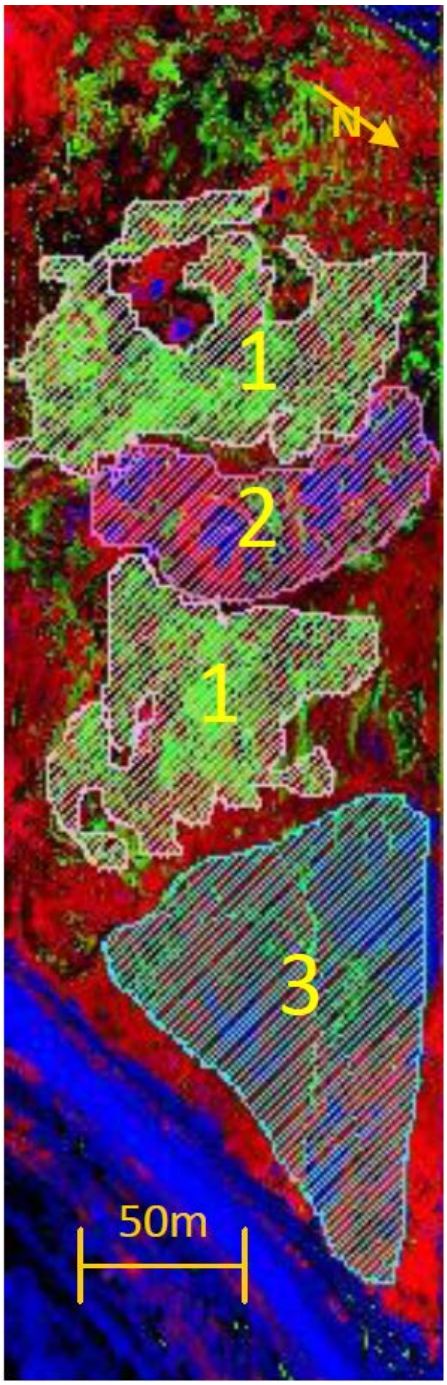

Figure 3-8: April 6, 2010 SEBASS image of the Davis-Schrimpf field, R: anhydrite, G: kaolinite, B: quartz. Once again, each region has been labeled with the numbers by with they are referred to in the latter tables. Note that region 1 covers two separate areas of similar mineralogy.

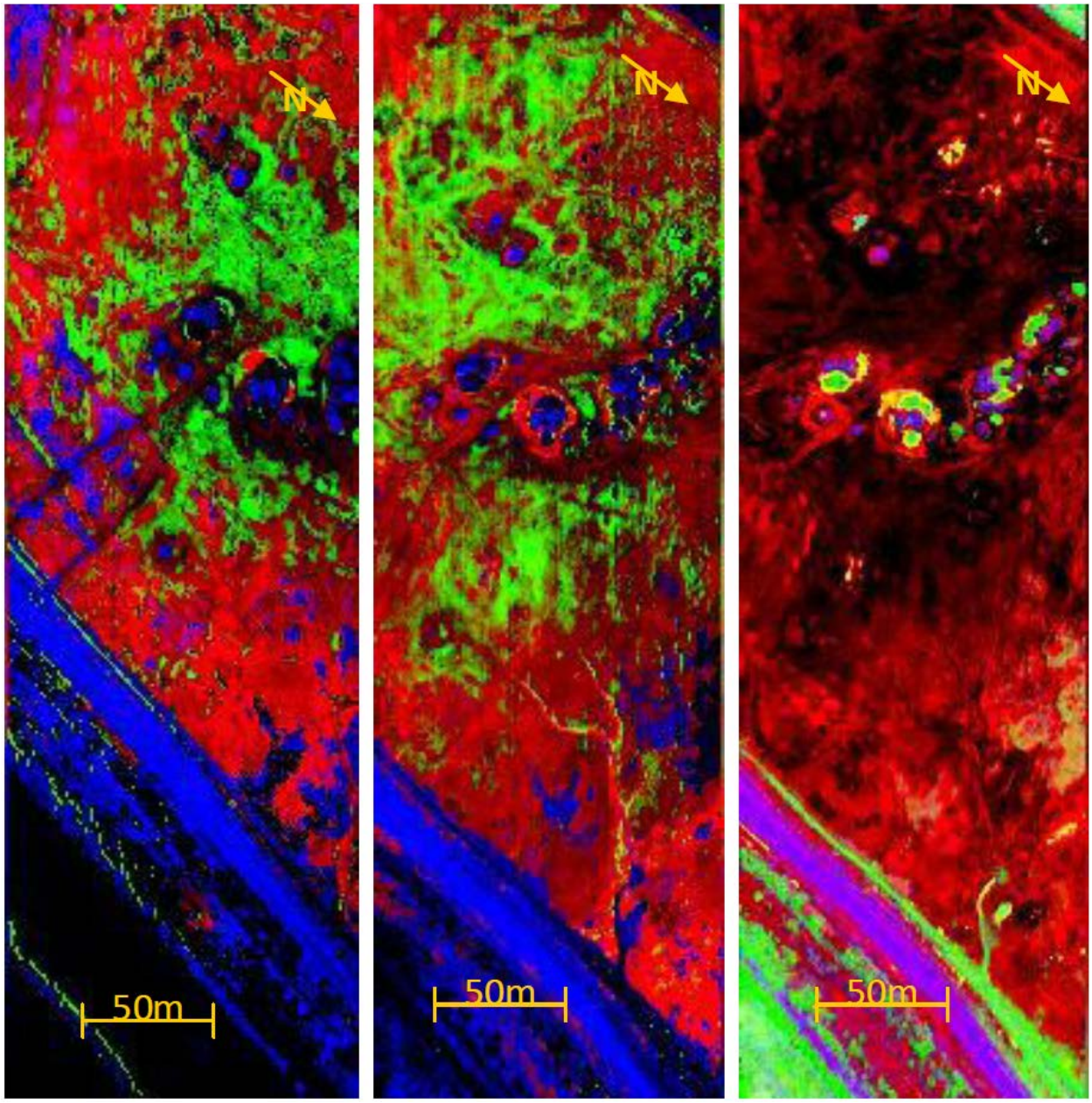

Figure 3-9: April 6, 2010 SEBASS image of the Davis-Schrimpf field, R: anhydrite, G: kaolinite, B: quartz. Once again, these maps are from the same area, at the same time, and map the same minerals in RGB. The only differing factor is the spectral resolution. These maps have the resolution of SEBASS (left), MAGI (center), and ASTER (right).

Table 3-5: Numerical analysis of average mineral percentages of each region that were not identified as a blackbody end-member in region 1 of the April 6, 2010 map. Average RMS values are given as an indicator of error.

Region 1 2010 Mineral Percentage Comparisions					
Minerals	SEBASS	MAGI	ASTER(CKHH)	ASTER (QMAG)	ASTER (KCAQ)
Quartz	0	0	na	0	0
Microcline	0	0	na	0	na
Anhydrite	13	12	na	89	9
Gypsum	0	0	na	0	na
Chalk	31	43	0	na	91
Kaolinite	13	12	0	na	0
Halloysite	16	0	31	na	na
Hectorite	26	34	69	na	na
Blackbody	29	42	0	80	58
RMS	1.46×10^{-2}	1.25×10^{-2}	1.03×10^{-2}	3.1×10^{-2}	1.53×10^{-2}

Table 3-6: Numerical analysis of average mineral percentages of each region that were not identified as a blackbody end-member in region 2 of the April 6, 2010 map. Average RMS values are given as an indicator of error.

Region 2 2010 Mineral Percentage Comparisions					
Minerals	SEBASS	MAGI	ASTER(CKHH)	ASTER (QMAG)	ASTER (KCAQ)
Quartz	3	2	na	5	2
Microcline	4	4	na	12	na
Anhydrite	13	9	na	82	18
Gypsum	1	1	na	1	na
Chalk	33	32	5	na	71
Kaolinite	3	2	5	na	9
Halloysite	1	1	23	na	na
Hectorite	42	48	66	na	na
Blackbody	62	57	17	86	69
RMS	9.57×10^{-3}	9.36×10^{-3}	7.9×10^{-3}	1.81×10^{-2}	1.02×10^{-2}

Table 3-7: Numerical analysis of average mineral percentages of each region that were not identified as a blackbody end-member in region 3 of the April 6, 2010 map. Average RMS values are given as an indicator of error.

Region 3 2010 Mineral Percentage Comparisions					
Minerals	SEBASS	MAGI	ASTER(CKHH)	ASTER (QMAG)	ASTER (KCAQ)
Quartz	2	1	na	2	0
Microcline	2	1	na	1	na
Anhydrite	21	15	na	97	23
Gypsum	0	0	na	0	na
Chalk	33	36	2	na	72
Kaolinite	1	1	4	na	4
Halloysite	4	2	19	na	na
Hectorite	37	43	75	na	na
Blackbody	66	62	20	90	74
RMS	$8.67x10^{-3}$	$8.02x10^{-3}$	$3.98x10^{-3}$	$1.08x10^{-2}$	$9x10^{-3}$

Both the SEBASS and eMAGI mineral maps are visually similar (**Figures 3-7 and 9**). Areas identified as being rich in anhydrite and kaolinite minerals in SEBASS data were comparable to the same areas in eMAGI data. There were, however, some slight variations. The eMAGI data assigned the kaolinite end-member slightly more area and muted the differences between minerals rich areas. In most cases, SEBASS and MAGI percentages were very similar (**Tables 3-2 through 7**). The percentage difference between minerals ranged from 0% to 16% and the majority of that difference is below 2.5%. In the March 26, 2009 data there was a percentage difference of 16% of kaolinite in the region containing large amounts of the unidentified mineral, which was classified as kaolinite (**Table 3-2**). Although this is a significant percentage difference, kaolinite was still identified in the same areas in both the datasets.

The eASTER scene was very different from the SEBASS data. Observing mineral maps at these two spectral resolutions and using the same three minerals in RBG, large variances are

seen (**Figures 3-7 and 9**). Anhydrite was positively identified in the eASTER data surrounding the geothermal field. However, anhydrite was also identified in every other area of the Salton Sea in this dataset as well. The unidentified mineral area surrounding the geothermal vents disappeared. The area in the SEBASS dataset that contained larger amounts of the unidentified mineral has values in eASTER that are slightly higher in the RMS map, this was similar to the higher spectral resolution RMS maps. However, other areas in the RMS map have values that are just as high and therefore the unknown mineral region could be easily overlooked without prior knowledge of an anomaly. The difference in percentage between the SEBASS and eASTER data range from 0 to 88% with a majority of the difference above 10% (**Tables 3-2 through 7**). In the eASTER data, pixels were also found to be less mixed and many regions had single mineral dominating all pixels in the region with percentages of 70% and up.

3.2 FIELD AND LABORATORY RESULTS

The temperatures found in gryphon vents using the thermocouple and FLIR thermal camera on March 13, 2010 and July 2, 2010 were 19-41°C above the background surface temperature of 20°C. Conversely, temperatures in the mud pots were 10-15°C cooler than the background surface temperature. The temperatures in the area derived from SEBASS data found mud pots to be 9-12°C cooler than the surrounding surface and gryphon vents 10-13°C warmer. Temperature flux of a vent captured by the FLIR thermal camera in region three was also analyzed and heat spikes as high as 10°C occurred above an actively degassing vent (**Figure 3-10**). Thermal photos of the same vent taken from an aerial position revealed the hottest spots of the gryphon vent to be

the same locations where degassing was occurring by bubbling out of the liquefied mud (**Figure 3-11**). Temperature as high as 61°C were recorded in the zones that were bubbling from active degassing whereas the liquefied mud in the vent surrounding these zones had temperatures ranging from 39 to 55°C on the surface. These temperatures were 19 to 35°C warmer than the recorded background surface temperature (20°C).

Samples collected from the March 13, 2010 and July 2, 2010 field expeditions were analyzed by the Nicolet Nexus 670 FTIR spectrometer in the IVIS lab at the University of Pittsburgh (**Graph 3-5**). One sample displayed the same short wavelength absorption feature displayed in the SEBASS data in these areas. This validated that this odd spectrum was in fact related to an unidentified mineral, not a sensor artifact. However, a sample that was obtained in July from the same relative position displayed no such absorption feature.

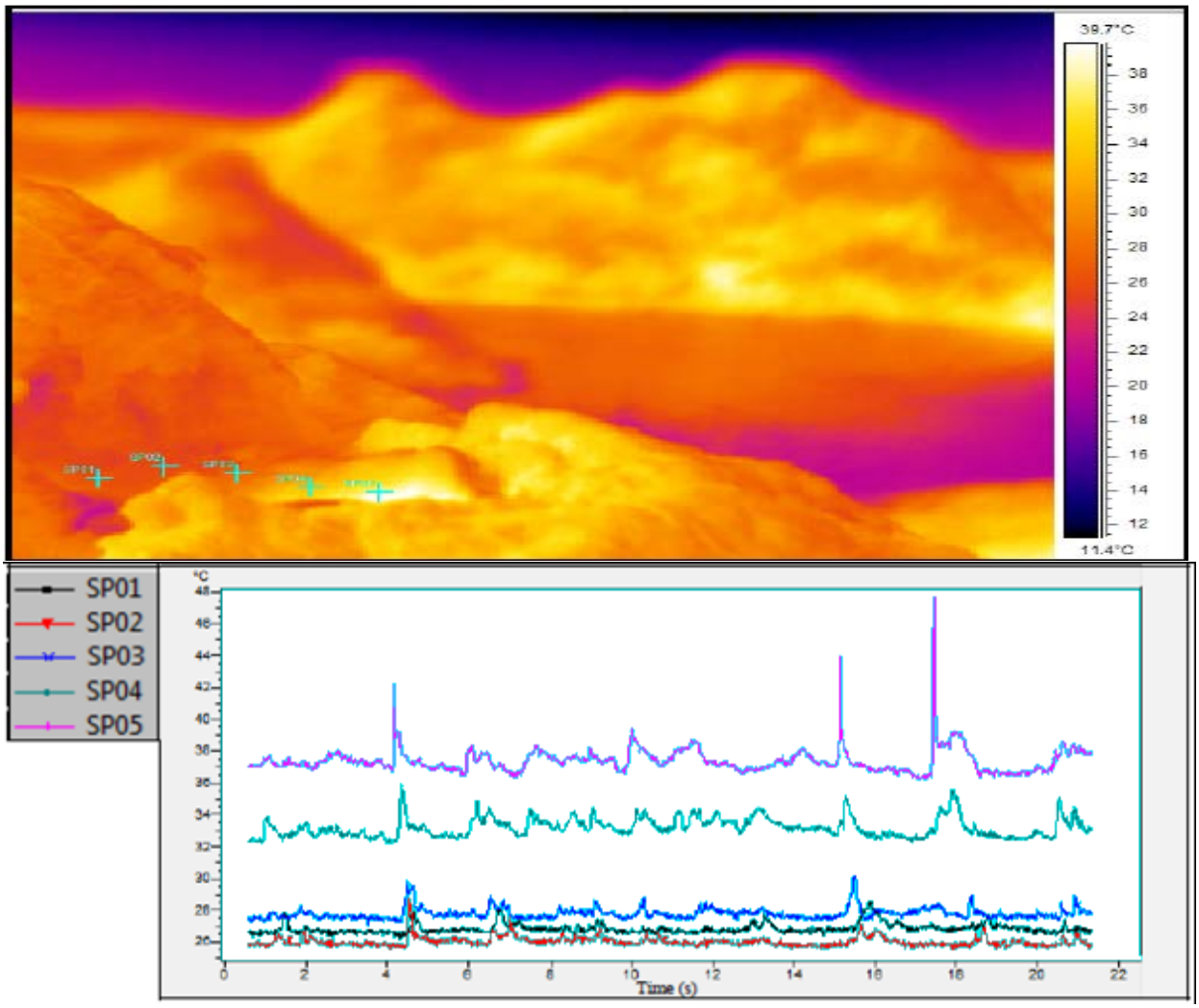

Figure 3-10: FLIR thermal image obtained March 13, 2010. Thermal readings of five points above an actively degassing vent in the Davis-Schrimpf geothermal field (top) were graphed over 30 seconds (bottom). The quick spikes in temperature found in the graph correspond with periods of gas bubbles venting from the gryphon.

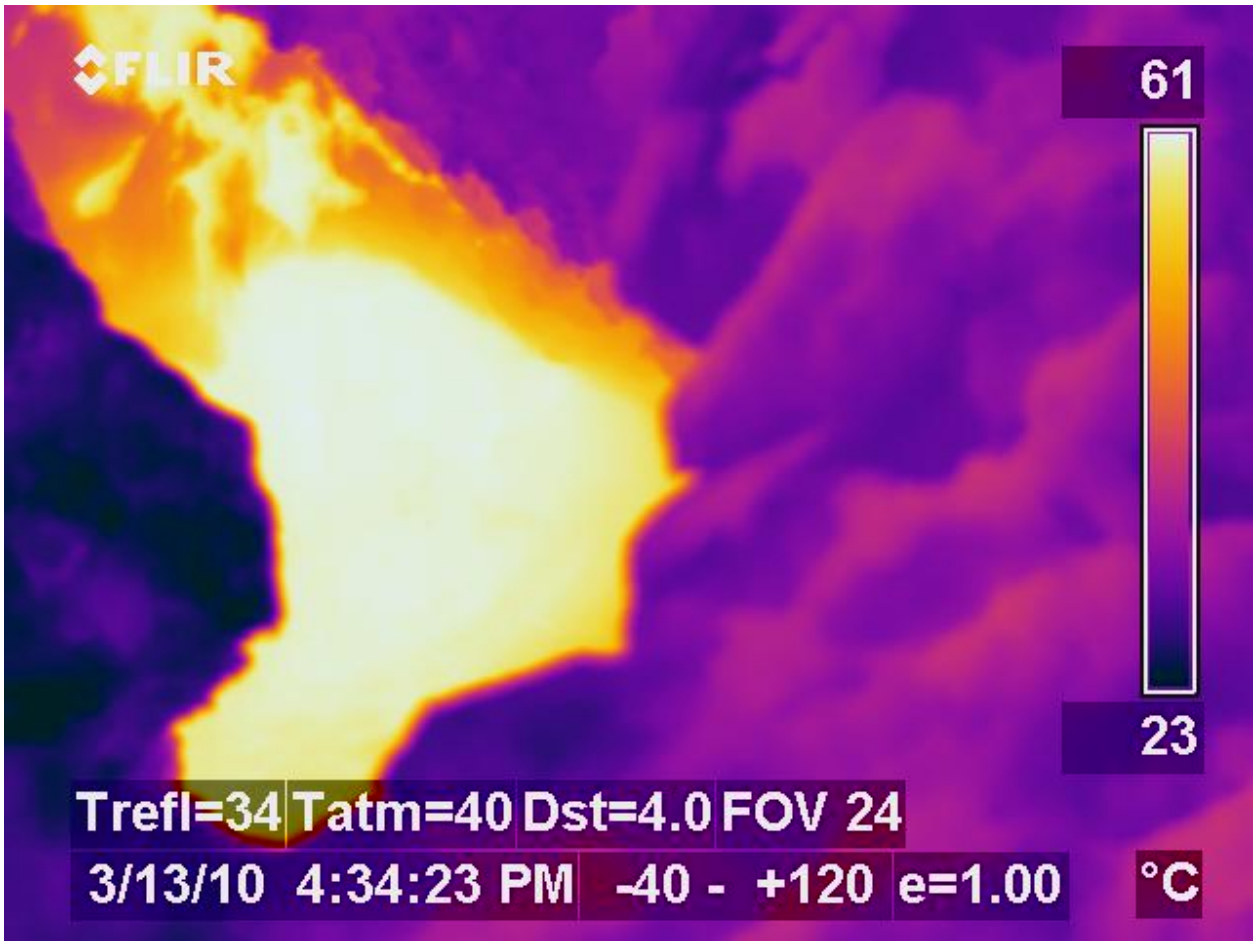

Figure 3-11: FLIR thermal image of the vent in region 3 that had a heat flux analysis performed upon it. Note that the hottest areas of the vent are in the central areas where gas is bubbling out of the liquefied mud.

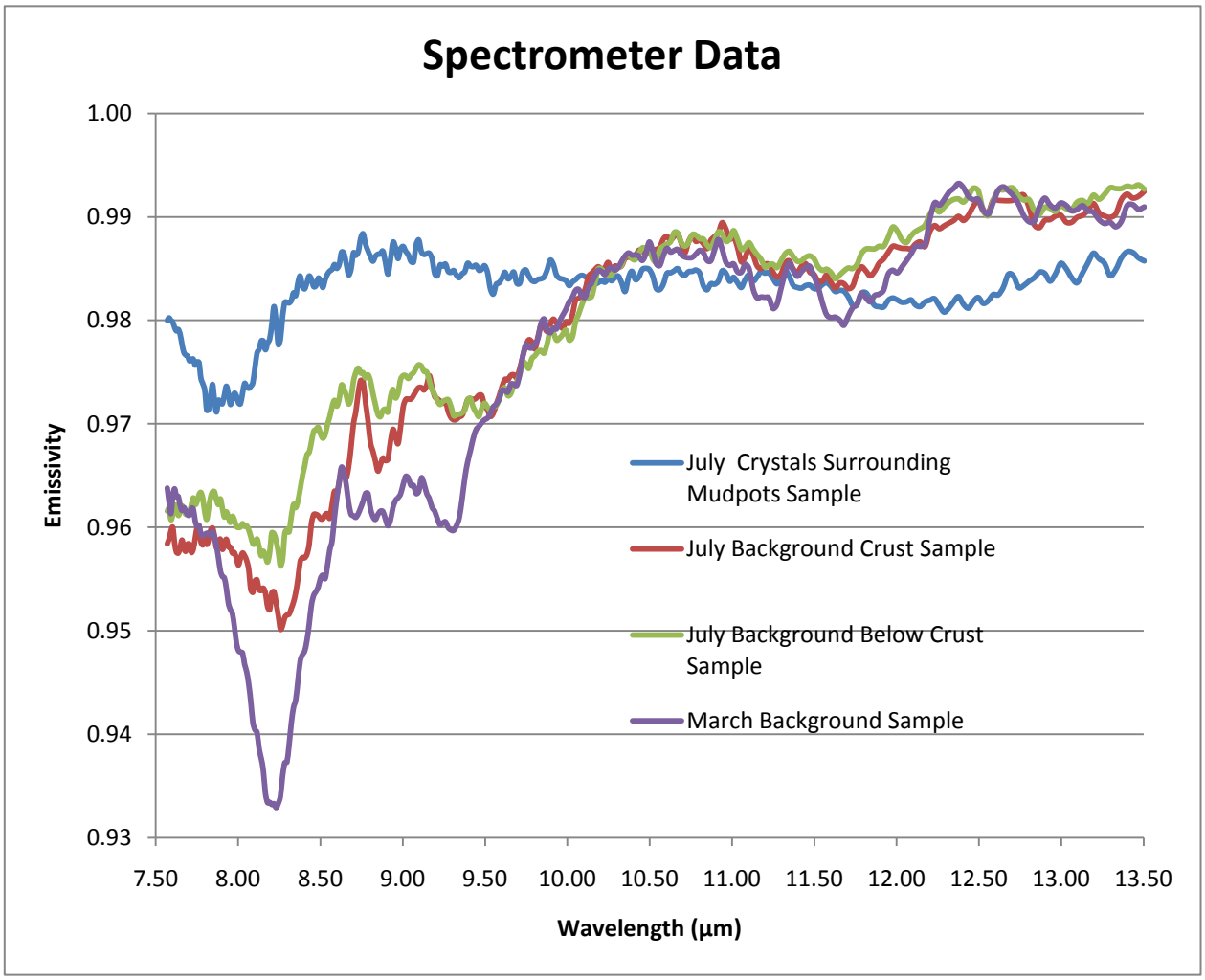

Graph 3-5 : Spectra from four samples collected from the Davis-Schrimpf geothermal field from the July and March expeditions. These data were acquired by the Nicolet Nexus 670 FTIR spectrometer. Notice the absorption feature similar to the unidentified mineral feature in the March Background Sample.

The March Background sample, which had a confirmed presence of the unidentified mineral, was then taken to the Material Micro-Characterization Laboratory (MMCL) in the University of Pittsburgh Swanson School of Engineering for further analysis. Both SEM and XRD tests were performed on this sample. During the SEM analysis, five grains were targeted for element analysis (**Appendix A).** SEM analysis revealed that elements of carbon, oxygen, iron, sodium, magnesium, aluminum, silicon, chloride, potassium, calcium, titanium, and sulfur were all present in the March 2009 sample. The combinations of elements found in each grain can be found in **Appendix A**. Of the grains analyzed one grain of note had a unique elemental make up of carbon, oxygen, iron, sodium, magnesium, aluminum, silicon, sulfur, chloride, potassium, titanium and calcium. Many of the elements found in this make-up are similar to those found in a salt/evaporite grain. An XRD analysis was then performed upon the March Background Sample (**Figure 3-12**). By constraining the potential minerals found in the XRD libraries to only those that have elements found in the SEM analysis, the minerals quartz (SiO_2), calcite ($CaCO_3$), halite (NaCl), dolomite ($CaMg(CO_3)_2$), rutile (TiO_2), and microcline ($KAlSi_3O_8$) were identified within the sample. However, with just these minerals, the presence of both sulfur and iron in the sample were not accounted for. All these minerals have known spectra that do not contain the low TIR wavelength absorption feature associated with the unidentified mineral.

Spectral analysis of potential minerals continued due to the inability to identify the mineral with SEM and XRD. Based on elements present in the SEM analysis this mineral may be a sulfate salt, therefore potential minerals in this category were analyzed in the FTIR spectrometer producing the results found in **Appendix B.** However, no matching minerals were found.

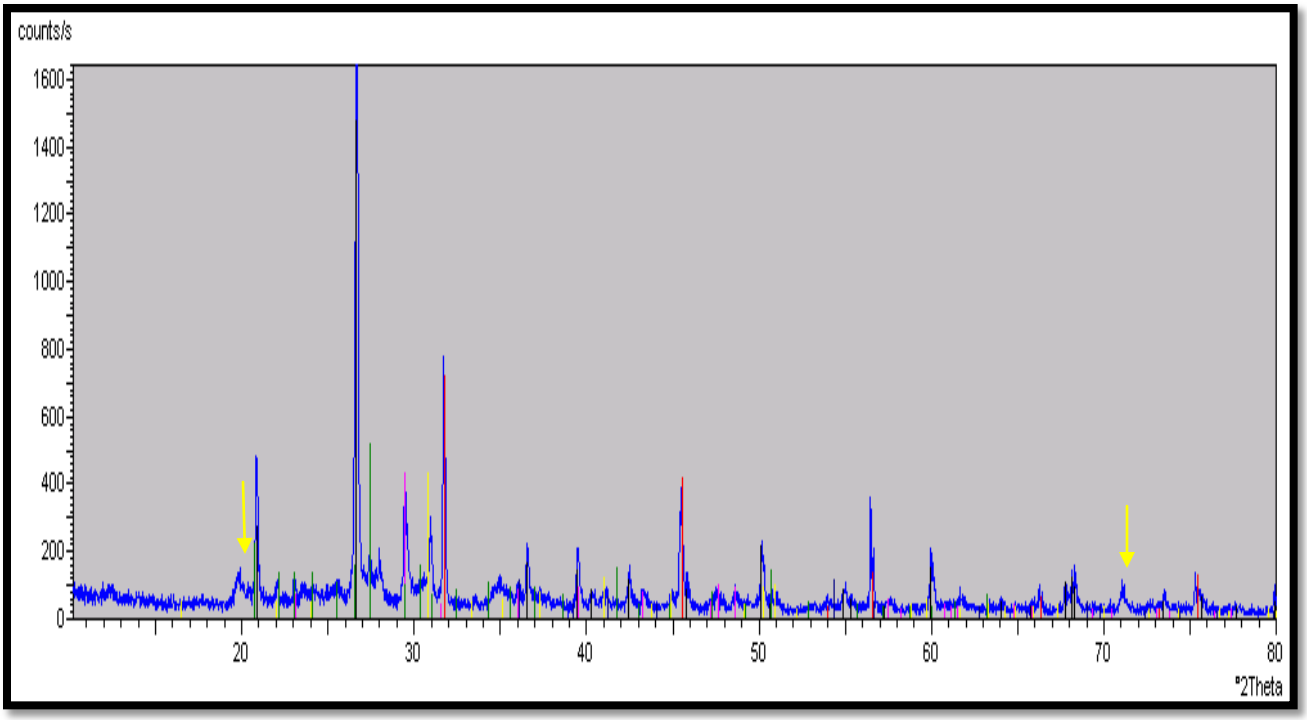

Figure 3-12: XRD analysis graph of the March background sample. Minerals are matched to peaks in counts at different °2θ values. Colored lines on the graph correspond with readings associated with a certain type of mineral. Black lines are associated with quartz, pink with calcite, red with halite, yellow with dolomite, dark blue with rutile, and dark green with microcline. Note that no minerals were found to be associated with the spikes at approximately 20 and 73 °2θ.

4.0 DISCUSSION

The new availability of the 128 channel spectral resolution and 1 m^2 spatial resolution SEBASS sensor has led to several new discoveries in the Salton Sea geothermal field, as has the use of more common instruments and methods. Thermal readings collected in the field as well as those collected by ASTER over a 7 year period were used to better evaluate the heat carriers in the Davis-Schrimpf geothermal field as well as changes in the degree of geothermal activity over the past seven years. Analyzing the Salton Sea with SEBASS allowed specific minerals dominantly surrounding geothermal fields to be identified. In the process of identifying minerals surrounding geothermal fields an unknown mineral was discovered and analyzed.

By regressing SEBASS data to the resolution of the MAGI and ASTER sensors, the degree of TIR spectral resolution needed to identify surface minerals can be analyzed. Correctly determining this degree of spectral resolution would allow TIR sensors to be produced with a high degree of spectral accuracy that, by having fewer channels, are still be more cost effective than TIR hyperspectral sensors.

4.1 THERMAL ANOMOLIES

Thermal readings taken from the field and obtained remotely were used to build upon the current understanding of temperature variations within the Davis-Schrimpf geothermal field and to validate past research. The ASTER sensor has a 7 year record of the temperature of the Davis-Schrimpf geothermal field. The 90 m pixels of the data cause most of the geothermal field to be located within one pixel. By comparing the temperature of this pixel to that of the surrounding background surface and the water inside the Salton Sea a temperature elevation of 1-6°C for the geothermal area is observed over this period. In a geothermal system where mud and gas have been identified as heat carriers (Svensen et al., 2009), variations in surface heat are a direct result of changes in the ability of these two driving forces to reach the surface. In both of these cases deep gases produced from devolatilization reactions with sedimentary carbonates are expected to be the main driver for the seep activity (Svensen et al., 2007). Thus, as more or less heat comes into contact with sedimentary carbonate minerals, variations in heat reaching the surface occur. This can occur either from the deep magma reservoir drawing closer or further from the surface, or from the process of deep heated mud being transported to the surface and new minerals being forced deeper, thus allowing previously unvolatilized sedimentary carbonate to begin degassing. The ASTER seven year thermal profile acts as a record of these changes occurring in the geothermal system, spikes in the ASTER thermal profile are related to increases in geothermal activity. Comparing the spikes in the ASTER data to seismic data of the area demonstrates that the first spike occurs several months after a Salton Sea earthquake swarm that occurred in late August 2005 (Lohman et al, 2005) and the second spike occurs several months after another swarm in the same area that that took place in late March 2009 (Anza Group, 2010). These

earthquake swarms could have triggered both the pulses in the magma reservoir and subsidence of carbonate sediments.

Through the use of a thermocouple and the FLIR thermal camera, readings of mud pots were found to be 10-15°C cooler than the surrounding area in the field. This result was echoed in the SEBASS data where mudpots are found to be 9-12°C cooler. This accuracy was made possible by the high spatial resolution found in both SEBASS and the proposed MAGI sensor. The entire pixel is filled with the low temperature mudpot feature, no temperature mixing occurs, and this results in an accurate temperature for the small feature. Pixels where hot gryphon vents can be found had a much lower degree of accuracy. In the field gryphons were found to be 19-41°C warmer than the surrounding surface, pixels containing these features were only 10-13°C warmer than surrounding pixels. This occurred because the gryphon vents were smaller than 1 m^2 and therefore where observed in a pixel, temperature mixing from multiple surfaces occurred. These pixels still appeared hotter than surrounding pixels therefore confirming heat production in a feature, accurate results from these features are limited. Interpretation of this remote data can be better understood by collecting temperatures of features in the field. Being able to remotely record the temperatures of individual features allows insight into the properties of the geothermal field without needing to travel to the location.

Remote thermal readings of hot gryphon vents and cool mudpots coincide with the past findings in Svensen et al., 2009 and support the theory that heat in the geothermal field is not carried by water and therefore gases and/or mud is the main carrier of heat. Thermal readings were also recorded from the FLIR thermal camera in the form of several 30 second long videos of an actively degassing vent. These thermal videos reveal temperature spikes at an average of 10°C that reach a high of 48°C occurring where gases bubbles out of the liquefied mud. The

temperatures of the mud found within gryphon vents were as high as 61°C, the hottest areas of the vents were the bubbling center regions where degassing occurred. There are several reasons for such thermal readings. First, where volcanic gases bubble out of the vent, hotter subsurface mud was brought to the surface. Thermocouple readings were taken of the liquefied mud slightly below the surface and away from the bubbling center to reveal temperatures as high as 57.5°C in several vents. Whereas this was 3.5°C cooler than surface temperatures measured in the bubbling vent center, it was still 7.5 to 17°C warmer than surrounding surface mud. A second reason why the bubbling centers of gryphon vents were hotter was due to heating occurring from deep gases. The 10°C spike in heat flux several inches above the vent demonstrates that the gases are indeed carrying heat from the magmatic source. The bubbling center of the gryphon vent has direct contact with these gases and therefore is heated to a higher temperature then the surrounding mud. Whereas both sources are clearly heat carriers, the main heat carrier is the liquefied mud. By finding that the liquefied mud in the degassing center of the vents is only raised several degrees confirms the prediction in Svensen et al., 2009 that gases may reach a higher temperature then the mud, but they simply lack the mass to raise temperature a significant amount. Furthermore, the building of gryphon mounds around these vents is evidence that large quantities of mud are being mobilized from below the surface. Also, in the case of the mud pots, a lack of liquefied mud is visible upon inspection. These mudpots still have large quantities of gas flowing through them. However, without the main heat carrier they resemble temperatures close to those of the groundwater in the area, which was cooler than temperatures found on the ground surface.

4.2 MINERAL MAPPING

An opportunity was presented to analyze the surface mineralogy of the known geothermal fields in the Salton Sea with remote sensing data of increased accuracy by utilizing the thermal deconvolution function on the high resolution SEBASS remote data. Upon an initial inspection of these mineral maps and correlating RMS maps two important features stand out. The first was that anhydrite was found only surrounding the geothermally active areas and gypsum could be found abundantly throughout the Salton Sea Trough, but not surrounding these same geothermal areas. Second, the area being classified as kaolinite was compared to the RMS map and a very strong correlation was noted. This kaolinite mineral, much like the anhydrite, could only be found surrounding geothermally active areas.

The Salton Sea has a history of evaporite deposits and mining (Helgeson, 1968) of minerals such as gypsum. In 1984, anhydrite was encountered in the SSDP borehole. This anhydrite was found in nodular textures, similar to those found in gypsum, therefore suggesting that anhydrite had replaced gypsum (Herzig et al., 1988). In the presence of pure water, at the typical surface pressure of 1 atm, gypsum is the stable phase for calcium sulfate for temperatures below 40°C, anhydrite is the stable phase for higher temperatures (MacDonald, 1953). Both the 7 year ASTER thermal profile and field measurement taken March 13 and July 2, 2010 found surface temperatures reaching a maximum of 38°C. Although these temperatures were not hot enough for anhydrite to form on the surface, the proximity of these temperatures to the equilibrium changing temperature of 40°C provided proof that the anhydrite may have been formed on the surface. It has also been found that where gypsum is hydrothermally heated a sharp transition from fast growth to very fast dissolution occurs at approximately 120°C; at this point there occurs a sudden nucleation of a phase more stable then gypsum, anhydrite (Jordan

and Astilleros, 2006). The Salton Sea geothermal system has been found to produce brines in excess of 350°C at a depth of 1400m (Elder and Sass, 1988), therefore proving that the transition of gypsum to anhydrite could have occurred post-burial. The intrasediment growth of anhydrite nodules is a common feature of burial alteration of gypsum to anhydrite (Spencer, 2000) as well as sabhka-style syndepositional surface alteration. Therefore, without other evidence, the sub-surface anhydrite could have been formed both on the surface or sub-surface. The geothermal brines and liquefied mud of the system absorbed a degree of this anhydrite and transported it to the surface. Here the anhydrite mixed with meteoric groundwater and leached out to the surface. Current climate conditions in the Salton Sea prefer the conversion of anhydrite into gypsum on the surface, therefore any anhydrite found on the surface has been recently deposited. Due to the intense temperatures needed to create sub-surface anhydrite as well as the transport process needed to get it to the surface, anhydrite is only found in geothermally active areas of the Salton Sea. In some cases remnants of anhydrite were found in areas that could have potentially been active in recent history or are starting to develop enough geothermal heat to create anhydrite (**Figure 4-1**).

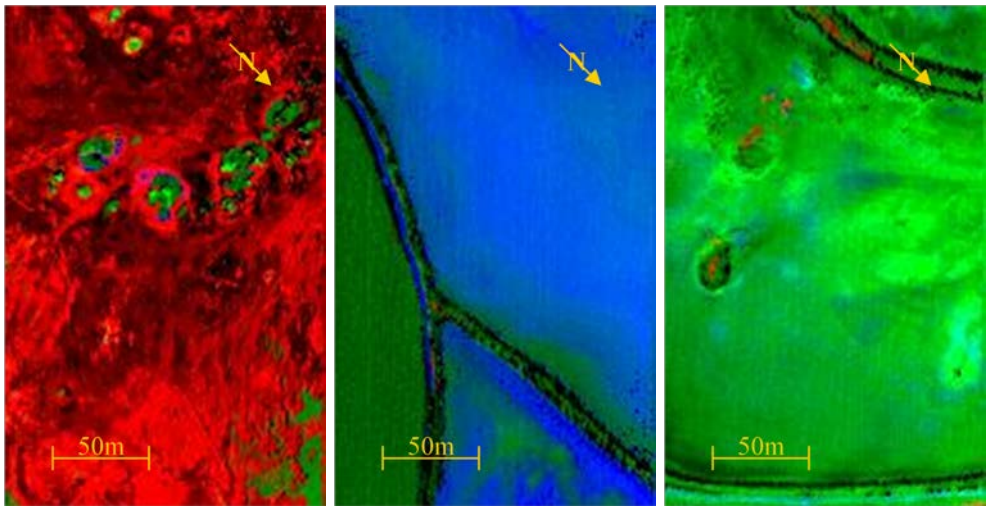

Figure 4-1: Three scenes from the Salton Sea taken from the same overpass. In March 26, 2009 the previously analyzed scene from the Davis-Schrimpf Geothermal field was recorded. Image deconvolution has been performed on the entire overpass the end-members of R: anhydrite, B: gypsum, and G: quartz are highlighted here. As seen in previous figures the geothermal field (left) has a larger amount of anhydrite. In a typical agricultural field (center) large amounts of gypsum can be identified on the surface. To the northeast of the geothermal field (center) geothermal relics can be identified by sparse amounts of anhydrite on the surface.

Similarly, the mineral that had been identified as kaolinite could only be found surrounding geothermally active areas. As mentioned earlier this mineral area corresponded to the areas of high error in the RMS map. Examined more closely the spectra of the area differs largely from the spectrum of pure kaolinite. This is due to a significant absorption feature found in the spectra at 8.2 µm. An absorption feature at wavelengths this short in the TIR spectrum could not be matched to any mineral currently found in a spectral library. Due to this same feature, this mineral stands out compared to other minerals in the geothermal field. Therefore this mineral can be easily recognized in the emissivity spectra of pixels.

Both anhydrite and this unidentified mineral can be used as indicator minerals for geothermal activity in the Salton Sea. This is due to the proximity to geothermal activity both of these minerals exhibit as well as the reliance upon geothermal activity anhydrite and, seemingly

the undefined mineral as well, have to form and reach the surface. Identifying the indicator minerals specific to each differing geothermal area could lead to unknown geothermal areas being remotely located in any potentially active area.

Comparing the 2009 and 2010 dataset some discrepancies appeared. Most of these were small, such as slight differences in percentages or regions of minerals. However, a major difference was observed in the "kaolinite" area. In the 2010 scene of the Davis-Schrimpf geothermal field this area is roughly twice as large as it is in the 2009 data, or 9613 m^2 with values above zero in 2009 compared to 17345 m^2 in 2010. Researching potential differences in the environment between where the two datasets were collected revealed that before the March 26, 2009 data had been recorded, there had been 0 mm of rainfall in March and only 2.5 to 6.4 mm of rain in February. There had not been any rain for 36 days before these data were recorded (National Weather Service, 2011). In the case of the April 6, 2010 data the there had been 0.25 to 2.55 mm of rainfall in April and 12.7 to 25.4 mm of rainfall in March. In fact, at the date these data were collected, the last rainfall in the area occurred just six days earlier (National Weather Service, 2011). This increase in rainfall before the 2010 data collection would have allowed the subsurface minerals to leach out to the surface by dissolving into water that was raised to the surface by these rains. Once the large amount of water on the surface evaporates, deposits of this unknown mineral were left. This accounts for the increase of the unknown mineral and even the slight increase of anhydrite found on the surface.

4.3 UNKNOWN MINERAL

By indentifying the unknown mineral found in the Salton Sea geothermal field an important step would be made toward indentifying an indicator mineral that can be utilized in this geothermal field and potentially other fields as well. Many steps were taken to better understand and identify this mineral.

Initially, as mentioned earlier, this mineral was found by the unique 8.2 μm absorption feature in its spectrum. This absorption feature was confirmed to be more than just an artifact of the sensor because the March background surface sample was analyzed in the FTIR spectrometer and the same absorption feature was identified. This also verified that the unidentified mineral could be found as part of the sample collected March 13, 2010. In a sample that was collected from the same basic area in July this feature was not found. Further tests were then performed to isolate and identify the mineral in this sample. SEM was performed on 5 grains of the sample and a full elemental analysis of each of these grains was collected. An XRD analysis was then performed on the sample that provided inconclusive results, finding only minerals that already have well documented spectra that do not have absorption features at 8.2 μm. However, during this XRD analysis two peaks at approximately 20 and 73 °2θ as well as the elements sulfur and iron found in SEM analysis remained unaccounted for. Of the grains analyzed only one contained the elements sulfur and iron; it also contained carbon, oxygen, sodium, magnesium, aluminum, silicon, chloride, potassium, calcium, and titanium. These elements resemble those found in sulfate salts. Examining the spectra of sulfate salts the same strong lower TIR wavelength absorption features are observed. The unknown mineral was also found to be water soluble enough to leach out of the subsurface during heavy rains and become crystalline within six dry days, as was observed in the 2009 and 2010 maps. It was also found to be friable enough

to erode away rather quickly, causing the reduced amounts on the surface where the 2009 dataset was collected and leading to the mineral not being identified in the July 2, 2010 background sample.

All these features, considered together lead to a good possibility that the unidentified mineral is a type of sulfate salt. This led to the consideration that the mineral might be szomolnokite ($FeSO_4 \cdot H_2O$), which is the type of iron sulfate that would form in the conditions present at the Salton Sea. However, this sulfate had already been spectrally analyzed and its absorption feature occurs at approximately 8.7 μm. Epsomite (MgSO4•7H2O) and its less hydrated form kieserite (MgSO4•H2O), which both have the possibility to form on the surface of the Salton Sea, where then analyzed by the FTIR spectrometer in the IVIS lab. However, the absorption features for both of these minerals do not occur at a short enough wavelengths (8.5 and 9.0μm). A mineral with a still shorter wavelength absorption feature was needed, thus a sulfate salt with a lower atomic weight was considered, thenardite (Na_2SO_4). Once again the spectrum of thenardite was analyzed in the IVIS lab spectrometer only to find that its absorption feature occurred from 8.6 to 8.8 μm. To date the mystery of the chemical formula of the unidentified mineral remains unknown. There was a possibility that the mineral may be beryllium sulfate ($BeSO_4$) due to the chemical combination being one of the few potential sulfate salts with an atomic weight lower then sodium sulfate. However, beryllium was not discovered in the SEM analysis and was not discovered historically in this area during an elemental analysis that was performed on the brines in the area (Helgeson, 1968). Another dissuading factor was that beryllium sulfate has never been found to occur in nature and where created in the lab it is regarded as a toxic substance that irritates the eyes, skin, and lungs according to its international chemical safety card. Such a substance would not go unnoticed by the tourists and Department of

Environmental Protection personnel that frequent this area. The unknown mineral could also be a rare sulfate that formed as a result of higher temperature in the geothermal brines (langbienite ($K_2Mg_2(SO_4)_3$, löweite ($Na_{12}Mg_7(SO_4)_{13}•15H_2O$) and vanthoffite ($Na_6Mg(SO_4)_4$)) or from a back reaction of gypsum and anhydrite with evolved brines (syngenite ($K_2SO_4•CaSO_4•H_2O$) , polyhalite ($2(CaSO_4)•K_2SO_4•MgSO_4•2H_2O$), and glauberite ($NaSO_4•CaSO_4$)) (Spencer, 2000). There is also a potential for this unknown mineral to have some combination of the historical elements found in brines that are published in Helgeson, 1968 that, in addition to elements discovered by the SEM analysis include strontium, boron, lithium, barium, lead, zinc, and copper. Future tests are required in order to decipher the true identity of this unknown mineral.

4.4 SPECTRAL RESOLUTION COMPARISONS

By comparing the spectral resolution of the SEBASS, MAGI and ASTER sensors the real question that must be answered is: How high must the spectral resolution of a sensor be in order to properly analyze an area? The SEBASS sensor, with a resolution of 128 channels, clearly identified regions of differentiating surface mineralogy. The unknown mineral formed a distinct ring around the active geothermal vents in the Davis-Schrimpf geothermal field, causing it to be quickly identified as a geothermal activity indicator mineral. Anhydrite and gypsum, two spectrally and chemically similar minerals, with single absorption features at 8.35 to 8.65 µm in anhydrite and 8.75 µm in gypsum, were also differentiated in SEBASS. This important differentiation allowed for yet another geothermal indicator mineral to be identified, as anhydrite could only found in geothermally active areas from the alteration and hydrothermal transport of

gypsum. The higher spectral resolution also caused unmixing percentages to be more accurate, allowing for aspects of minerals with smaller percentages on the surface to register in the image deconvolution process and be accounted for in the final end-member mineral maps.

The MAGI sensor, despite have only a 32 channel spectral resolution compared to the 128 of SEBASS, performed similarly. The unidentified mineral was still found to be an anomaly forming a ring around active geothermal vents. Although the area of this mineral was slightly larger in both the 2009 and 2010 datasets (**Figure 3-11 and 13**), no pixels that were classified in the SEBASS data as containing this mineral were excluded in the MAGI data, thus proving that the MAGI sensor can successfully identify this unknown mineral. Anhydrite and gypsum were also successfully differentiated at this lower spectral resolution, despite having closely related spectra. Yet another indicator mineral of geothermally activity could be positively identified and located with the MAGI sensor. Comparing the unmixing mineral percentage of SEBASS and eMAGI there were percentage differences that ranged from 0 to 16% with the majority of the difference occurring below 2.5%. Although there was a 16% difference for the “kaolinite” mineral the percent of surface minerals in the classification were still significant enough to identify the unknown mineral area. The MAGI sensor could successfully identify both geothermal indicator minerals and allow image deconvolution to unmix surface mineralogy to an accurate degree.

The 5 channel TIR spectral resolution of the ASTER sensor presented immediate shortcomings. Most notably was the fact that without at least nine channels the full mineral suite of eight minerals cannot be unmixed. This limitation of 5 channels only allows four minerals to be unmixed at a time. To deal with this limitation four different minerals in the suite were

unmixed three times. Although a direct comparison was impossible without the exact same unmixing function occurring, this alternative still proved useful.

Much like the tests previously performed in Cuprite, NV, (Hall et al., 2008) regression to the ASTER spectral resolution resulted in a complete loss of fidelity. The area occupied by the pseudo-kaolinite at higher resolutions was completely missing. Whereas there did appear to be an area of slightly higher RMS values surrounding the geothermal vents, similar high RMS value could be found throughout the dataset. With no more than this evidence to go on, this indicator mineral could be easily missed. Anhydrite was successfully identified surrounding the geothermal field, however it was also identified in many other areas throughout the Salton Sea that are agricultural fields previously classified as gypsum. With this regression of spectral resolution, the differentiation between gypsum and anhydrite is lost; therefore anhydrite can no longer be used as an indicator mineral. By analyzing the difference between mineral percentages in the unmixing process differences ranging from 0 to 88% with a majority of these occurring above 10% were observed. Whereas percentages differences can be expected due to less end-members being factored into the process, differences reaching as high as 88% are too significant to occur as a result. This difference occurs due to unmixing at this resolution causing classification of areas to be dominated by a single mineral, therefore causing important minerals that occur at lower percentages to be completely missed.

The MAGI sensor will overcome the problems occurring at the spectral resolution of the ASTER sensor to the point where it can produce virtually indistinguishable visual results to those of the SEBASS sensor and still use 96 less channels. The efficiency of this lower resolution sensor provides strong evidence that an orbital version of the sensor would identify these minerals and reduce costs due to the compact design and limited usefulness of an additional 96 extra channels.

5.0 CONCLUSIONS

Analyzing the collected thermal data revealed some interesting results, the seven years of data collected by the ASTER sensor can be used to measure the heat flux that occurs in the geothermal field, which is driving force of geothermal activity. Readings collected on the surface and subsurface of the gryphon vents revealed that liquefied mud is the main heat carrier in this system. This was due to its near constant elevated temperatures throughout the subsurface of the vent opening. Thermal readings collected both remotely and in the field shed some light into understanding the dynamics of the Salton Sea geothermal system.

To date the mineral with an 8.2 μm wavelength absorption feature remains unidentified. This mineral was observed to be water soluble enough to leach out of the soil during rains, to crystallize on the surface in a matter of days, and be friable enough to disperse in months. These properties suggest the presence of an evaporite. The low TIR wavelength absorption feature found in the spectrum of this mineral match those found in sulfate salts. Although, no sulfate salt with an absorption feature low enough to match this mineral could be found during analysis, there remains several possible methods to be explored to identify this mineral. Several obscure sulfate salts still remain to be analyzed. There is also the possibility that heated fluids from the geothermal activity and acidic water conditions caused by the influx of CO_2 from the deep gases has changed the molecular formula of a typical sulfate salt to produce a shorter wavelength

absorption feature. Right now, the unidentified mineral is a mystery, but with further testing and analysis the true identity of this mineral will be known.

The ability to find geothermal indicator minerals with the new availability of the high resolution SEBASS sensor was proven possible. Both anhydrite and the unidentified mineral could be used as indicator minerals in the Salton Sea due to the geothermal processes required to produce and transport these minerals to the surface. Upon investigation of several overpasses of the Salton Sea collected by the SEBASS sensor, these minerals were found to be located around geothermally active areas exclusively. There is a potential that using a linear deconvolution technique to search for these minerals in locations outside the Salton Sea will remotely locate geothermally active areas. Even with the possibility that these indicator minerals are unique to the Salton Sea, the process of analyzing these minerals can be repeated in other active geothermal zones to identify the unique indicator minerals for that area. By taking advantage of these indicator minerals a new step can be made in the exploration of geothermal activity. Active regions that are thermally undetected yet have the energy to alter the surface mineralogy to a degree can be found after a simple image deconvolution of remote sensing data. Therefore, allowing areas of high potential for geothermal activity to be indentified remotely before reaching them in person for a field analysis.

Comparing the SEBASS, MAGI and ASTER sensors, both SEBASS and MAGI succeeded in identifying important factors relating to mineralogy where the ASTER sensor failed. In general both the SEBASS and MAGI sensors produced the same results. Both sensors successfully located the unidentified mineral in the area surrounding the geothermal vents and could positively differentiate between the gypsum and anhydrite areas, allowing for two important geothermal indicator minerals to be identified remotely. Both of these minerals are

either unidentified or misclassified with the spectral resolution of the ASTER sensor. Readings of the many minerals found on the surface of the geothermal field can be accurately classified with the SEBASS and MAGI sensors, whereas the ASTER sensor tends to categorize most minerals found on the surface to a single mineral classification. Despite the 96 channel spectral resolution difference between the SEBASS and MAGI sensor, the 32 channel MAGI seems just as capable in most situations. This indicates that the MAGI-L sensor would be effective in these regards as well. The creation of this satellite sensor would allow a multispectral 32 channel TIR sensor to be placed in orbit and record locations throughout the world with the same spectral accuracy of many airborne hyperspectral TIR sensors.

Purely from the geothermal standpoint, the creation of the MAGI-L sensor will lead to detailed sweeps for geothermal indicator minerals and thermal anomalies to be performed in any location. Locations displaying features that are indicative of geothermally activity will be found quickly and effectively. Thus advancing geothermal exploration and allowing new geothermally active areas to be found. This would streamline the process of locating areas with the necessary energy for geothermal power therefore increasing the options for locations at where geothermal power plants could be built. Building these plants would help to increase geothermal energy input into the power grid and decrease reliance on more traditional means of energy.

APPENDIX A

SEM ELEMENT ANALYSIS

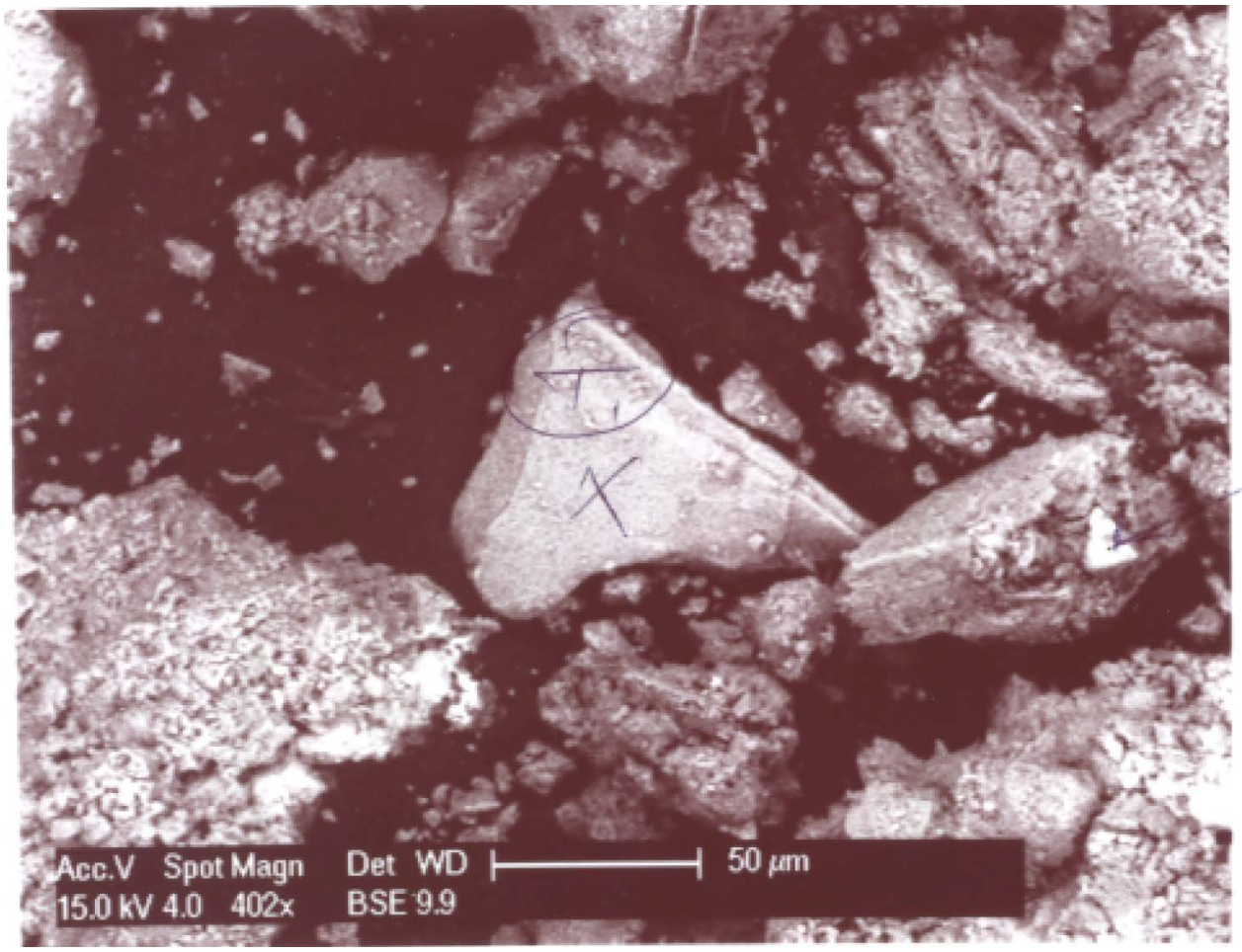

Image A-1: SEM image of a part of the March 13, 2010 Playa sample where the unidentified mineral was located.

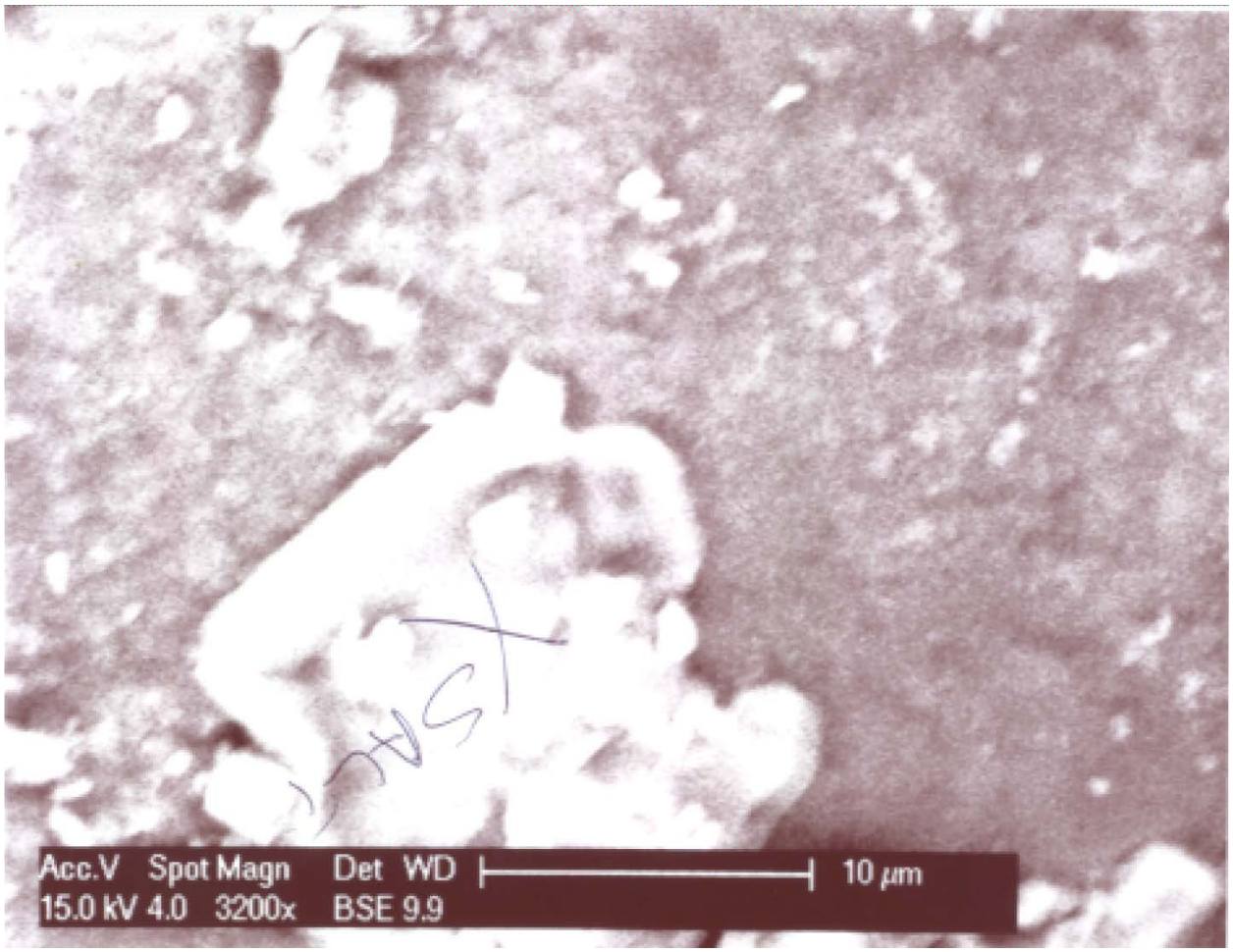

Image A-2: SEM image of the March 13, 2010 background surface sample. The large white grain in the middle of the image was identified as a salt sample that contained sulfur. This may well be a grain of the unidentified sample.

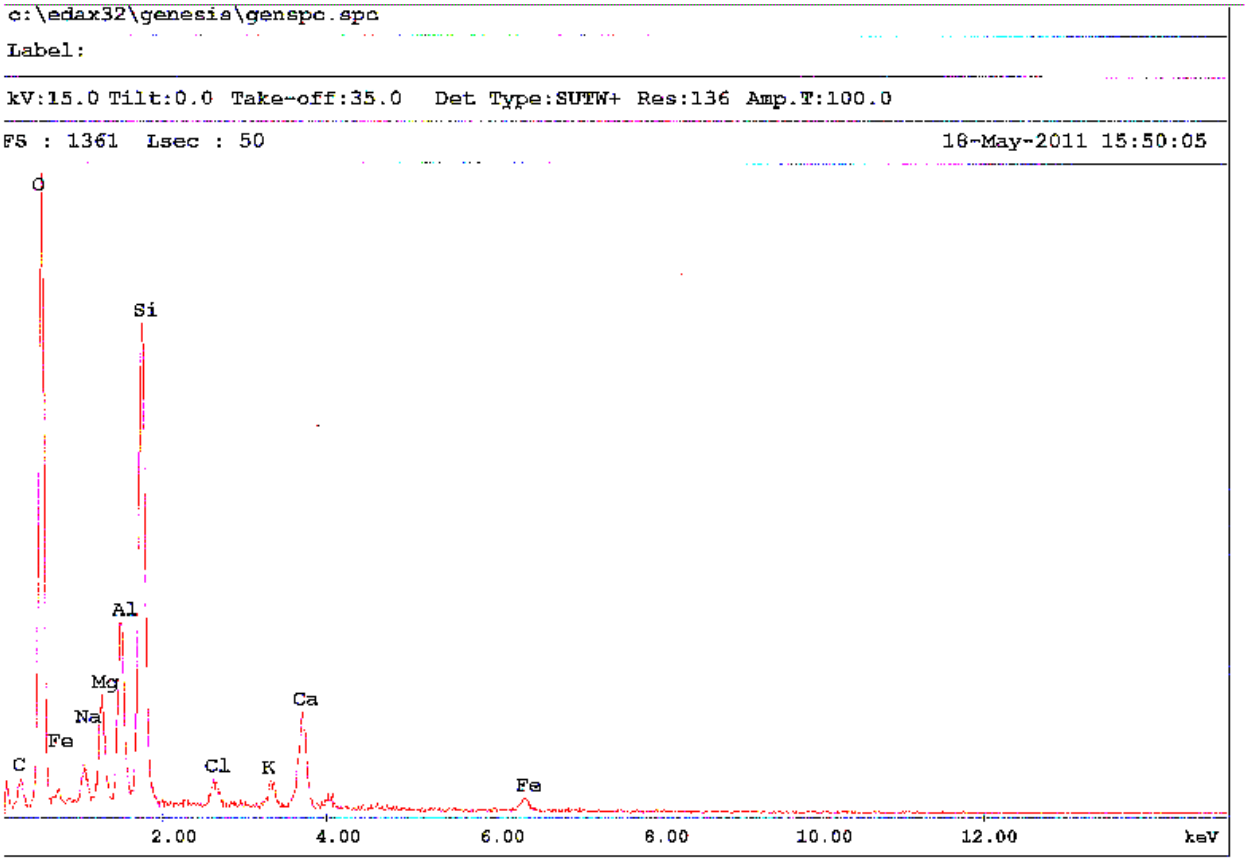

Graph A-1: End results of photon analysis of grains within March 2010 sample. Elements are determined based on where groupings of photons occur.

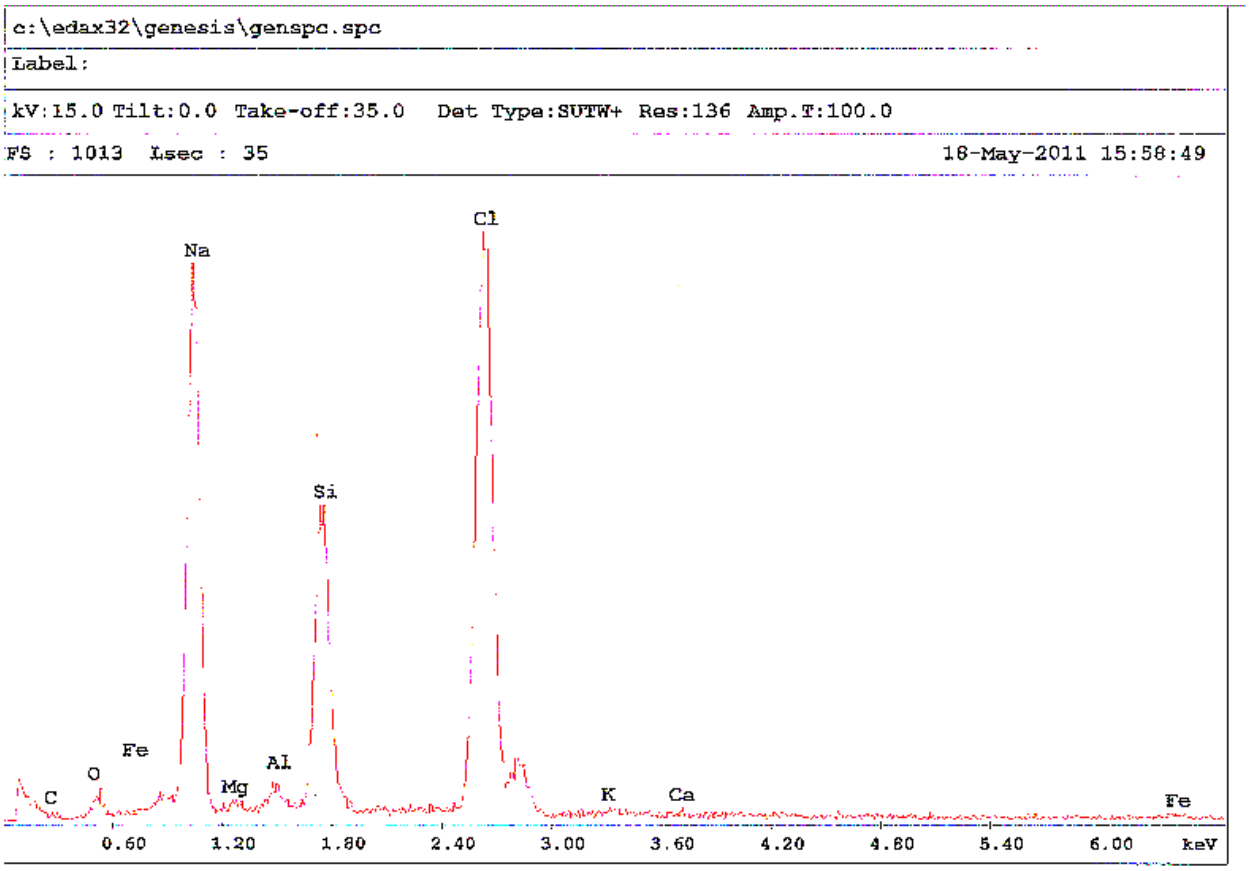

Graph A-2: End results of photon analysis of grains within March 2010 sample. Elements are determined based on where groupings of photons occur.

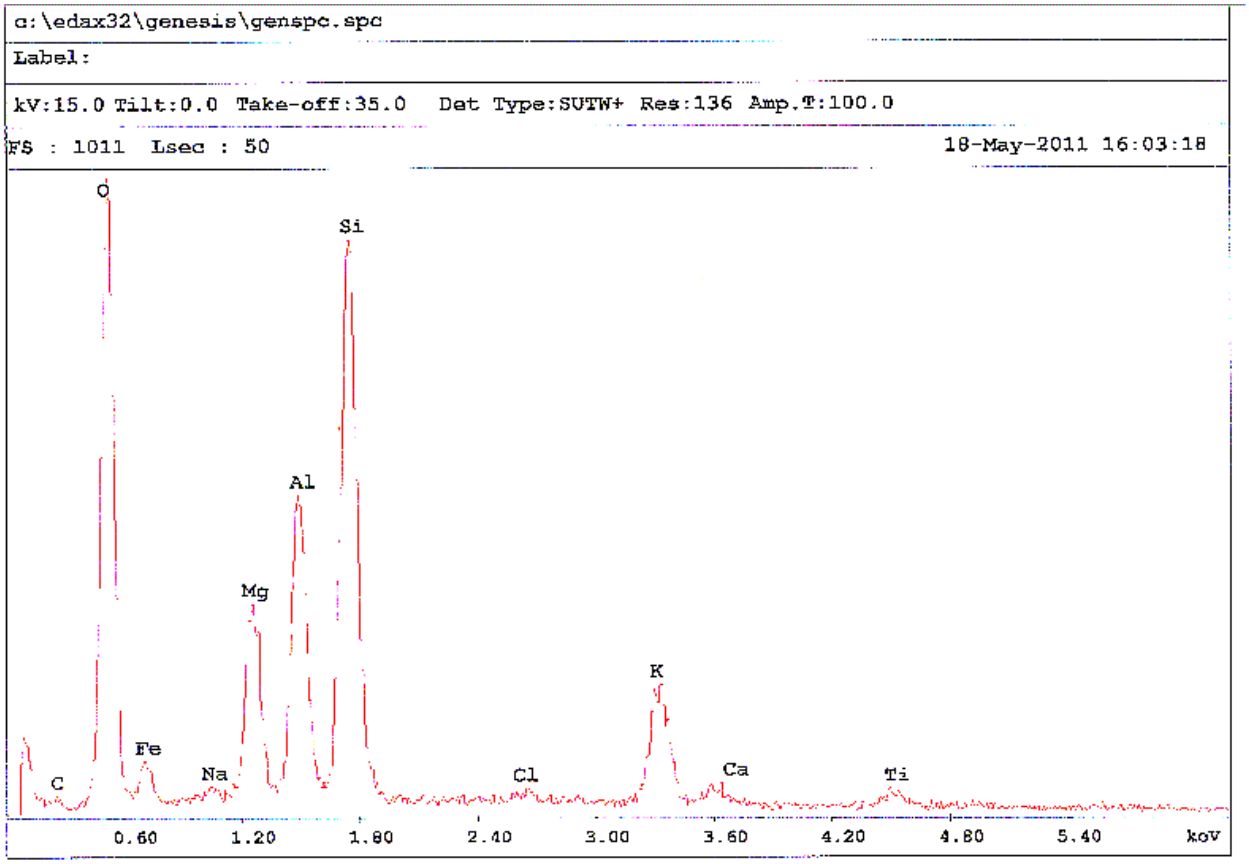

Graph A-3: End results of photon analysis of grains within March 2010 sample. Elements are determined based on where groupings of photons occur.

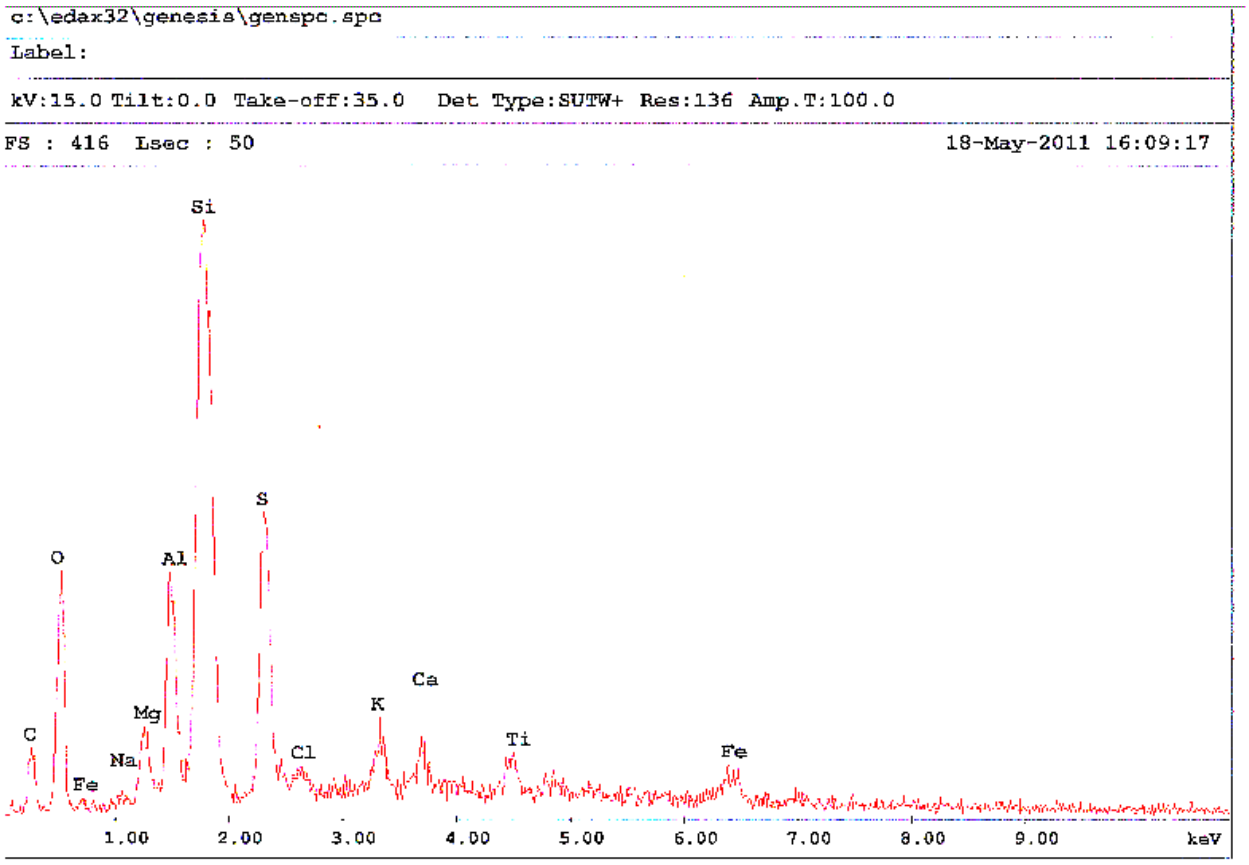

Graph A-4 : End results of photon analysis of grains within March 2010 sample. Elements are determined based on where groupings of photons occur.

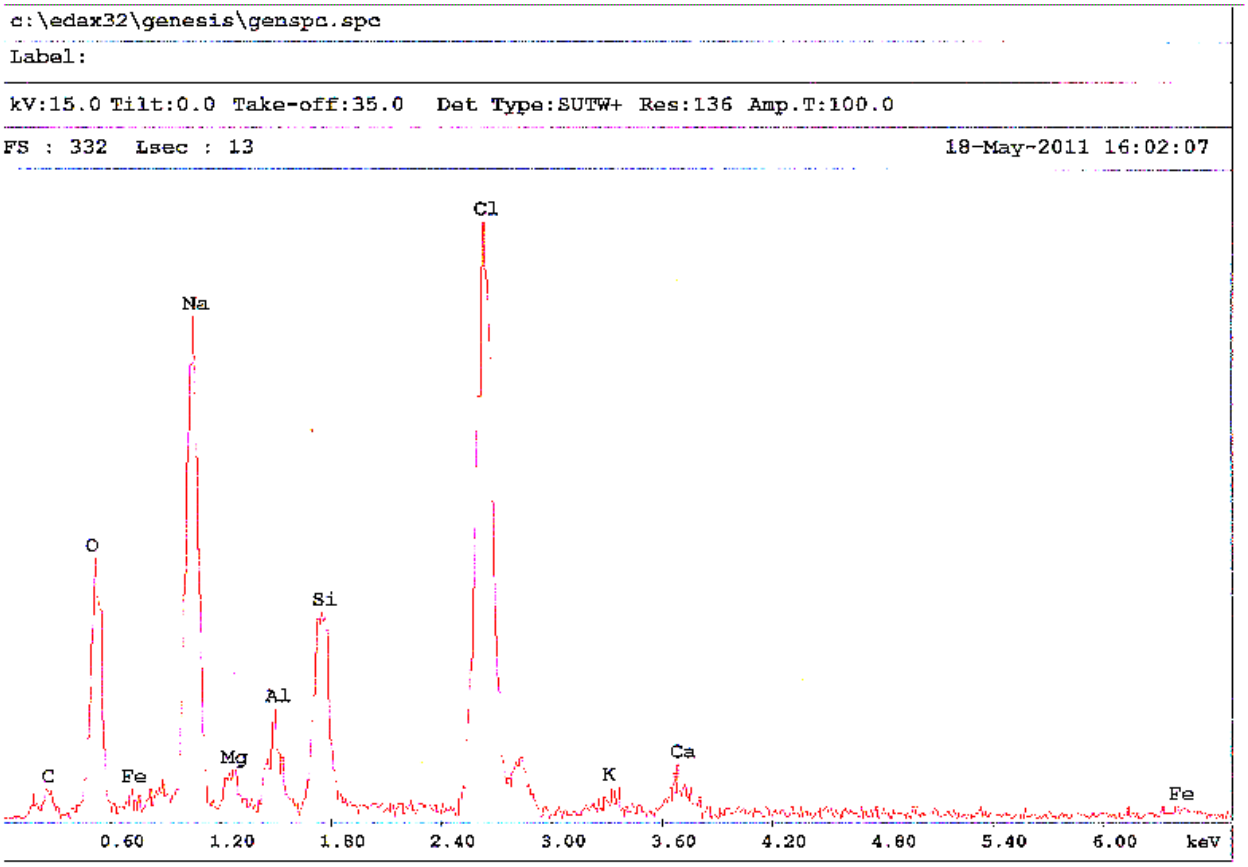

Graph A-5: End results of photon analysis of grains within March 2010 sample. Elements are determined based on where groupings of photons occur.

APPENDIX B

SULFATE SALTS SPECTRAL DATA

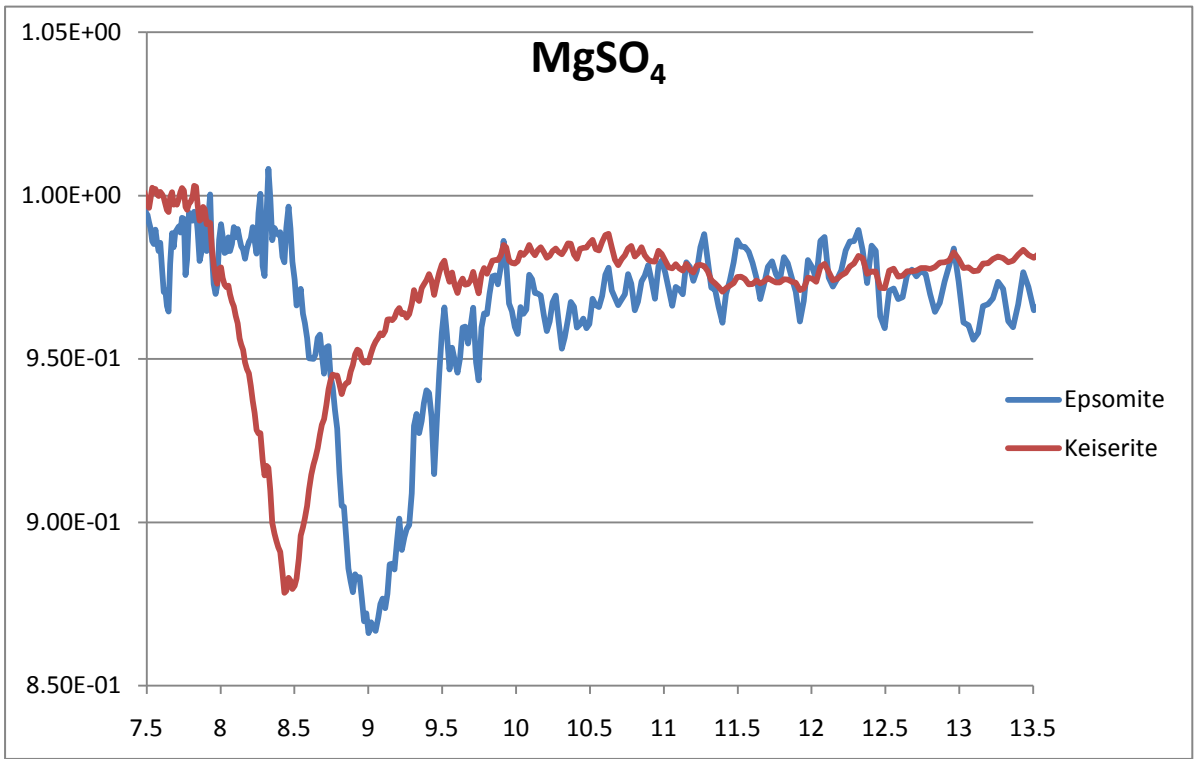

Graph B-1 : This graph depicts the spectra of magnesium sulfate in its hydrous (MgSO4·7H2O-Epsomite) and less hydrated (MgSO4·H2O- Kieserite) forms.

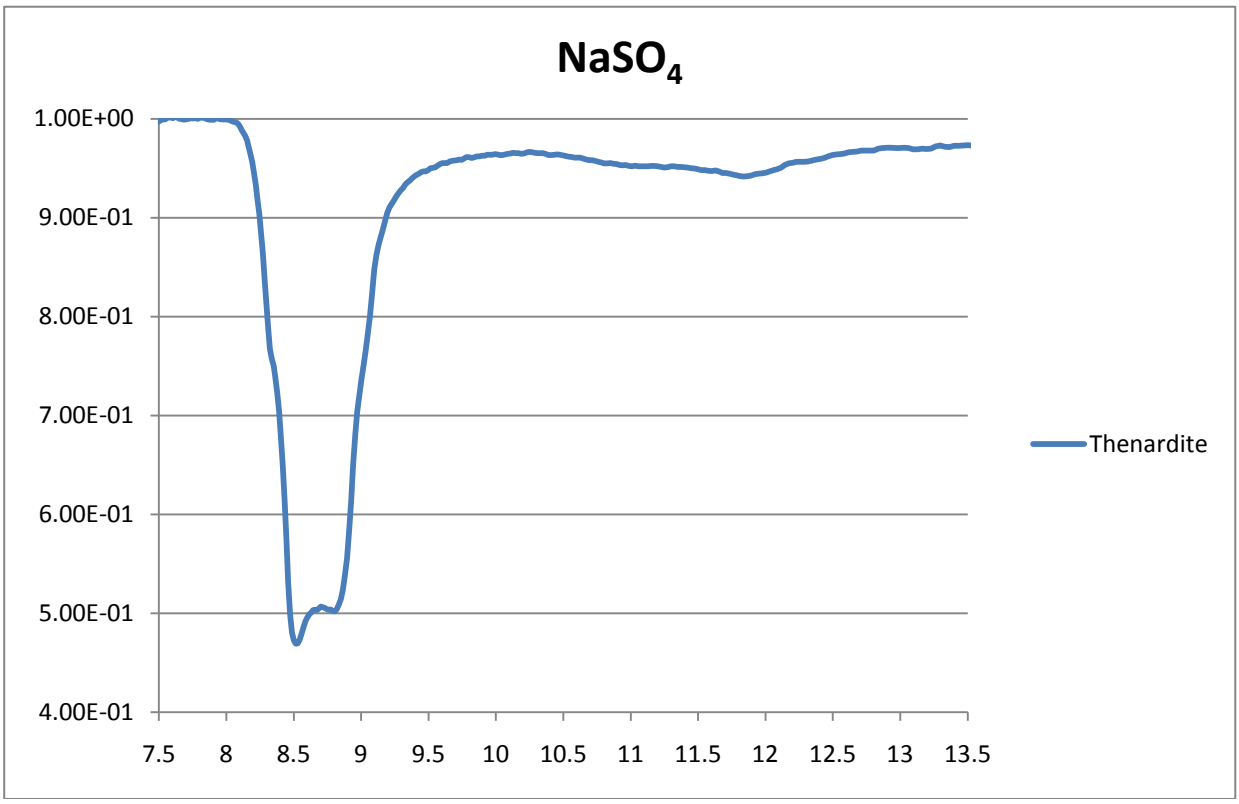

Graph B-2 : Graph of the spectrum of sodium sulfate in its anhydrous form as received from Fisher Scientific.

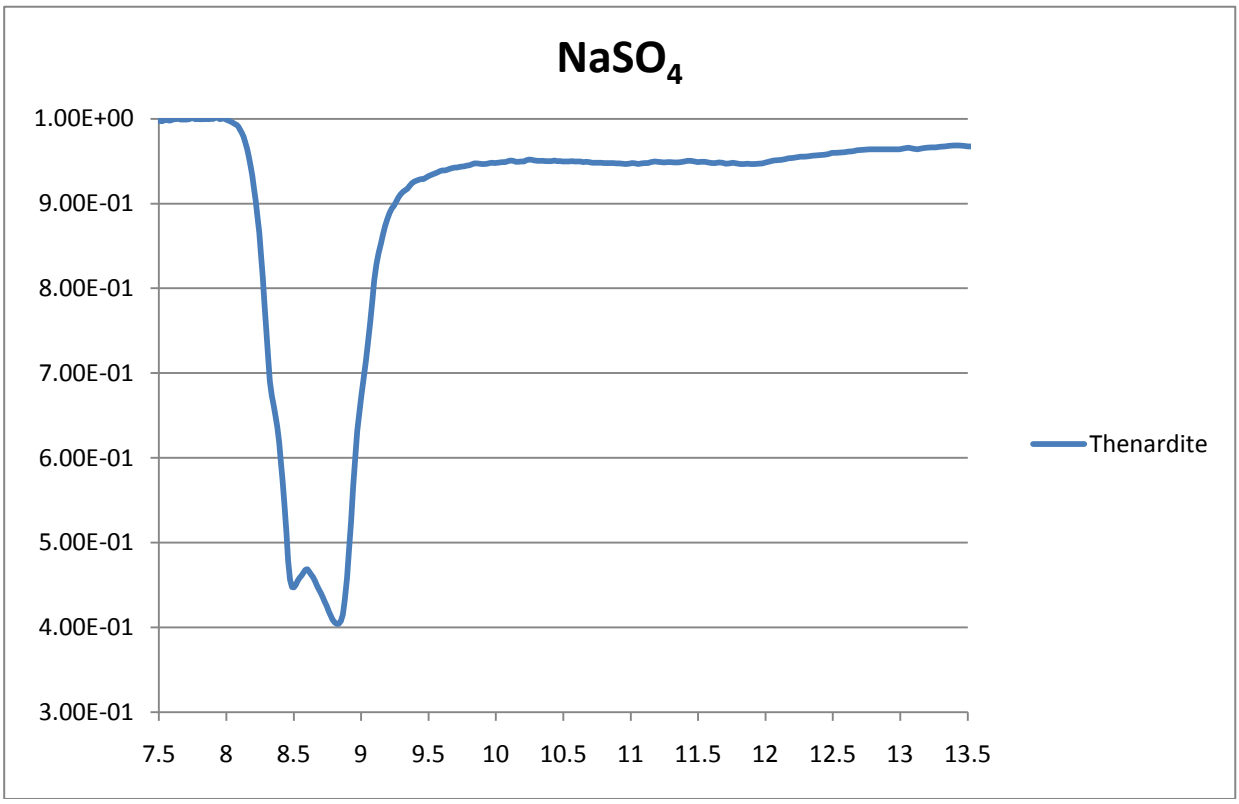

Graph B-3 : This graph depicts the spectrum of sodium sulfate that has been re-hydrated from its original chemical anhydrous form and dehydrated by heat.

BIBLIOGRAPHY

Abrams, M.J., Ashley, L., Rowan, L., Goetz, A., Kahle, A., (1977). Mapping of hydrothermal alteration in the Cuprite Mining District, Nevada, using aircraft scanner images for the spectral region 0.46 to 2.36 Am. Geology 5, 713–718

Adams, J.B., Smith, M.O., Gillespie, A.R., (1989) Simple models for complex natural surfaces: Astradegy for the hyperspectral era of remote sensing, Proc. IGARSS Can. Symp. Remote Sens., 12th, 16-21

Allaby, A., and Allaby, M., (1999) "geothermal field" A Dictionary of Earth Sciences. *Encyclopedia.com.*

Anza group, (2010), Earthquake Swarm near Bombay Beach, Salton Sea, California, Broadchannel Seismic Data Collection Center, eqinfo.ucsd.edu

Blake, W. P.,(1855) Reports of Exploration and Surveys for the Railroad from the Mississippi River to the Pacific Ocean, 1853-1854, Executive Document 78, 33rd Cong. (USA), 2nd Session

Calvin, W.M.; Coolbaugh, M.; Kratt, C.; Vaughan, R.G.; Calvin, W. (2005) Application of Remote Sensing Technology to Geothermal Exploration. In Proceedings of Geological Survey of Nevada Meeting, Reno, NV, USA, May 14–18

Carter, A.J., (2008) Quantitative Thermal Infrared Analysis of Volcanic Processes and Products: Application to Bezymianny Volcano, Russia

Christensen, P. R., J. L. Bandfield, V. E. Hamilton, D. A. Howard, M. D. Lane, J. L. Piatek, S. W. Ruff, and W. L. Stefanov, (2000), A thermal emission spectral library of rock-forming minerals, J. Geophys., 9735 – 9739

Egerton, R. F. (2005) Physical principles of electron microscopy: an introduction to TEM, SEM, and AEM. Springer, 202

Elders, W. A., S. Biehler, R. W. Rex, P. T. Robinson, and T. Meidav, (1972) Crustal spreading in Southern California: The Imperial Valley and the Gulf of California formed by the rifting apart of a continental plate, Science, 178, 15– 24, doi:10.1126/science.178.4056.15.

Elders, W. A., and Sass, J. H., (1988) An Overview of the Salton Sea Drilling Project, JGR November 10

Fujisada, H., Sakuma, F., Ono, A., Kudoh, M., (1998). Design and preflight performance of ASTER instrument protoflight model. IEEE Trans. Geosci. Remote Sens. 36, 1152–1160.

Gillespie A.R., (1992), Enhancement of Multispectral Thermal Infrared Images: Decorrelation Contrast Stretching, Remote Sens Environ. 42: 147-155

Gillespie,A.R.,(1985) "Lithologic mapping of silicate rocks using TIMS," in The TlMSData User's Workshop, June 18-19, 1985, JPL Pub. 86-38, pp. 29-44

Hackwell, J.A., D.W. Warren, R.P. Bongiovi, S.J. Hansel, T.L. Hayhurst, D.J. Mabry, M.G. Sivjee, and J.W. Skinner (1996), "LWIR/MWIR imaging hyperspectral sensor for airborne and ground-based remote sensing," Proceedings of SPIE, 2819, 102-107, doi:10.1117/12.258057.

Hall, J.L., J.A. Hackwell, D.M. Tratt, D.W. Warren, and S.J. Young (2008), "Space-based mineral and gas identification using a high-performance thermal infrared imaging spectrometer," Proceedings of SPIE, 7082, 70820M, doi:10.1117/12.799659.

Helgeson, H.C.,(1968) Geologic and Thermodynamic Characteristics and the Salton Sea Geothermal System, American Journal of Science, Vol. 266, Pg. 129-166, March

Herzig, C.T., Mehegan, J.M., and C.E. Stelting, (1988) Lithostratigraphy of the State 2-14 borehole: Salton Sea Scientific Drilling Project: J. Geophys. Res.

Herzig, C.T., and Elder, W.A., (1988) Probable Occurrence of the Bishop Tuff in the Salton Sea Scientific Drilling Project Bore, Salton Sea Geothermal System, California, Geothermal Resources Council, TRANSACTIONS, Vol. 12, October

Jordan, G. and Astilleros J.M., (2006) In situ HAFM study of the thermal dehydration on gypsum (010) surfaces, American Mineralogist; April; v. 91; no. 4; p. 619-627

Jakubov, A. A., A. A. Ali-Zade, and M. M. Zeinalov (1971), Mud Volcanoes of the Azerbaijan SSR, (in Russian), Azerbaijan Acad. of Sci., Baku, Azerbaijan.

Kääb, A., Wessels, R., Haeberli, W., Huggel, C., Kargel, J.S., Khalsa, S.J.S., (2003). Rapid Aster imaging facilitates timely assessments of glacier hazards and disasters. EOS, Trans. Am. Geophys. Union, 13 (84), 117–121.

King, P. L., Ramsey, M. S., McMillan, P. F., & Swayze, G. (2004). Laboratory fourier transform infrared spectroscopy methods for geologic samples. In P. L. King, M. S. Ramsey, & G. A. Swayze (Eds.), *Infrared Spectroscopy in Geochemistry, Exploration Geochemistry, and Remote Sensing, Vol. 33* (pp. 57-91). London, Ontario: Mineralogical Association of Canada.

Lohman, R. B. & McGuire, J. J., (2007), Earthquake swarms driven by aseismic creep in the Salton Trough, California. J. Geophys. Res. 112, B04405

Li, F and Husar, B. H., (1999), Pre-processing of Sea WiFS Satellite Data for Aerosol Retrieval, Center for Air pollution Impact and trend Analysis Meeting

MacDonald, G. J. F., (1953), Anhydrite-gypsum equilibrium relations: Am. Jour. Sci., v. 251, p. 884-898

McKibben, M.A., Andes, J.P., and Williams, A.E., (1988) Active ore formation at a brine interface in metamorphosed deltaic –lacustrine sediments: The Salton Sea geothermal system, California, Econ. Geol., 83, 511-523

National Weather Service, (2011), Advanced Hydrologic Prediction Service, Precipitation, http://water.weather.gov/precip/

Planke, S., H. Svensen, M. Hovland, D. A. Banks, and B. Jamtveit ,(2003) Mud and fluid migration in active mud volcanoes in Azerbaijan, Geo Mar. Lett., 23, 258– 268, doi:10.1007/s00367-003-0152-z.

Ramsey, M.S., Christensen, P.R., (1998), Mineral abundance determination: Quantitative deconvolution of thermal emission spectra, JGR, vol. 103, no. B1, pg., 577-596, January 10

Realmuto, V.J., (1990) Separating the effects of temperature and emissivity: Emissivity spectrum normalization. In: Proceedings of the 2nd TIMS Workshop, vol. 2, pp. 31–35.

Rook, S.H., and Williams, G. C., (1942) Imperial Carbon Dioxide gas field, Calif. Div. Oil and Gas Bull., v. 28, pg. 12-23,

Ruff, S. W., Christensen, P. R., Barbera, P. W., & Anderson, D. L. (1997). Quantitative thermal emission spectroscopy of minerals: A laboratory technique for measurement and calibration, *Journal of Geophysical Research*, 14,899-14,913.

Sabins, F.F., (1999). Remote sensing for mineral exploration. Ore Geol. Rev. 14, 157– 183.

Sass, John, H., (1988) The Salton Sea Drilling Project, Journal of Geophysical Research, Vol. 93, No. B11, Pg. 12, 953-12, 968, November 10

Saunders, P.H., (1967): The temperature at the ocean-air interface. J.Atmos Sci., 24, 269-273

Spencer, R.J., (2000), Sulfate Minerals in Evaporite Deposits, in Sulfate Minerals: Crystallography, Geochemistry, and Environmental Significance, Rev. Mineral. Geochem., vol. 40

Svensen, H., Ø. Hammer, A. Mazzini, N. Onderdonk, S. Polteau, S. Planke, and Y. Podladchikov,(2009) Dynamics of hydrothermal seeps from the Salton Sea Geothermal System (California, USA) constrained by temperature monitoring and time series analysis, J. Geophys. Res., B09201, doi:10.1029/2008JB00624

Svensen, H., D. A. Karlsen, A. Sturz, K. Backer-Owe, D. A. Banks, and S. Planke, (2007) Processes controlling water and hydrocarbon composition in seeps from the Salton Sea geothermal system, California, USA, Geology, 35, 85– 88, doi:10.1130/G23101A.1.

Thompson, J.M. and Fournier, R.O., (1988) Chemistry and Geothermometry of Brine Produced from the Salton Sea Scientific Drill Hole, Imperial Vally, California, J. Geophys. Res., Vol. 93, Pg. 13,165-13,173, November 10

Van de Kamp, P.C., (1973) Holocene continental sedimentation in the Salton Basin, California: A reconnaissance, Geol. Soc. Am. Bull., 84, 827-848

Vaughan, R.G., Calvin, W.M., and Taranik, J.V., (2003) SEBASS Hyperspectral Thermal Infrared Data: Surface Emissivity Measurement and Mineral Mapping, Remote Sens. Of Envir. 85, pg. 48-63

Vincent, R.K., Pleitner, P.K., Wilson, M.L., (1984). Integration of Airborne Thematic Mapper and Thermal Infrared Multispectral Scanner data for lithologic and hydrothermal alteration mapping. Proceedings of the International Symposium on Remote Sensing of the Environment, Third Thematic Conference. Remote Sensing for Exploration Geology, vol. 1. Erim International, Paris, France, pp. 219– 226.

Yamaguchi, Y., Kahle, A.B., Tsu, H., Kawakami, T., Pniel, M., (1998). Overview of Advanced Spaceborne Thermal Emission and Reflection Radiometer (ASTER). IEEE Trans. Geosci. Remote Sens. 36, 1062–1071.

Younker, L. W., P. W. Kasameyer, and J. D. Tewhey (1982), Geological, geophysical, and thermal characteristics of the Salton Sea Geothermal Field, California, J. Volcanology Geothermal Res., 12(3-4), 221-258, doi:10.1016/0377-0273(82)90028-2.